University of Bergen

Master Thesis in Medical Physics and Technology

Development of a Monte Carlo Based Treatment Planning Verification Tool for Particle Therapy

Lars Fredrik Fjæra

Supervisors:
Ph.D. Kristian Smeland Ytre-Hauge
Professor Dieter Röhrich

Department of Physics and Technology

June 2016

"Cancer is the ultimate nemesis that hangs in the balance for one in three women and one in two men in their lifetime."

— David Agus, M.D.

Abstract

Radiation therapy is an important component of cancer treatment. The favorable characteristics of proton radiation open the possibility of conforming the treatment dose to the target volumes and sparing of the surrounding healthy tissue. Pencil beam scanning is the current state of the art treatment method for delivering proton therapy. Accurate delivery of the prescribed radiation dose in a cancer patient, requires precisely calculated dose distributions. Commercial treatment planning systems (TPS) must compromise in the level of accuracy in order to compute the radiation plans in a reasonable amount of time. This trade-off can be considerable, especially in heterogeneous regions or in the case of metallic implants. Monte Carlo (MC) simulations are currently the gold standard in dose calculation. The FLUKA MC Code is a general purpose MC tool that enables recalculation of dose distributions and verification, in addition to more detailed studies not feasible in a TPS or other more specific MC codes. All treatment plan information is contained in a common format (DICOM), which must be adapted to be readable for most MC tools, including FLUKA.

In this project, a tool that translates treatment plan information into data readable for the FLUKA code was developed. The tool includes several routines based on Python scripts. It enables reading of relevant treatment plan settings required to automatically generate a FLUKA simulation file for dose recalculation. Functions for data analysis and visualization, as well as comparison between the TPS and FLUKA results were also created. In addition, scripts for converting a FLUKA calculated dose distribution into DICOM format were created. The results in this work demonstrate the feasibility of FLUKA MC recalculation of TPS generated dose distributions through the developed software. Treatment plans for both water phantoms and for actual patients were successfully recalculated in FLUKA. The FLUKA doses were also exported to DICOM files and can be imported back into a TPS for dose evaluation. The results further stress the importance of detailed information and calibration to the specific beam line for obtaining clinical precision of the recalculation process.

This developed and tested tool is a contribution to software that enables MC treatment plan verification and can further be implemented in proton and particle therapy TPSs. Furthermore, the tool enable detailed studies of the dose distributions, including linear energy transfer (LET) and secondary particle production. Such tools are essential in radiobiological modeling.

Acknowledgements

I would first like to thank my supervisors Ph.D. Kristian Smeland Ytre-Hauge and Professor Dieter Röhrich.

Thank you, Ph.D. Kristian Smeland Ytre-Hauge, for presenting me with this project and providing me with all necessary tools and inspiration for writing this master thesis. Thanks for all conversations and guidance. And thank you for making a collaboration with the Haukeland University Hospital possible.

Thank you, Professor Dieter Röhrich, for your helpful guidance in this project. And thank you for several enthusiastic lectures about particle therapy a few years back. You are part of the reason I decided to do a master's degree in Medical Physics.

I would also like to thank Camilla Hanquist Stokkevåg for providing me with several treatment plans used in this project. And thank you for helping me with further treatment planning and other clinical challenges beyond my expertise, even though you had a very busy schedule.

I want to thank the Ph.D. students Tordis Dahle and Eivind Rørvik for all provided help and ideas. Thank you, Eivind for brainstorming me out of trouble when the laws of physics did not listen to me, and thank you Tordis for reading my entire thesis and giving me invaluable feedback.

Thanks to Marcin Sikora for giving me access to the RayStation treatment planning system. Thanks to Grete May Engeseth for calculating treatment plans and further help with treatment planning. And thanks to the rest of the people at Haukeland who has in any way contributed to this project.

Thanks to Andrea Mairani for letting us visit at CNAO and for providing helpful knowledge in the science of particle therapy.

Thanks to all my friends at the institute. Thank you Håkon Eidsvåg and Kristian Austreim for giving me answers to all the homework for the first two years (no wonder I am a mathematical genius), and for good friendship these last six years. I am looking forward to the next six(ty). Also thanks to Are Træet, Simen Hellesund and Andreas Heggelund for letting me procrastinate in your office, when I rather should have been working on my thesis.

Thank you, my dear sister Hege Terese Fjæra, for your fantastic friendship. And a huge thanks for being excellent in English. Your proofreading has been a great help.

And lastly, a special thanks to my wonderful parents Lill Turid and Terje Georg Fjæra. You have no idea how much your support means to me. I am forever grateful.

Bergen, June 2016
Lars Fredrik Fjæra

Contents

List of Figures

List of Tables

List of Abbreviations

ART	**A**daptive **R**adiation **T**herapy
CSDA	**C**ontinuous **S**lowing **D**own **A**pproximation
CSI	**C**ranio **S**pinal-**I**rradiation
CTV	**C**linical **T**arget **V**olume
CT	**C**omputed **T**omography
DSB	**D**ouble-**S**trand **B**reak
DVH	**D**ose **V**olume **H**istogram
GTV	**G**ross **T**umor **V**olume
HFP	**H**ead **F**irst - **P**rone
HFS	**H**ead **F**irst - **S**upine
HU	**H**ounsfield **U**nit
ICRP	**I**nternational **C**ommission on **R**adiological **P**rotection
ICRU	**I**nternational **C**ommission on **R**adiation **U**nits & Measurements
IMPT	**I**ntensity-**M**odulated **P**article **T**herapy
IMRT	**I**ntensity-**M**odulated **R**adiation **T**herapy
LET	**L**inear **E**nergy **T**ransfer
MC	**M**onte **C**arlo
MLC	**M**ulti**L**eaf **C**ollimator
NIST	**N**ational **I**nstitute of **S**tandards and **T**echnology
NTCP	**N**ormal **T**issue **C**omplication **P**robability
OAR	**O**rgan **A**t **R**isk
PB	**P**encil **B**eam
PRV	**P**lanning Organ at **R**isk **V**olume
PTV	**P**lanning **T**arget **V**olume

RBE	**R**elative **B**iological **E**ffectiveness
ROI	**R**egion **O**f **I**nterest
SOBP	**S**pread-**O**ut **B**ragg **P**eak
SSB	**S**ingle-**S**trand **B**reak
TCP	**T**umor **C**ontrol **P**robability
TPS	**T**reatment **P**lanning **S**ystem
VMAT	**V**olumetric **M**odulated **A**rc **T**herapy

Chapter 1

Introduction

On a clinical level, cancer is not *one* disease, but rather a term referring to a large number of diseases. However, in the end, cancer's overall result is an imbalance of cell replication and cell death. If these cells has the ability to invade locally, spread to regional lymph nodes and to metastasize to distant sites in the body, the cancer is characterized as malignant and may further be lethal. Cancer can result in an expansion of cancerous tissue, known as a tumor [1].

Cells in the human body replicate and die every second. Cell replication is what makes children grow, wounds heal and people age. When a cell replicates, it transfers the genetic code of its DNA to the new cell. Normal healthy cells become cancerous as a result of mutations caused by changes in the DNA. While this occurs quite often, DNA enzymes repair most of these mutations. However, the enzymes are not 100 % effective, and thus, cancer in the form of, for example, a tumor can occur in all parts of the body. If the tumor is malignant it can be highly dangerous, deadly, and difficult to remove [2].

According to the World Health Organization, cancer is the worldwide leading cause of death for people under the age of 85 [3]. In 2013, a total of 29,793 Norwegians were diagnosed with cancer, whereas the same year, 10,699 people died of the disease [4]. The number of cancer incidences will continue to rise further, mainly due to the increase in population and life expectancy, as cancer is strongly related to age [1]. This demands for more and better treatment methods.

In 2011, more than 11,000 patients were treated using radiation therapy with photons in Norway [5]. Over half of all patients diagnosed with cancer will receive radiation therapy, either as a standalone treatment, or in conjunction with other treatment methods such as surgery and chemotherapy [6].

Radiation therapy using protons or heavy ions, also known as particle therapy, is still limited compared to photon therapy. The use of particle therapy is however expected to greatly increase in the years to come [7]. Since the first person was treated in 1954 [8] at the Lawrence Berkeley Laboratory in California, by the year 2014, more than 137,000 patients has been treated by particle therapy worldwide, where 86 % of the treatments were conducted with protons. By the end of 2014, 48 particle therapy facilities were in clinical operation, and in 2015, more than 30 particle therapy centers were under construction worldwide [9]. Norway received its consent for the startup of particle therapy facility planning by the Minister of Health and Care Services in 2013 [10]. The potential treatment centers are currently still in the review process.

1.1 A Short Radiotherapeutic History

On November 30th, 1895, Wilhelm Röntgen announced his discovery of X-rays. At the end of January 1896, approximately 60 days after Röntgen's announcement, Emil Grubbe, a second-year medical student treated the first two patients with X-rays. The first was breast cancer and the other, skin lesions due to Tuberculosis. This gave birth to radiation therapy [11].

Radiation therapy has been constantly developing for the last 120 years. However, the aim has always been the same, to deliver as close as possible to 100 % of the prescribed dose to the target volume, while at the same time spare as much of the healthy tissue as physically possible. The advancements since 1895 have been tremendous.

In the beginning, treatments were available for only superficial tumors and melanomas, due to the relatively low photon energies that were achievable. But as the years went by, both supervoltage X-ray tubes and linear accelerators were developed, which allowed for treatment of more deep-seated tumors. As early as in 1906, different patterns of radiosensitivity were demonstrated, and in 1934 radiation dose deliverance using fractionation, as opposed to deliver all the dose at the same time, was proposed. These developments, amongst others, led to better cure rates for cancer and less damage to healthy tissue [3].

In 1953, the first linear accelerator for photon therapy was installed in London. This was only a few years after Robert Wilson's emphasis on the therapeutic advantage of using protons in radiation therapy in his article *Radiological Use of Fast Protons* [12] published in 1946. He also proposed the use of heavier ions. As mentioned, the first patient was treated with protons as early as in 1954, while treatments using helium- and neon ions were first conducted in 1957 and 1975, respectively [8]. In the years following the 1960s, the definitions of target volumes and organs at risk were identified by the International Commission on Radiation Units and Measurements (ICRU). The first treatment planning systems also arrived, allowing more accurate treatment planning [3].

Thanks to Godfrey Hounsfield's development of the CT scanner in 1971, radiation planning started to shift from two- to three dimensions. In consequent years, CT-based simulations and dose planning were introduced, and computer driven multileaf collimators (MLC) conforming the radiation field, were developed in the 1990s. With this, radiation therapy treatment could be done by sculpting the dose in three dimensions onto target volumes and easier avoidance of organs at risk could be accomplished.

Going into the early 2000s, intensity-modulated radiation therapy (IMRT)[1], followed by volumetric modulated arc therapy (VMAT)[2] and adaptive radiation

[1]Intensity-modulated radiation therapy: Treatment using computer based algorithms to modulate the photon beam intensity by changing the MLC positions. Dose calculations performed via inverse planning.

[2]Volumetric modulated arc therapy: Similar to IMRT, only that the gantry is continuously moving during beam radiation. Effective for decreasing the treatment duration.

therapy (ART)[3] had a significant effect on the successfulness of radiation therapy. The many delivery techniques and methods developed in the last century have made it possible to personalize the radiation therapy techniques based on different types of patients, tumor extents and locations. However, the spatial dose distribution from photons must unfortunately follow the laws of physics, meaning that there is an upper limit to the achievable dose conformity. Which brings us to the usage of particles in radiation therapy [3, 13].

1.2 The Rationale and Motive for Particle Therapy

One of the biggest advantages of conducting radiation therapy using protons or heavy charged particles, like carbon- or helium ions, is the mechanics of their dose deposition compared to photons [14, 15]. Photons have a short build-up region, followed by an exponential decrease in the dose deposition with increasing depth. This means that a considerable amount of healthy tissue will receive dose for photon treatment of deep-seated tumors. And due to the penetrating ability of photons, tissue beyond the target of interest will also be irradiated [16]. In 1946, Robert Wilson based his statements, about the advantage of using protons in radiation therapy, on their well-known physics; they slow down during material penetration. As the velocity of a proton decreases, the energy loss per unit length increases, causing a maximum dose deposition at a certain depth. This region of dose deposition is known as the Bragg peak, located near the end of the protons' range. It is followed by a rapid decrease in dose deposition, and the protons will not penetrate any further. The proton penetration depth is highly energy dependent, and thus by adjusting the beam energy, the Bragg peak can be spread out over e.g. a tumor, creating a so-called spread-out Bragg peak (SOBP) [7]. The same applies to, for example, carbon ions. The main difference is the considerably sharper carbon Bragg peak, in addition to the extended fragmentation tail located after the peak [8].

The depth dose curves for photons, protons and carbon ions are shown in Figure 1.1. The figure depicts the dose from a single field for all three particles. For protons and carbon ions, there are some treatment cases where only one field is used. On the other hand, there are also many cases where two or more beams are applied to achieve an even higher dose conformity [18]. For photons, a single beam is rarely used [19]. Following the development of IMRT and VMAT, a higher dose conformity for photon therapy was achieved [3], meaning that it was possible to distribute the dose over more tissue, reducing the amount of healthy tissue receiving high doses compared to what Figure 1.1 shows. However, the external modulations and conformations applied in photon therapy can also be used in particle therapy, and due to heavy charged particles' much more advantageous physics, a lower integral dose, perhaps as high as a factor of 2-3 [20], may be

[3]Adaptive radiation therapy: Changing the radiation plan during the course of treatment to account for anatomical changes such as tumor shrinkage, weight loss etc.

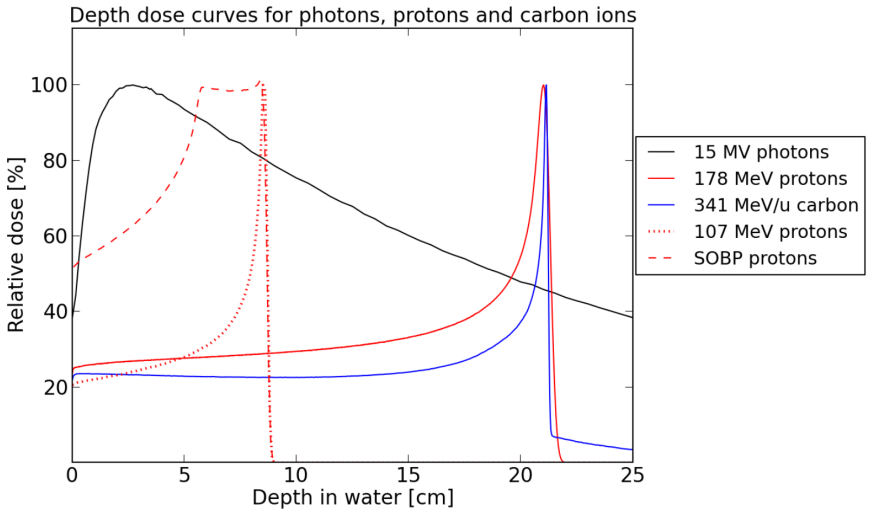

Figure 1.1: The depth dose curves for photons, protons and carbon ions. The protons and carbons deposit a large fraction of the dose deep into the medium, while the photons have a maximum dose deposition a few centimeters into the medium. The dashed red line shows a proton SOBP. Also notice the sharper carbon Bragg peak, in addition to the fragmentation tail [17].

achieved [21]. Two-dimensional dose distributions from radiation plans for photon- and proton treatment are seen in Figure 1.2.

There are indications that patients undergoing radiation therapy may have an increased risk of secondary malignancies as a result of out of out-of-field doses to healthy tissues [23, 24]. There has in addition been shown a significantly higher risk of developing radiation-induced cancer for pediatric patients treated with photon treatment techniques as compared to proton therapy [25]. Considering that the risk of developing radiation-induced cancer increases throughout a patient's lifetime [26], reducing the total dose can potentially increase the overall quality of the life for pediatric patients. There are however discussions as to whether the advantages of particle therapy are clinically significant for all treatment sites [7].

There are also concerns about the cost of proton therapy. An article [27], published in 2010, estimated a cost ratio between particle therapy and photon therapy to 4.8 for combined proton and carbon ion facilities, and 3.2 for proton-only facilities. The cost of particle therapy is however expected to decrease, and if it is possible to reduce the risk of secondary malignancy by using particles in cancer treatment, in addition to lower the number of treatment fractions, fewer people will need treatment for side effects, and patients will spend less time in the hospital. Therefore, particle therapy may be ultimately economically advantageous compared to photon therapy.

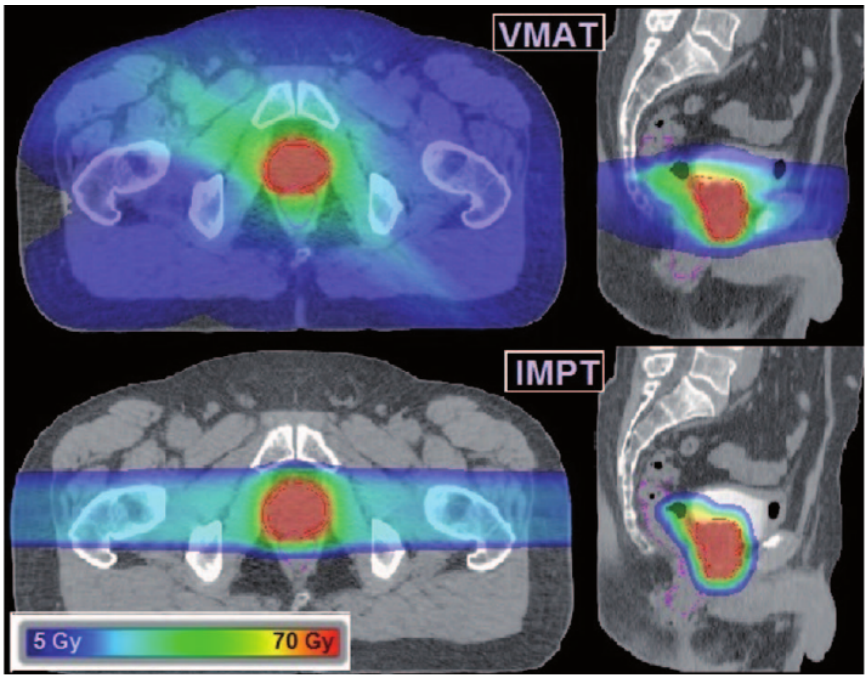

Figure 1.2: Dose distributions for a prostate cancer patient using VMAT and intensity-modulated proton therapy (IMPT). Notice the increased out-of-field doses to healthy tissues by VMAT [22].

1.3 Monte Carlo Simulations in Particle Therapy

Due to the finite range of protons and ions and the steep distal dose fall-off, particle therapy is a treatment modality capable of delivering high-precision and conformal treatments. However, a safe and optimal treatment relies on a good correspondence between the planned and delivered dose to the patient [28]. Heterogeneities in tissues are of a much higher importance in proton therapy compared to conventional photon therapy. The range of protons is strongly dependent on the density of the tissues they traverse, and as a result, the distal part of the dose distribution can be substantially affected by heterogeneities [29, 30].

There are three main models for dose calculation in proton therapy; uniform intensity beam algorithms, pencil beam (PB) algorithms and Monte Carlo calculations [31]. A necessity for all three is that they require an accurate three-dimensional description of the patient anatomy in the form of computed tomography images. The uniform intensity beam algorithms are the least accurate and will not be discussed further.

Commercial treatment planning systems (TPS) are today used by clinics in order to calculate radiation plans for patients. TPSs usually rely on PB algorithms to calculate the dose, which are considered to offer a reasonable compromise between accuracy and computation time. This method models the incident beam using closely spaced finite PBs, each assigned its own weight directly proportional to the particle fluence for the respective beam. Measured or calculated data is used for modeling the spread of the PB due to multiple Coulomb scattering, in

addition to the depth dose distribution. The total dose in any point can then be computed by summarizing the contributions from each PB [31]. Although PB algorithms are highly accurate, they can still encounter problems for dose calculations in low-dose regions, in very heterogeneous tissues or if metallic implants are present. This is where Monte Carlo calculations are most desirable due to their superior accuracy [15, 32–37].

Monte Carlo simulations are considered the gold standard for dose calculations in particle therapy [38, 39]. The reason for the high accuracy is that the physics of interactions for each and every particle is taken into account using theoretical models or experimental data for electromagnetic and nuclear interactions. They further consider material specific properties, as for example elemental composition, electron density, ionization potential, and so forth [35]. In addition, secondary particles can be tracked, which allow for nuclear fragments to be studied. However, the accuracy of the dose calculations performed depends on the calculation duration. As a result, in order to obtain sufficient statistical accuracy, a substantial amount of particles must be tracked. These calculations can require a lot of time, making them potentially unsuitable for clinical applications on a routine basis. But Monte Carlo simulations are regularly used for TPS benchmarking, in addition to being the preferred choice for special geometries, e.g. metallic implant cases. Monte Carlo simulations are, in addition, often used for recalculation or validation of analytically calculated dose distributions, and for to treatment plan optimization. And as time moves forward and the computational efficiency increases, the Monte Carlo code will hopefully become optimized for routine clinical use and may replace the pencil beam algorithms as the standard method for patient dose calculation [16, 31].

1.4 Project Objectives

The main objectives of this project has been to:

- Develop and test a procedure to extract CT-scans along with proton therapy treatment plans from commercial dose planning systems, and further translate and import this information into the FLUKA [40, 41] Monte Carlo tool to enable dose recalculation and validation of treatment plans.

- Develop tools for versatile comparisons of the initial- and recalculated dose distributions, in addition to making studies of biologically relevant parameters such as linear energy transfer distributions feasible.

Chapter 2 provides the basic physics relevant for particle therapy. This includes the main interactions of heavy charged particles, alongside a short summary of basic dosimetry and radiobiology focusing on linear energy transfer and relative biological effectiveness.

Chapter 3 emphasizes the main aspects of the particle therapy processes. Treatment planning, followed by plan assessment, treatment delivery and uncertainties in particle therapy are successively discussed. A short introduction to the

DICOM file standard and the coordinate systems involved in the project is also found in this chapter.

Chapter 4 contains the method of developing and applying the scripts in this project. The most important aspects to consider when developing this tool are outlined.

Chapter 5 presents the results obtained when testing the developed tool. Two-dimensional dose distributions from commercial treatment planning systems alongside FLUKA recalculations, in addition to one-dimensional dose curves and dose volume histograms are shown.

Chapter 6 contains the discussion, outlined shortcomings, potential for the tool and suggestions for further work.

Chapter 7 forms the final conclusion.

All FLUKA Monte Carlo simulations in this thesis are produced by the author, unless specified otherwise.

Chapter 2

Physics of Particle Therapy

2.1 Charged Particle Interactions in Matter

2.1.1 Energy loss by ionization and excitation

Heavy charged particles, i.e. particles with mass greater than the electron rest mass, lose energy while traversing through matter mainly by collisions with bound electrons. In these collisions an electron can either be raised to a higher shell in the absorbing atom (excitation) or it can be ejected from the atom (ionization). If the ejected electron receives enough kinetic energy, it can cause further ionizations. These electrons are referred to as δ-electrons [42]. The energy loss per collision is typically very small. However, because of the high number of collisions per unit path length, a substantial fraction of the interacting particle's kinetic energy can be transferred to a relatively thin layer of matter [43]. The mean energy loss per unit length for a charged particle traversing through matter is described by the Bethe-Bloch equation [44]:

$$-\left\langle \frac{dE}{dx} \right\rangle = Kz^2\rho\frac{Z}{A}\frac{1}{\beta^2}\left[\frac{1}{2}\ln\frac{2m_ec^2\beta^2\gamma^2W_{\max}}{I^2} - \beta^2 - \frac{\delta(\beta\gamma)}{2} - \frac{C}{Z}\right], \tag{2.1}$$

where

$$K = 4\pi N_A r_e^2 m_e c^2 \approx 0.307\,\mathrm{MeVcm^2g^{-1}}\ ,$$

and W_{max} is the maximum energy that can be transferred to a free electron in a single collision given by

$$W_{\max} = \frac{2m_ec^2\beta^2\gamma^2}{1 + 2\frac{m_e}{m}\sqrt{1+\beta^2\gamma^2} + \frac{m_e^2}{m^2}}\ . \tag{2.2}$$

Table 2.1 provides the variables used in the Bethe-Bloch equation. The mean excitation potential, I, is in essence Planck's constant, h, times the electrons average orbital frequency, $\bar{\nu}$ [43]. Using a correctly determined excitation potential is of high importance in particle therapy as the uncertainty of the excitation potential for tissues can be as high as between $5-15\,\%$ [30] and can alter the calculated energy loss, and thereby the beam range by as much as $1.5\,\%$ [21].

The shell correction, C, is important at low energies, i.e. when the velocity of the incoming particle approaches and becomes smaller than the orbital velocity of the electrons in the absorbing material. The correction is applied in the energy

Table 2.1: Relevant parameters used in the Bethe-Bloch equation.

Symbol	Definition	Value and/or unit
ρ	Density of material	$\mathrm{g\,cm^{-3}}$
Z	Atomic number of material	
A	Atomic mass of material	$\mathrm{g\,mol^{-1}}$
z	Charge number of incident particle	
β	v/c of incident particle	
m_e	Electron mass	$\mathrm{MeV\,c^{-1}}$
m	Mass of incident particle	$\mathrm{MeV\,c^{-1}}$
c	Speed of light in vacuum	$2.998 \times 10^8\,\mathrm{m\,s^{-1}}$
γ	Lorentz factor $1/\sqrt{1-\beta^2}$	
I	Mean excitation potential	eV
$\delta(\beta\gamma)$	Density effect correction	
C	Shell correction	
N_A	Avogadro's number	$6.022 \times 10^{23}\,\mathrm{mol^{-1}}$
r_e	Classical electron radius	2.818 fm
v	Speed of incident particle	$\mathrm{m\,s^{-1}}$
$W_{\max}$	Maximum energy transfer in a single collision	

range of $1-100\,\mathrm{MeV}$, and the maximum correction is about 6 % [45]. The δ-term, i.e. the density correction, is only relevant for proton energies higher than for therapeutic purposes [45, 46].

The energy loss for a heavy charged particle is highly energy dependent and is therefore mostly determined by the particle's velocity. For non-relativistic particle energies, the first term in equation (2.1) is predominant, and thus the energy loss has a $1/\beta^2$ dependence. For even lower energies, about 10 MeV or less [42], the Bethe-Bloch equation is no longer valid, and phenomenological fitting formulas and other theories are used to describe the energy loss [44]. The stopping power for protons with energies of $\sim 0 - 200\,\mathrm{MeV}$ traversing through water is shown in Figure 2.1.

2.1.2 Multiple Coulomb scattering

A charged particle traversing through an absorber will not follow a straight path. The particle will be elastically scattered in many small angles [44]. This scattering is mainly due to the incident particle's electric charge interacting via the Coulomb force, i.e. deflection in electric potential of nuclei. This will lead to broadening of particle beams used in radiation therapy [42]. The lateral deflection is smaller for particles heavier than protons and is proportional to the charge of the incoming particle and inversely proportional to the projectile's velocity and the atomic weight [17]. Consideration of the lateral spreading is highly important in particle therapy as the amount of spread is also dependent on the beam line, the distance between the treatment nozzle and the patient, and other treatment room specifics [42]. The lateral spread of protons and carbon ions is illustrated in Figure 2.2.

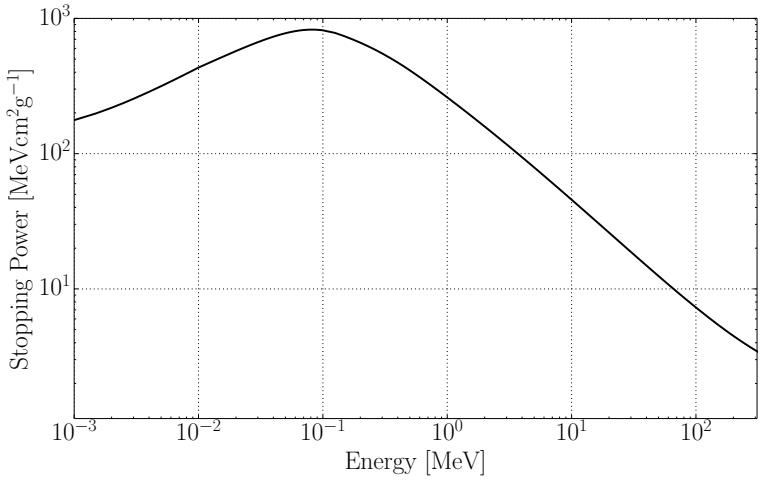

Figure 2.1: Stopping power for protons ($\sim 0-200\,\mathrm{MeV}$) in water. The data is provided by the National Institute of Standards and Technology (NIST) [47].

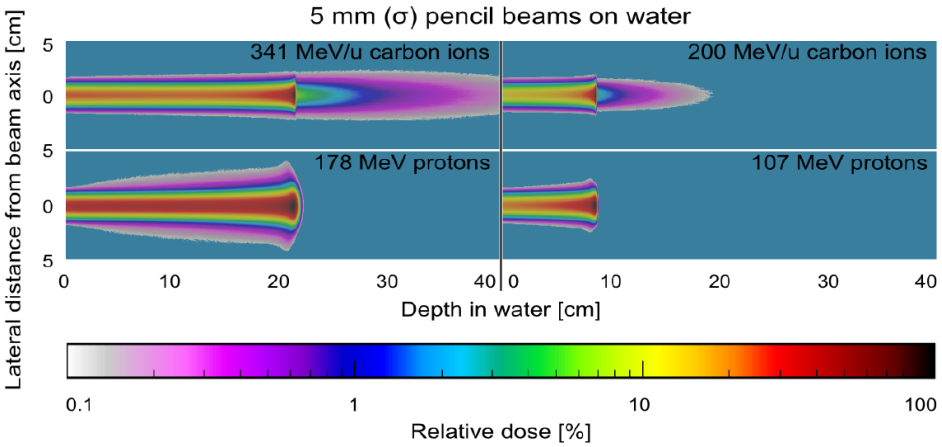

Figure 2.2: Lateral spread for proton- and carbon beams as a function of depth in water. The protons have a three times larger broadening than the carbon ions for the lowest energies depicted on the left. The dose tail, as a result of fragmentation of the carbon ions, can also be seen [17].

2.1.3 Nuclear interaction and fragmentation

Nuclear interactions are, in addition to excitation and ionization, the primary interactions of charged particles in the energy range used in particle therapy [42]. The incoming particles can interact with the nucleus by knocking out secondary particles like protons, neutrons, and light ion clusters. These knocked out particles have, in most cases, a considerably lower energy than the initial particle [7]. However, in all radiation therapy, secondary particles contribute to the total absorbed dose and if a secondary particle is neutral, it is not affected by the Coulomb force and may travel longer, leading to dose deposition outside the target volume [48]. As a result of the beam fragments' forward momentum due to the high velocity of the primary beam particles, an additional dose will be deposited beyond the

maximum range of the primary particles [17]. This effect, see Figure 2.2, is more prominent for carbon ions than protons, considering that the former are composite particles.

2.1.4 Energy-range relation for charged particles

Obtaining the range of a charged particle in matter can be a complicated task as fluctuations in the energy loss, multiple Coulomb scattering and collisions with high energy transfers can lead to considerable energy straggling. From a theoretical point of view, the mean range of a given particle can be calculated by the Continuous Slowing Down Approximation (CSDA), where the stopping power, equation (2.1), is integrated from the maximum energy, E, to 0 [49]:

$$R = \int_E^0 \left(\frac{dE}{dx}\right)^{-1} dE \ . \tag{2.3}$$

The range for protons of energy $0 - 200\,\mathrm{MeV}$ is shown in Figure 2.3.

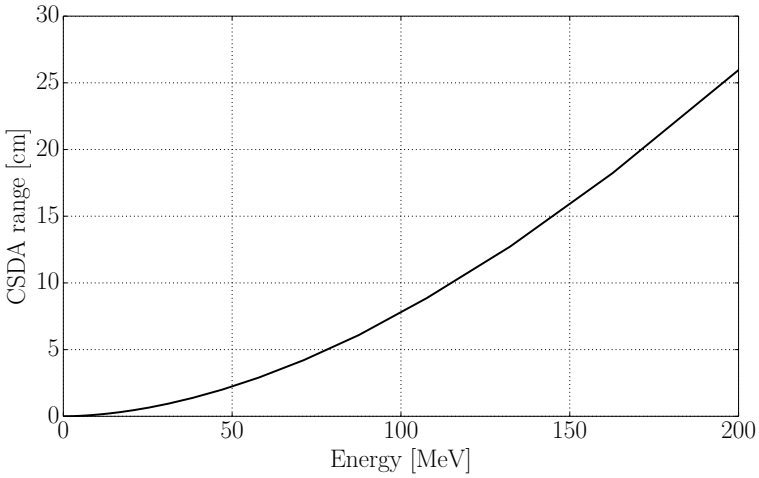

Figure 2.3: The CSDA range vs. energy for protons ($0 - 200\,\mathrm{MeV}$) in water. The data is acquired from Libamtrack [50].

2.1.5 The Bragg peak

A charged particle continuously loses small fractions of energy when traversing matter. This energy loss causes the particle to slow down and the rate of interactions per unit length increases, leading to a maximum energy loss at the end of the particle's range. This region of maximum energy loss is called the Bragg peak. Ideally the energy loss just after the Bragg peak should drop rapidly to zero. As this is the case for a single particle, due to statistical fluctuations in the energy loss, a monoenergetic beam will show the effect of range straggling. This can be seen as a small tail at the end of the particles' range [7]. The Bragg curve for 200 MeV protons in water is shown in Figure 2.4.

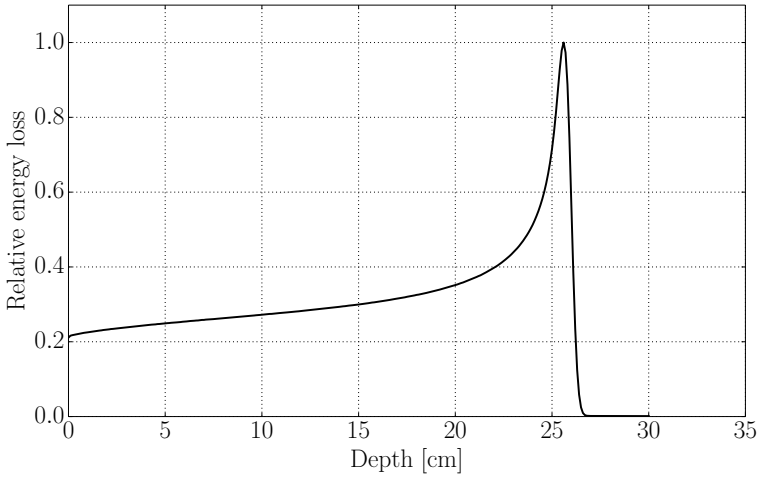

Figure 2.4: FLUKA [40, 41] Monte Carlo simulation of the Bragg curve for 200 MeV protons in water. Notice the Bragg peak at the end of the trajectory.

2.2 Dosimetry

The amount of damage in tissue due to ionizing radiation must be measured with a unit suitable for both radiation protection and radiation therapy [51]. The accuracy of the determination of absorbed dose is highly important, as a small offset of the tumor dose may be the difference between underdosage, thereby failing to control the tumor, and overdosage, potentially resulting in noticeable damage to healthy tissue [7].

2.2.1 Absorbed dose

Radiation damage depends on the amount of energy departed by radiation. It is proportional to the mean concentration of absorbed energy in the irradiated tissue. ICRU defines absorbed dose as the mean energy imparted by ionizing radiation, ΔE, to a certain mass, Δm [52]:

$$D = \frac{\Delta E}{\Delta m} \ . \tag{2.4}$$

The unit for absorbed dose is called Gray (Gy) in the SI system, where $1\,\mathrm{Gy} = 1\,\frac{\mathrm{J}}{\mathrm{kg}}$. An important thing to remember is that the energy lost by e.g. a proton beam is larger than the absorbed dose. This is because a part of the beam's energy will be transformed into neutral secondary particles, e.g. photons and neutrons, which may deposit their energy outside the volume in question [7].

2.2.2 Equivalent dose

Different kinds of radiation have a different biological effect on tissues. In terms of dose, this difference was introduced in 1977 as the equivalent dose [53]. A weighting factor, w_R, was suggested to differentiate between different particles

and energies. The equivalent dose is defined as:

$$H_T = \sum_R w_R D_{T,R} \ , \tag{2.5}$$

where w_R is the weighting factor for distinct radiations, tabulated in Table 2.2, and $D_{T,R}$ is the absorbed dose averaged over the irradiated tissue(s). The unit for equivalent dose is Sievert (Sv) defined as $1\,\mathrm{Sv} = 1\,\frac{\mathrm{J}}{\mathrm{kg}}$ [54].

Table 2.2: Radiation weighting factors as defined by the International Commission on Radiological Protection (ICRP) in ICRP Publication 103 [55].

Radiation type	**Weighting factor, w_R**
Photons	1
Electrons and muons	1
Protons and charged pions	2
Alpha particles, fission fragments and heavy ions	20
Neutrons:	
$E_n < 1\,\mathrm{MeV}$	$2.5 + 18.2e^{-[ln(E_n)]^2/6}$
$1\,\mathrm{MeV} \leq E_n \leq 50\,\mathrm{MeV}$	$5.0 + 17.0e^{-[ln(2E_n)]^2/6}$
$E_n > 50\,\mathrm{MeV}$	$2.5 + 3.25e^{-[ln(0.04E_n)]^2/6}$

2.2.3 Effective dose

The equivalent dose is not concerned as to which tissues are being irradiated. Therefore, ICRP has introduced the effective dose where tissue dependent weighting factors have been added. The effective dose is defined as:

$$E = \sum_T w_T H_T = \sum_{R,T} w_R w_T D_{T,R} \ , \tag{2.6}$$

where w_T is the tissue weighting factor, tabulated in Table 2.3. The unit for effective dose is also Sv [55].

Table 2.3: Tissue weighting factors as defined in ICRP Publication 103 [55].

Organ/tissue	**Weighting factor, w_T**
Breast, bone marrow, colon, lung, stomach, remaining tissues*	0.12
Gonads	0.08
Bladder, liver, esophagus, thyroid	0.04
Bone surface, brain, salivary glands, skin	0.01

*Adrenals, extrathoracic region, gall bladder, heart, kidneys, lymphatic nodes, muscle, oral mucosa, pancreas, prostate, small intestine, spleen, thymus, uterus/cervix.

2.3 Radiobiology

Radiobiology, the branch of science that deals with the effects of ionizing radiation on living systems, is a combination of the basic principles of physics and biology. In radiation therapy, the main goal is to kill the cancer cells. Death for proliferating cells is defined as the loss of reproductive integrity, also called reproductive death [56]. The most radiosensitive part of a cell is the DNA molecule [57]. If the DNA is destroyed, it can lead to cell death [58].

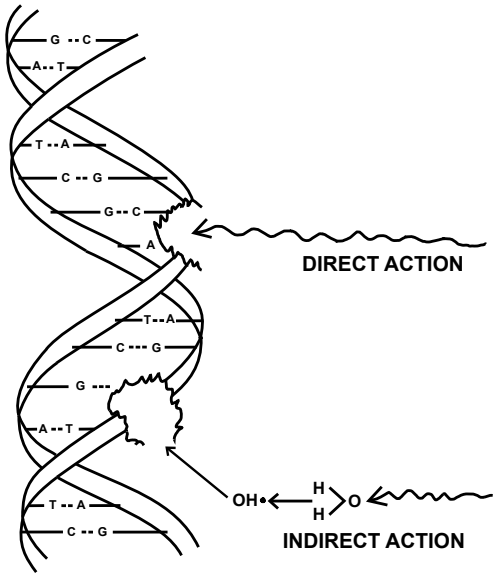

Figure 2.5: Illustration of direct- and indirect single-strand break DNA damage caused by ionizing radiation. Modified from [57].

Different kinds of radiation interact with the DNA molecules in different ways. When a photon is absorbed in the cell, free electrons (δ-electrons) are produced. For radiotherapeutic energies, this happens mainly through the Compton process [56]. These δ-electrons may further ionize atoms in the medium and are able to split one or two of the DNA strands if they are close enough. This type of interaction is called direct action and will in most cases lead to double-strand break (DSB). However, in photon therapy, the majority of strand breaks, i.e. about 70 %, are caused by the so-called indirect action [59]. In indirect action, the produced δ-electrons do not hit the DNA itself, but rather interact with water in the cells. These interactions produce a free radical, OH, which further has the ability to damage the DNA (see Figure 2.5). The disadvantage of indirect action is that more often than not, the damage to the DNA occurs by single-strand breaks (SSB), which is easier to repair than DSBs [57].

2.3.1 Linear energy transfer

Protons and heavier ions have a higher ionization density compared to photons, at least for low energies [56]. As a result, more δ-electrons are produced resulting in

an increased probability to perform DSBs, and thus, more efficient cell inactivation can be achieved with therapy using protons or heavier ions.

Linear energy transfer (LET) is used in radiobiology as a measure of the quality of the ionizing radiation. The International Commission on Radiation Units & Measurements (ICRU) defines the LET as follows [52]:

> *The linear energy transfer or restricted linear electronic stopping power, LET_Δ, of a material, for charged particles of a given type and energy, is the quotient of dE_Δ by dl, where dE_Δ is the mean energy lost by the charged particles due to electronic interactions in traversing a distance dl, minus the mean sum of the kinetic energies in excess of Δ of all the electrons released by the charged particles, thus*
>
> $$LET_\Delta = \frac{dE_\Delta}{dl} \ .$$

The unit used for LET is typically $\mathrm{keV\,\mu m^{-1}}$, and the LET therefore represents the local ionization density in a cellular state. Higher LET means more effective cell killing per unit dose and vice versa for low LET. The demarcation between low- and high LET is about $10\,\mathrm{keV\,\mu m^{-1}}$, and typical values are $2\,\mathrm{keV\,\mu m^{-1}}$ for 250 kVp photons. For heavy charged particles, the LET increases drastically for lower energies (see Figure 2.6) which means that the charged particles are most lethal at the distal end of the Bragg curve. Typical LET values for heavy charged particles are about $100-200\,\mathrm{keV\,\mu m^{-1}}$ in the Bragg peak [19].

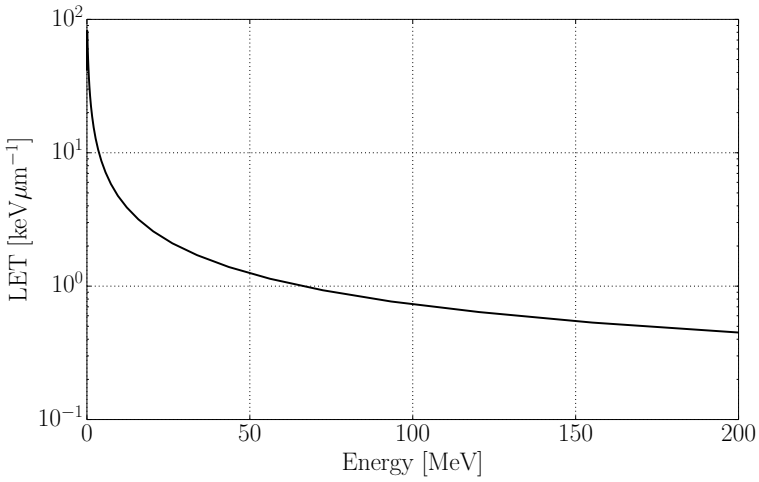

Figure 2.6: Linear energy transfer for $0-200\,\mathrm{MeV}$ protons in water. The LET data is acquired from Libamtrack [50].

2.3.2 Relative biological effectiveness

The relative biological effectiveness (RBE) is a measure of the biological effect of a certain kind of radiation. It is defined as the ratio between the dose of a reference radiation and the dose of the given radiation to achieve the same biological effect.

Historically, the reference radiation has been regarded as 250 kV X-rays. This was done for clinical consistency and to benefit from a large amount of clinical results [60]. The formula for RBE is given below:

$$\mathrm{RBE} = \frac{D_{\mathrm{reference}}}{D_{\mathrm{ions}}} \ . \tag{2.7}$$

Typically, all treatments in proton therapy assume an RBE of 1.1, a value which is primarily based on animal experiments conducted in the 1970s [61]. However, the RBE varies depending on a particle's energy, depth of penetration, dose per fraction and other parameters [7]. The single value of 1.1 is therefore only a generic value. It has been shown in in vivo and in vitro studies that the RBE can vary significantly [62], but there is no clear clinical data that indicates that the usage of 1.1 as the generic RBE value is unreasonable [63]. On the other hand, there is neither clear clinical data that confirms that an RBE of 1.1 is correct [7].

The RBE is closely related to the LET in the sense that the former increases as the latter increases. At an LET of approximately 100 keV µm^{-1}, the maximum RBE is about 3-8, depending on the level of cell kill. Beyond this LET value, the RBE declines due to cell overkill. This is because high LET particles are densely ionizing and will deposit more energy to the DNA than what is required to kill the cell, thereby decreasing the effectiveness. This effect is shown in Figure 2.7.

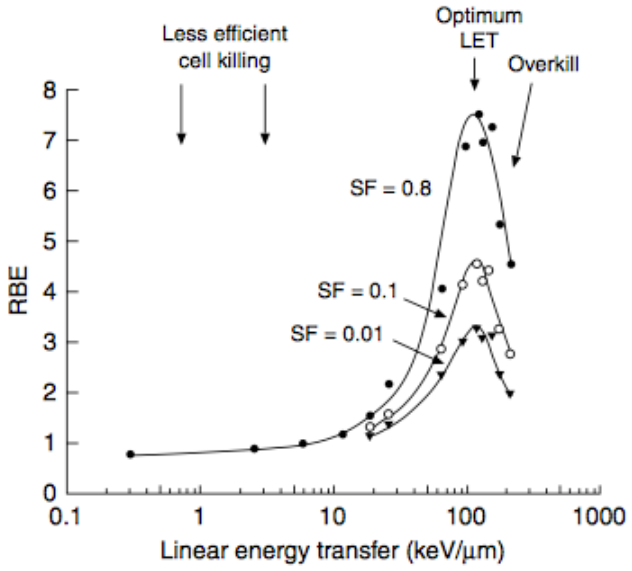

Figure 2.7: Illustration of the relationship between RBE and the mean LET. Notice that the RBE is relatively constant around 1 for low-LET particles as, for example, protons. SF is an abbreviation for survival fraction [54].

Chapter 3

Treatment Planning and Delivery

The aim of radiation therapy is to deliver the highest possible dose to the tumor while at the same time sparing healthy tissue. In order to do so, a well-planned treatment must be diligently chosen. In addition to the planning, plan evaluation, deliverance and quality assurance are highly important, even more so in radiation therapy with protons than photons, because of the protons' high dose conformity and tissue density dependence [31].

The impact of radiation on tumors and normal tissues can be measured by evaluating the tumor control probability (TCP) and the normal tissue complication probability (NTCP). The TCP and the NTCP are dose-response curves that depend on the dose delivered to the tumor and dose received by normal tissues, respectively. By plotting the dose-response curves, their relative position and shape can determine the possibility of delivering a sufficient amount of dose with an acceptable level of side effects. The distance between the two curves is called the "therapeutic window", and an important part of the development of radiation therapy is to be able to increase the size of this window [6]. Ideally, delivering zero dose to the healthy tissue while at the same time delivering all the dose to the tumor is the desirable situation [17]. However, this is not possible, and the compromise between the NTCP and TCP will always be an issue in radiation therapy.

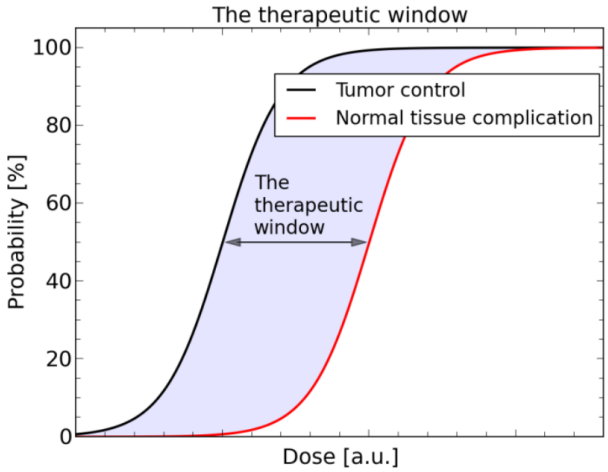

Figure 3.1: The therapeutic window separating the NTCP curve (red) from the TCP curve (black). Wider windows are preferable [17].

3.1 Treatment Planning

3.1.1 Image acquisition

During treatment planning for a cancer patient, precise quality images of the patient are required for assessing the extent and position of the tumor and possible organs at risk. Images are also needed to obtain tissue density information for accurate dose distribution calculations, and for precise patient setup.

The most common medical imaging modalities are computed tomography (CT), positron emission tomography (PET), magnetic resonance imaging (MRI), and ultrasound (US). While all four modalities have their advantages and disadvantages, CT is the gold standard in radiation therapy due to its ability to acquire tissue density information [64].

Computed tomography (CT)

CT utilizes X-ray photons (energy of $20 - 100\,\mathrm{keV}$) to create an anatomical image of the patient via X-ray attenuation.

Helical scanning, introduced at the end of the 1980s, revolutionized clinical imaging. By continuously scanning the patient, image acquisition duration could be drastically reduced, and thus, more accurate images could be acquired as a result of less motion artefacts. In helical scanning, the X-ray tube, emitting photons, rotates around the patient with one revolution taking less than a second. At the same time, the patient is moved through the gantry. The level of photon attenuation in the patient will depend on the material composition and the density of the area of penetration. The intensity of the transmitted photons is measured and counted by a bank of solid state detectors opposite the X-ray tube. By using a computer, the helical information can be translated to slice-by-slice information, i.e. data matrices of typically 512×512 or 1024×1024 pixels for each slice with a thickness of a few millimeters [64, 65].

The intensity of photons traversing matter can be calculated by the following formula:

$$I = I_0 e^{-\mu x} \ , \tag{3.1}$$

where I_0 and I are the initial- and measured photon intensity, respectively, x is the thickness of the matter in question and μ is the linear attenuation coefficient which expresses the amount of photons absorbed per cm. If the initial intensity is known, and the intensity of the photons that have penetrated the patient is measured, the attenuation coefficient can be obtained. The coefficient is highly dependent on the density of the traversed tissue. And so, by measuring the reduction in intensity, density information can be translated into a gray scale image. The darker the region of the image, the less attenuation has occurred, while the brighter regions represent tissues/organs having a relatively high density [64] (see Figure 3.2).

The Hounsfield units

In order to easily compare images obtained from different CT scanners, Godfrey Hounsfield introduced the Hounsfield units (HU), also referred to as CT numbers.

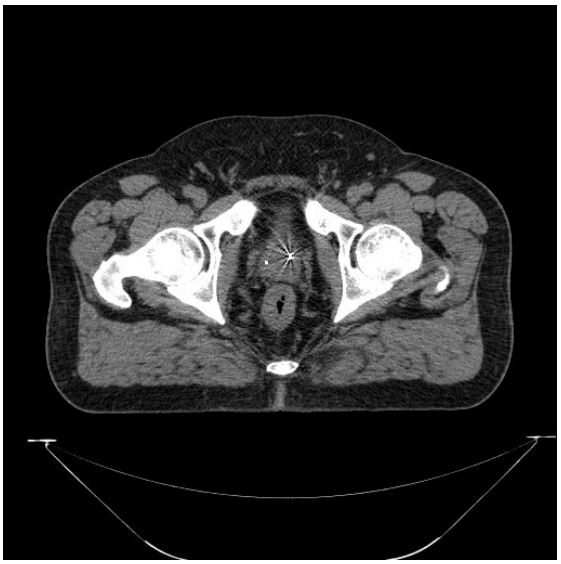

Figure 3.2: CT image of a prostate cancer patient acquired at Haukeland University Hospital. The white dots in the middle, lighting up in the image due to their very high density, are gold markers used for patient positioning. The measured Hounsfield unit for the markers was around 3000.

The HU scale is expressed relative to the linear attenuation coefficient of water which was assigned a Hounsfield unit of 0. He also assigned HU = 1000 to dense bone and HU = -1000 to air. The Hounsfield units are defined as [64]:

$$HU = \frac{\mu_{\text{tissue}} - \mu_{\text{water}}}{\mu_{\text{water}}} \times 1000 \ . \tag{3.2}$$

The Hounsfield units are directly related to the attenuation coefficient as a change of 1 HU equals a difference of 0.1 % between the attenuation coefficient of the tissue and the attenuation coefficient of water [65]. In proton therapy the HUs are further converted into relative stopping power values (relative to water) for proton range calculations. However, as uncertainties in HUs are linearly transferable to uncertainties in proton range calculations, an accurate conversion is highly important in proton therapy [7, 66] and will be further discussed in section 3.4.

The calibration curve

The density information, and thus the relative stopping power for particle therapy, is imported into the treatment planning system using a calibration curve (see Figure 3.3). The relationship between the Hounsfield units and the density/stopping power is typically acquired by calibration of the CT scanner using a phantom with substitute materials of known elemental composition [66]. The stopping powers can be determined by using a simplified version of the Bethe-Bloch equation [67] and may also be confirmed by direct measurements in proton beams [7].

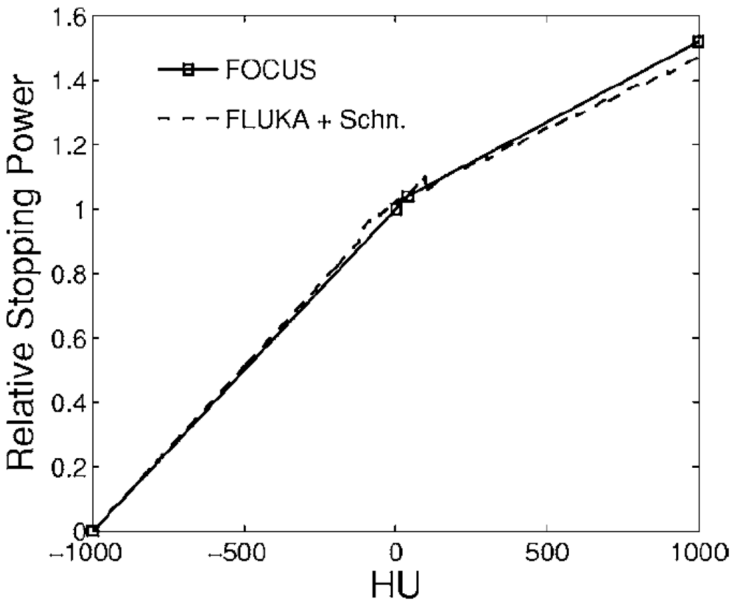

Figure 3.3: A typical HU to relative stopping power calibration curve used in proton therapy [68].

3.1.2 Anatomical volumes and target delineation

By acquiring an anatomical image of a patient, volumes of interest such as tumors and critical organs can be located and delineated. These are needed for prescription, recording, and delivery of the treatment plan. In ICRU Report 50 [69], targets and volumes used in radiation therapy are defined. Most of the volumes have the same definitions for both proton- and photon therapy. The exception is volumes that has specific treatment modality margins. These are specifically described in ICRU Report 78 [31] for proton therapy.

Prior to treatment planning, the two volumes that should be defined are the gross tumor volume (GTV) and the clinical target volume (CTV). Further volumes to be defined and delineated during treatment planning are the planning target volume (PTV) and the organs at risk (OAR). The anatomic regions of interest (ROI) are delineated by a radiation oncologist slice by slice, and while it is a time-consuming process, it is one of the most important ones [70].

Gross tumor volume (GTV)

ICRU defines the GTV as the *gross palpable or visible/demonstrable extent and location of malignant growth* [69]. The GTV typically consists of the primary tumor and other local metastases. The tumor cell density is always high in the GTV and therefore an adequate dose must always be delivered to the whole volume for radical therapy (curative treatment). The GTV's extent, shape, size, and location are determined by different means of diagnostic methods. This can be imaging using CT, MRI, PET, etc. and/or by clinical examination, for example, palpation, endoscopy and so forth. Depending on what method is used for GTV

determination, the GTV can be quite different in size and shape. It is therefore important to indicate the determination method used.

Clinical target volume (CTV)

Even though the whole macroscopic tumor has been delineated, surrounding tissue close to the GTV typically contains subclinical malignancy in the form of individual malignant cells, small cell clusters, or micro-extensions that can not be clinically detected. In ICRU Report 50 [69], the CTV is defined as *a tissue volume that contains a demonstrable GTV and/or subclinical microscopic malignant disease which has to be eliminated. This volume thus has to be treated adequately in order to achieve the aim of therapy, cure or palliation.* The CTV delineation is based on available data on the probability that malignant cells are located outside the GTV and on individual judgment by the radiation oncologist. The CTV, in addition to the GTV, are purely clinical-anatomical concepts, meaning that they are defined without regard to movement of the tissues and/or patient.

Planning target volume (PTV)

Variations in beam sizes and directions, in size and shape of tissues containing the CTV, movement of the CTV due to e.g. respiration, in addition to potential patient setup errors, calls for an additional margin to the CTV. By adding this margin, a new volume is defined by ICRU [31]: *The planning target volume is a geometrical concept, and it is defined to select appropriate beam sizes and beam arrangements, taking into consideration the net effect of all the possible geometrical variations, in order to ensure that the prescribed dose is actually absorbed in the CTV.* By adding an extra margin to the CTV, significant deviations from the prescribed dose in any part of the CTV are kept to a minimum. In proton therapy, beams can be designated directly to the CTV, taking into account the margins within the aperture design, without referencing the PTV. However, a PTV must always be defined due to the requirement of reporting purposes, and as a result, each CTV will always have a corresponding PTV.

Organ at risk (OAR) and planning organ at risk volume (PRV)

When creating a radiation plan for a patient, normal tissues and organs that have such a high sensitivity to radiation that they can significantly influence the treatment planning and/or the prescribed dose, should be delineated. These volumes are called organs at risk (OAR). Similarly as for the PTV, an additional margin is added to the OAR in order to ensure that adequate sparing of the OAR is achieved with a high probability. This leads to the concept of the planning organ at risk volume (PRV). It is designed to help treatment planning and evaluation. The uncertainties that need to be taken into account for the PRV are the movement of the OAR during treatment, variation in patient positioning, mechanical uncertainty of equipment, transfer setup errors from CT to the treatment unit, and human factors [31, 69].

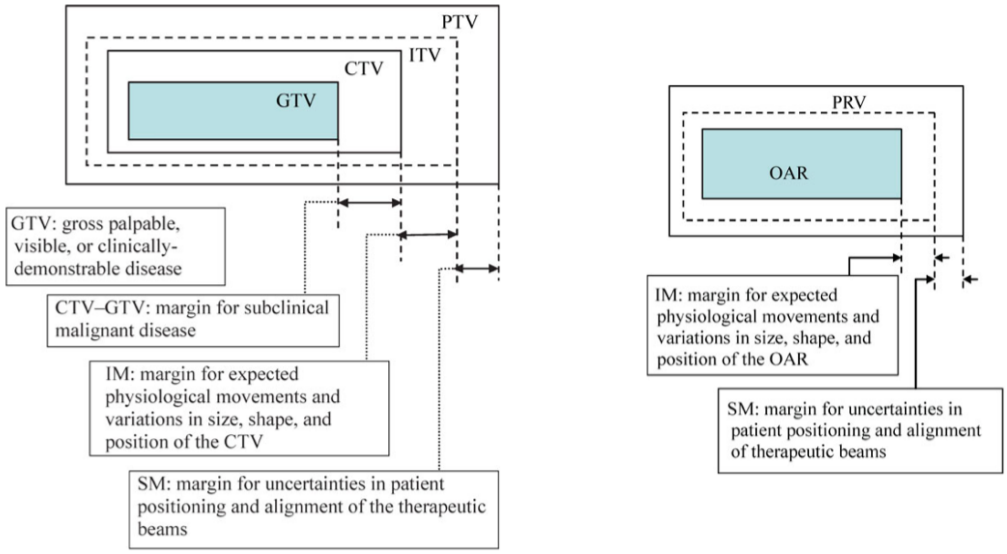

(a) Illustration of the volumes and margins related to the definition of the target volume.

(b) Illustration of the volumes and margins related to the definition of organs at risk.

Figure 3.4: Volumes and margins in proton therapy as defined in ICRU Report 78 [31].

3.1.3 Dose planning

After anatomical images have been acquired, and target and organs at risk have been delineated, the task of finding an appropriate treatment plan for the patient can start. The CT images which are a virtual representation of the patient can be imported, together with the outlined volumes, into the treatment planning system available for the clinic. Typically, a radiation oncologist prescribes planning aims, i.e. dose requirements and normal tissue constraints to the target volume(s) and OARs, respectively. These planning aims are based on detailed evaluation of the patient, diagnostic studies and other oncological concepts. The treatment planner uses the planning aims as a basis for finding an acceptable compromise between the dose to the target(s) and the OARs [7].

The preferable method of dose planning in particle therapy is the so-called inverse planning. The treatment planner can specify the number of beams, where each beam is defined by its specific parameters such as modality, field weight, beam angle and so forth. The treatment plan can then further be simulated in the TPS. Numerous simulations are conducted, where a computer algorithm evaluates which plan fulfills the treatment prescription to a maximum extent [31], by for example analyzing the therapeutic window, or by other methods. This is referred to as plan optimization. The optimized plan must, in the end, be evaluated. The optimization- and evaluation processes are further discussed below.

In treatment planning, it is always important for the planner to know the

limitation of the TPS. The analytical dose calculation algorithms utilize certain approximations which may lead to shortcomings in the accuracy of the calculated dose [7]. Most semi-empirical dose calculation algorithms in use are different variations of the pencil beam (PB) algorithm developed by Hong *et al.* [14]. The dose distribution from a PB with a given energy is represented by the product of a lateral profile term and a PB central axis depth dose term, obtained through measurements of broad beam data in water. The dose at any point in the patient is calculated by summing the dose contribution from all the PBs surrounding the point of interest. The lateral spread of the pencil beams is assumed to be describable by a function with Gaussian characteristics [70, 71].

3.1.4 Treatment plan optimization

The method of inverse planning is typically used for intensity-modulated particle therapy (IMPT). IMPT in pencil beam scanning means that the scanning magnets can steer the pencil beam and conform the dose in the transverse plane (see section 3.3.3). Dose conformation in this plane is also achievable for photons by IMRT or VMAT. However, due to the Bragg peak of protons, an additional degree of freedom is introduced, meaning that modulation along the beam axis is possible. In IMPT, each pencil beam must be weighted relative to each other and must be optimized separately [31]. The optimization process is an important part of the treatment planning. Optimization is essentially to iteratively generate, followed by automatically assessing, a large number of plans and choosing the best among them. A computer is given constraints and objectives on targets and organs at risk by a clinician. If given constraints, the computer must follow these without violation. Objectives, on the other hand, are typically given weights relative to each other, in which case a small violation may be allowed. An example of objectives can typically be 60 Gy to 98 % of the tumor volume, while no more than 20 Gy should be received by 30 % of a nearby OAR. When the computer have calculated the best plan for the given constraints, it should be inspected by the treatment planner. If the results are unsatisfactory, the objectives and constraints can be edited and a new optimization process may be initiated [31].

Biological optimization

As written in chapter 2, treatments in proton therapy usually assumes a constant RBE of 1.1. This means that converting the physical to biological dose is done by multiplying the former with the RBE. Consequently, the optimization can be performed based on the physical dose alone. However, as the RBE is closely related to the LET, which increases at the distal end of the Bragg curve, there are indications that the use of a constant RBE may not be the best approach [62].

Therefore a shift from optimization based on physical dose, to optimization based on physical dose *and* LET to account for a variable RBE may be a better method [7]. One approach to biological optimization has been suggested by J. Wilkens and U. Oelfke [72].

3.2 Plan Assessment

A treatment plan is evaluated by several different methods. Usually, dosimetrics and volumetrics are inspected using dose distributions displayed onto patient CT scans, and graphically using dose volume histograms alongside predetermined dose constraints to target volumes and organs at risk [31].

3.2.1 Dose distributions

Two methods of displaying the dose distribution are either via two-dimensional isodose curves or by a color wash overlaid on the three-dimensional CT images. The color wash display of the dose gives the most qualitative representation of the dose distribution. The dose distribution can typically be displayed in any two-dimensional plane, with the transverse, sagittal or coronal plane being the most common ones. In order for the dose distribution to be a good representation, a well-defined color bar should be used, where typically cooler colors (purple, blue) depicts lower dose, and warmer colors (yellow, orange, red) means higher dose. As there is no satisfactory way to evaluate the dose distribution in three dimensions in a single view, often, simultaneous displays of the dose distribution in different planes are used [31, 73].

While the display of the dose transposed over the CT images gives a fast impression of how the dose is distributed, it can be quite difficult to properly evaluate treatment plans in terms of the amount of dose organs and targets receive. Dose distribution display may also not be ideal for comparison purposes.

3.2.2 Dose volume histograms

Dose volume histograms (DVH) are a simple way to evaluate the dose distribution on volumes of interest. Cumulative DVHs, showing the amount of dose up to a given value received by a fraction of the total volume, are the most common type of dose volume histograms. The DVHs can employ both relative and absolute doses and volumes. By using DVHs for plan assessment and comparison, the spatial information is lost. This loss of spatial information can, however, be compensated for by using dose distribution displays in conjunction with the DVHs [31, 73].

3.3 Treatment Delivery

3.3.1 Accelerators in particle therapy

In order to use protons for therapeutic purposes, they first need to be accelerated up to the desired energy, a task that is done by particle accelerators. In particle therapy, the two main types of accelerators are the cyclotron and the synchrotron. For protons, an energy of typically about $230-250\,\mathrm{MeV}$ is needed for a radiation depth of $30\,\mathrm{cm}$ in tissue [13]. This can be achieved using both mentioned accelerators. However, for heavier ions, their high magnetic rigidity can be a problem for

cyclotrons. Therefore, with today's technology, synchrotrons are the accelerators used for particles heavier than protons.

The big advantage of cyclotrons, compared to synchrotrons, is that they can provide a continuous particle beam. Cyclotrons can however only accelerate particles to a fixed energy, and thus a degrader must be used to vary the beam energy in order to create a SOBP. Protons coupled with two electrons are accelerated to therapeutic energies by an applied radio frequency wave inside the cyclotron. The trajectories are further bent by a strong magnetic coil making the particles travel in spiral shaped paths with increasing radius. When the particles reach the desired energies, the electrons are removed and the protons are extracted from the cyclotron. They can then be used for particle therapy [7].

For acceleration to therapeutic energies of heavier particles than protons, a cyclotron will not suffice. A much larger accelerator, the synchrotron, is needed. One or more linear accelerators are necessary for particle pre-acceleration before entering the synchrotron. The synchrotron can provide very high particle energies by having a large radius, and by increasing the strength of its magnetic bending fields. Unlike for the cyclotron, the energy the particles accelerated in the synchrotron can be adjusted within the accelerator itself [7].

3.3.2 Energy modulation

A monoenergetic beam from the accelerator is unsuitable for cancer treatment due to its longitudinally narrow Bragg peak. In order to cover the target volume in its full depth, beams of decreasing energy, and typically decreasing weight, are combined to create the spread-out Bragg peak (see Figure 1.1). This modulation can be done either actively or passively [7].

Active modulation

Active modulation is only possible for synchrotrons. The energy of the beam is changed directly within the accelerator and the energy change must happen quickly in order to limit the treatment duration and to allow for fast switching between treatment rooms. The energy selection must also be accurate in order to determine the depth of the Bragg peak with sufficient accuracy [7].

Passive modulation

For cyclotrons, only passive modulation is available. This is because these accelerators only work at a specific energy. Passive modulation is achieved by inserting material in front of the beam, thereby decreasing the effective energy, and thus the range of the particles. This can either be done immediately after the beam has been extracted from the cyclotron, or the modulation can take place directly inside the treatment nozzle [7].

To create the SOBP, either a plate with ripples (ridge filter) or a rotating wheel with varying thickness in the azimuthal direction (modulator wheel) is used. The modulators are designed such that the result is a predefined depth dose profile.

The SOBP can, in addition, be adjusted in depth by using an additional range shifter consisting a number of plastic plates with varying thickness [73].

3.3.3 Beam delivery techniques

In addition to spreading the dose over the target in the longitudinal direction, the dose must also be spread laterally. This can be done by different beam delivery techniques. The two major delivery techniques in particle therapy are referred to as active beam shaping (beam scanning) and passive beam shaping (beam scattering) [74].

Passive scattering

Passive scattering was the first method to be developed. In this delivery technique, the narrow particle beam is spread in the lateral direction either by using one scatter foil (single scattering technique), when small fields are requested, or two scatter foils (double scattering technique), when a broader beam is preferable [75]. The beam must additionally be shaped according to the target volume. Usually, collimators are used to adapt the field for each separate treatment angle [74]. An illustration of the passive scattering technique is shown in Figure 3.5a.

The main advantage of passive scattering is that the change of energy between the different layers is achieved much faster than the scanning technique. Considering that the whole field is delivered almost at once, the complete treatment duration will also be shorter [76]. However, a large disadvantage of the passive scattering technique is the fact that subsidiary dose to the patient may occur due to the additional collimation material in the beam line. This can lead to more nuclear fragments [74].

Pencil beam scanning

Pencil beam scanning uses magnets to deflect, focus and steer the charged particles in the beam. The magnets consist of two dipoles, run by fast power suppliers; one for horizontal steering and one for vertical steering. This way a narrow beam can be used to "paint" the dose over the target, layer by layer. When one layer of voxels has been irradiated, the energy of the beam is decreased, and a new layer can be treated [77]. The voxels, or spots, can be irradiated one by one (discrete spot scanning) meaning that the beam is turned off between the irradiation of each spot. Another method is the so-called raster scanning technique where the beam continuously irradiates while the dipoles are simultaneously steering the beam [75]. In pencil beam scanning, it is highly important that beam intensities and beam positions are monitored in order to ensure a safe and accurate delivery of the dose to the patient [73]. The main advantage of pencil beam scanning is its high dose conformity compared to the passive scattering technique, and as a consequence, lower doses to healthy tissues may be achieved. There will also be no additional dose due to nuclear fragmentation from beam shaping materials [74]. The method of pencil beam scanning is shown in Figure 3.5b.

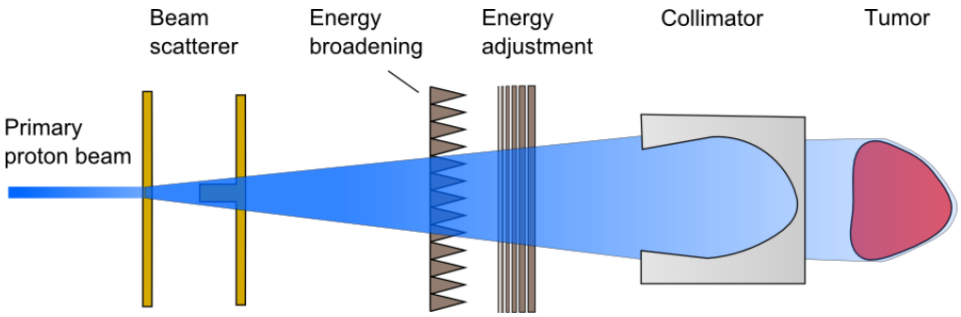

(a) Schematics of the passive scattering technique. Scattering foils are used for beam broadening while a collimator is used for beam shaping.

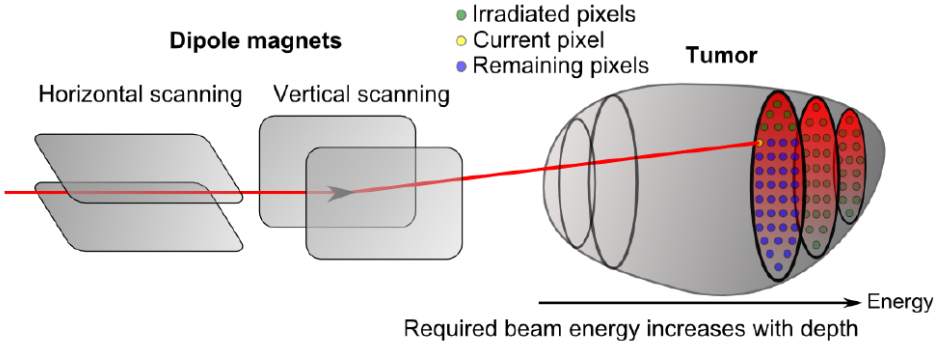

(b) Illustration of the pencil beam scanning technique. Dipole magnets are used to steer the beam in both the horizontal- and lateral direction.

Figure 3.5: The two main delivery techniques used in particle therapy [17].

3.3.4 The rotating gantry

By using fixed beams in radiation therapy, either a horizontal beam, a vertical beam, or both, the direction of the beam relative to the patient may be manipulated by rotating the treatment table in different angles, or by turning the patient relative to the treatment table. However, by only rotating the patient and the treatment table, there are some limitations. By delivering the beam via a rotating gantry, and (optionally) simultaneously rotating the patient, a higher degree of freedom for the beam delivery angles relative to the patient and the tumor can be achieved.

The gantries in proton therapy are rather large mainly due to the big and heavy magnets that are needed to bend the proton tracks with a sufficient radius of curvature. For protons, this curvature is typically around 1.5 m. Gantries as large as 10−15 m in length, with a radius of about 5−6 m and weighing as much as 100−200 t are not uncommon [71].

3.4 Uncertainties in Particle Therapy

The finite range and sharp distal dose fall-off are the biggest advantages of protons in radiation therapy [12]. However, these advantages are at the same time their

biggest disadvantages with respect to uncertainties. The finite range and the strong energy-range relation make the protons highly susceptible to tissue density variations and uncertainties [21]. Further, the relatively high dose increase in the Bragg peak and the sharp dose-response curve may result in a significant change in the TCP and/or the NTCP. Keeping the uncertainties to an absolute minimum in particle therapy can be challenging and must have a high priority. Commercial treatment planning systems available today are not able to display consequences of uncertainties for the treatment plans. A physician in treatment planning must always be aware that the dose distribution displayed by the TPS is not necessarily the actual dose distribution delivered to the patient, and must therefore be able to make mental assessments of the consequences of the dose uncertainties [7]. Additional margins for the proton beam range are typically added for range uncertainty assessment. These margins often differ from treatment center to treatment center, but are generally around $2.5-3.5\,\%$ of the proton range with an additional 1 mm margin [21].

3.4.1 Patient alignment and setup

Acquiring images of the patient should be done in the same patient position as for the actual treatment. Patients are often immobilized on the treatment table in order to minimize patient movement. External markings on the patient's skin, in addition to bony anatomy or implanted fiducials can be used for alignment. A well-executed patient positioning procedure is essential for the reduction of uncertainties [70]. The accuracy of the patient position should be about $1-2\,\text{mm}$, with an emphasis on avoiding nearby critical structures [7].

3.4.2 Tissue heterogeneities

Tissue heterogeneities can substantially alter the proton beam range. Therefore, it is important to select beam directions that try to avoid anatomical regions of the patient that contain complex or high-Z heterogeneities and large air cavities. Beam directions that require protons to stop right in front of critical organs should also be avoided [7]. It is not only the range of the proton beam that is affected by tissue heterogeneities. Multiple Coulomb scattering is the main cause of Bragg peak degradation and may alter the shape of the dose distribution by a factor not negligible from a clinical aspect [29]. Nuclear scattering may also contribute to as much as $5\,\%$ of the change in the width of the distal dose fall-off, but is however only slightly dependent on the complexity of tissue heterogeneities [78].

Analytical treatment planning algorithms are not able to correctly predict the Bragg peak degradation resulting from multiple Coulomb scattering, mainly due to their simplified algorithms [21]. Heterogeneities in the patient can, therefore, contribute to uncertainties in particle therapy.

3.4.3 CT conversion uncertainties

The relationship between the linear attenuation coefficient for photons, used to obtain Hounsfield units during a CT scan, and the relative stopping power of

protons is quite complicated and difficult to analytically evaluate with a sufficient accuracy. The relative stopping power depends primarily on the elemental composition, the mean ionization energy, and the physical density, of the material. There are two main ways of converting HUs to relative stopping powers; the stoichiometric method [67] and the direct-fit method [79]. Without going into details, both methods rely on converting Hounsfield units, acquired in a CT scanner using photons in the kilovoltage range, to relative proton stopping power. This conversion is not trivial and can lead to uncertainties. The acquisition of the HUs themselves can also lead to uncertainties as these units depend on the CT scanner's tube voltage, filter and other machine variables [66].

3.5 Monte Carlo Simulations

The Monte Carlo (MC) method is considered the most accurate procedure of simulating particle interactions in a medium [32]. By applying random sampling of possible outcomes of different interactions and physical processes calculated from probability distributions, the MC method can mimic real life interactions at the atomic level on a particle-by-particle basis. The probability distributions are obtained from experimental measurements or from models of particle transportation. The particles are simulated one by one, a single step at the time, where a probability distribution is sampled from, at each separate step. The physical event (absorption, annihilation, direction change, energy change etc.) occurring at each step determines the next step of the particle. If secondary particles are produced, these need to be tracked as well. After a particle, in addition to possible secondary particles, has been absorbed, a new particle can be simulated [7].

In order to achieve a given accuracy in MC simulations, a sufficient number of particles must be simulated. The precision of Monte Carlo results depends on the number of histories (N) and is proportional to the function $1/\sqrt{N}$. Therefore, by increasing the number of histories, the computation time will also increase, possibly making the MC simulation very time-consuming. The uncertainty of a MC simulation also depends on the number of steps each particle takes. In dose calculation, the maximum step size is limited by the CT voxel size. The reason for this is that the physical processes that can occur are typically different for each voxel because the material composition and density are different. A possibility to decrease the computation duration would be to combine voxels and averaging the material composition and density between them. Another method would be to limit the particle tracking, meaning that if, for example, a secondary electron has an energy below a certain value, the dose will be deposited at the point of emission rather than to track the whole trajectory of the electron [71].

There are several different Monte Carlo codes available for dose calculation. Most of them were developed in physics laboratories and later adopted for medical use. As this project will use FLUKA [40, 41], a general purpose Monte Carlo tool, for its simulations, this specific MC tool will be further outlined below.

FLUKA

FLUKA is a multipurpose Monte Carlo code that can simulate the interaction and propagation of about 60 different particles with high accuracy. This includes photons and electrons from 1 keV to several thousands of TeV, hadrons up to 20 TeV, neutrinos and muons of any energies, among several other different particles. FLUKA is also able to track particles in electric and magnetic fields. FLUKA can be used for a range of different applications including proton and electron accelerator shielding, calorimetry, dosimetry, detector design, cosmic ray simulations and neutrino physics. Microscopic models are the basis of FLUKA where conservation laws are enforced at every single step to ensure consistency among all reaction steps and reaction types. The results are checked and benchmarked to experimental data at single interaction levels. This enables predictions with a minimal set of free parameters, and as a further consequence, results in complex cases and scaling laws arise naturally from the underlying physical models, providing predictivity where experimental data is absent [40].

The FLUKA input

FLUKA relies on an input file in order to perform simulations. The file is written using an ASCII standard where the user can provide different commands, by using the standard FLUKA cards. A typical structure of a FLUKA input file may be as follows [40]:

- Titles and comments for documentation purposes.
- Description of the problem geometry.
- Definition of materials.
- Material assignments.
- Definition of the particle source.
- Definition of the requested detectors to score physical quantities as dose, fluence, energy, etc.
- Definition of biasing schemes.
- Definition of problem settings such as energy cutoffs, step size, physical effects not simulated by default, particles not to be transported, etc.
- Initialization of the random number sequence.
- Number of requested histories.

For more advanced simulation setups that the regular input file is not capable of handling, a number of FLUKA user interface routines are available.

CT images in FLUKA

FLUKA is capable of describing complex geometries in terms of voxels, i.e. small parallelepipeds of equal size, forming a three-dimensional grid. This can be useful when performing dosimetric calculations in FLUKA. Flair [80], FLUKA's graphical user interface is capable of handling the importation of DICOM CT images directly (see the next section for an explanation of DICOM files). In the Flair DICOM interface, the Hounsfield unit in each voxel can be converted to material density and elemental composition using material tables provided by the user. The default conversion tables in FLUKA are based on the work of Schneider *et al.* [81], and further extended by Parodi *et al.* [82] (more information in section 4.8). By handling this information, Flair converts the CT images into a so-called voxel file that can be further used in FLUKA for patient dosimetry.

For more information about the specifics of FLUKA, the reader is referred to the FLUKA manual [83].

3.6 The DICOM File Format

There are many different medical equipment manufacturers, and therefore a standard format for storing medical information was needed. The standard DICOM format simplifies the exchange of medical data between equipment and software developed by different manufacturers. The DICOM files contain necessary information needed to execute radiation therapy on patients. Everything from images of the patient's anatomy, to coordinates of the regions of interest, beam energies, gantry angles and so forth. Flair is, as of version 2.1-8, only able to directly import DICOM images, containing the HU information. All other information necessary to perform dose recalculations in FLUKA must be manually converted to a FLUKA readable format.

The DICOM files store information mainly by using datasets, which are derived from dictionaries in Python. They are a collection of key-value pairs, where the key is the DICOM tag, and the value is a data element(s). By using the Pydicom library, these datasets are easily accessible. Below is a small excerpt of a DICOM dose file showing how a DICOM file is structured. The first column gives the tag numbers, the second provides the tag names, the third column specifies the data types (string, integer etc.) while the fourth column represents the data element(s):

Listing 3.1: "Example of data and format of a DICOM RT Dose file."

```
(0008, 0012) Instance Creation Date          DA: '20160416'
(0008, 0016) SOP Class UID                   UI: RT Dose Storage
(0008, 0018) SOP Instance UID                UI:
   1.2.826.0.1.3680043.8.176.2016416103318991.11.5678144388
(0008, 0060) Modality                        CS: 'RTDOSE'
(0008, 103e) Series Description              LO: 'Beam dose(s) for plan
   270dgProton'
(0008, 1090) Manufacturer's Model Name       LO: 'RayStation'
(0010, 0010) Patient's Name                  PN: 'PHANTOM_1^WATER'
(0018, 0050) Slice Thickness                 DS: '2'
(0020, 000d) Study Instance UID              UI:
   2.25.338943507792393627692024455029958395970
(0020, 0032) Image Position (Patient)        DS: ['-124', '-124', '-124']
(0028, 0008) Number of Frames                IS: '125'
(0028, 0010) Rows                            US: 125
(0028, 0011) Columns                         US: 125
(0028, 0030) Pixel Spacing                   DS: ['2', '2']
(3004, 0002) Dose Units                      CS: 'GY'
(3004, 0004) Dose Type                       CS: 'PHYSICAL'
(3004, 000a) Dose Summation Type             CS: 'BEAM'
(3004, 000e) Dose Grid Scaling               DS: '3.1164414806E-05'
(300c, 0002) Referenced RT Plan Sequence 1 item(s) ----
   (0008, 1150) Referenced SOP Class UID       UI: RT Plan Storage
   (0008, 1155) Referenced SOP Instance UID    UI:
      1.2.826.0.1.3680043.8.176.2016416103318990.7.5040860386
        ---------
(7fe0, 0010) Pixel Data                      OB or OW: Array of 3906250
   bytes
```

3.6.1 CT Image and RT Structure Set

The DICOM CT Image files contains information about the patient's anatomy acquired from a CT scan. The density information, necessary for treatment planning, is stored as HUs in a two-dimensional array, called a pixel_array (NumPy array). The CT images are stored as a series of files. One file for each planar slice in the DICOM coordinate system's z-direction, where each file contains a separate pixel_array. All files put together in the correct order result in a three-dimensional grayscale image of the patient. Furthermore, information about the dimensions of the pixel_array, in addition to the size of each pixel and the position and orientation of the patient on the imaging table are contained in the DICOM CT Image files. All the mentioned information is necessary to perform dose calculations.

A second DICOM file containing relevant information for radiation treatment is the RT Structure Set. This file defines a set of regions of interest (ROI) that are essential in radiation therapy, such as body contours, PTVs, GTVs and OARs. Information about the coordinates of the structures and the corresponding color codes for the delineation lines are located in this DICOM file. The structures can

for example be useful to visualize the dose deposited to PTVs and OARs and they are also necessary in order to calculate dose volume histograms.

3.6.2 RT Plan and RT Dose

The DICOM RT Plan file is the main pillar for performing dose recalculations. In this file, most information about the TPS calculated treatment plan is located. This includes treatment beams, dose prescription, accessories used (range shifter, lateral spreading device etc.), patient setup, gantry angles, isocenter position in the DICOM coordinate system, along with much more.

The RT Dose files contain the dose distribution calculated by the TPS, along with other dosimetric details. The dose is also contained in a pixel_array, as for the CT image. A single dose file is created for each field used in the treatment. This means also that the dose pixel_array is three-dimensional, as opposed to the two-dimensional array of the CT images. TPSs also allow for exportation of an RT dose file containing the dose distribution from all the treatment fields combined. Information about the dose scoring regions along with the size of the scoring grid is also located in the RT Dose files.

For more details on the DICOM standard, the reader is referred to *DICOM - Information Object Definitions* by the National Electrical Manufacturers Association [84].

3.7 Coordinate Systems

In this project, there were several different coordinate systems to consider when performing coordinate transformations. These systems are outlined below.

3.7.1 The patient coordinate system

The patient coordinate system is defined by the International Electrotechnical Commission (IEC) in IEC 61217 [85] as having the positive x-axis toward the left arm of the patient, the positive y-axis towards the patient's head, and the positive z-axis towards the patient's chest. The patient coordinate system follows the orientation of the patient, meaning that if the patient is rotated relative to the patient table, the coordinate system will rotate accordingly. The patient coordinate system can be seen in Figure 3.6a.

3.7.2 The DICOM coordinate system

The DICOM standard coordinate system is defined with the positive x-axis toward the left arm of the patient, the positive y-axis towards the patient's back, and the positive z-axis towards the patient's head [84]. The DICOM coordinate system is also dependent on the patient orientation. The origin of the DICOM coordinate system is not necessarily located at the isocenter of the CT scanner. The location of the origin is machine dependent and can differ from scanner to scanner. The DICOM coordinate system is seen in Figure 3.6b.

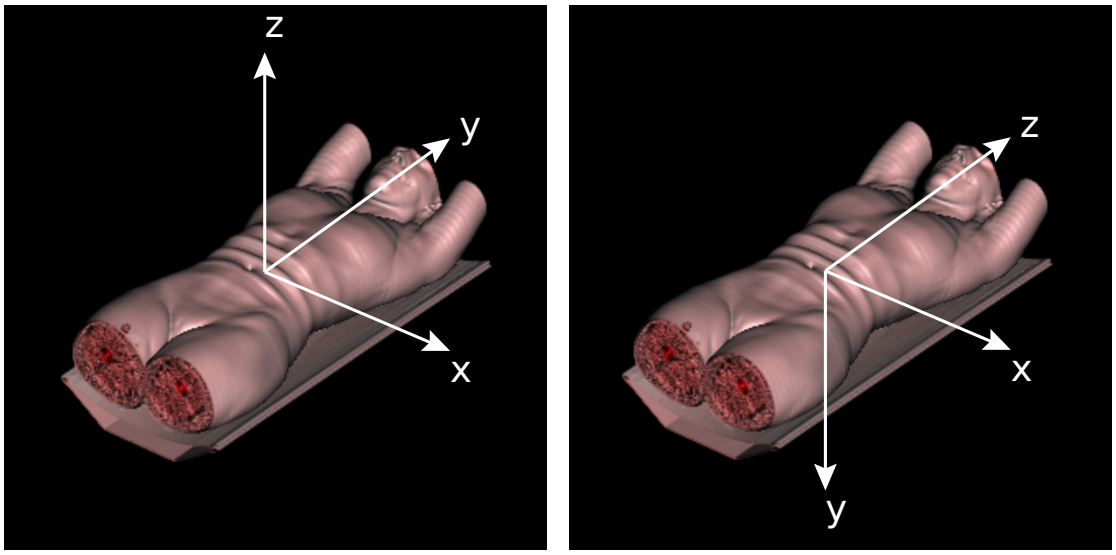

(a) The patient coordinate system. (b) The DICOM coordinate system.

Figure 3.6: The patient- and the DICOM coordinate system. 3D rendering of CT images from OsiriX [86]. Figures created by the author.

3.7.3 The treatment room coordinate systems

The different coordinate systems in the treatment room are also defined in IEC 61217 [85]. They are a set of systems that are described in relation to their mother coordinate systems. The systems in the treatment room, not used in this project, will not be explained. The fixed system is the uppermost system in the treatment room hierarchy, where the isocenter is located at the origin. Its daughter coordinate system is the IEC Gantry system. It coincides with the fixed system for a gantry angle equal to zero. If the gantry rotates, the coordinate system rotates with it. The isocenter for the gantry system is also located at it origin. The fixed- and the gantry coordinate systems are shown in Figure 3.7.

3.7.4 Patient orientations

Patients located on the imaging (and treatment) table can be oriented in different directions, depending on what orientation is the most advantageous for treatment. The most common orientation is the head first - supine (HFS) orientation where the patient's head is positioned toward the front of the imaging equipment, facing upwards. There are however seven more orientations which are shown in Figure 3.8.

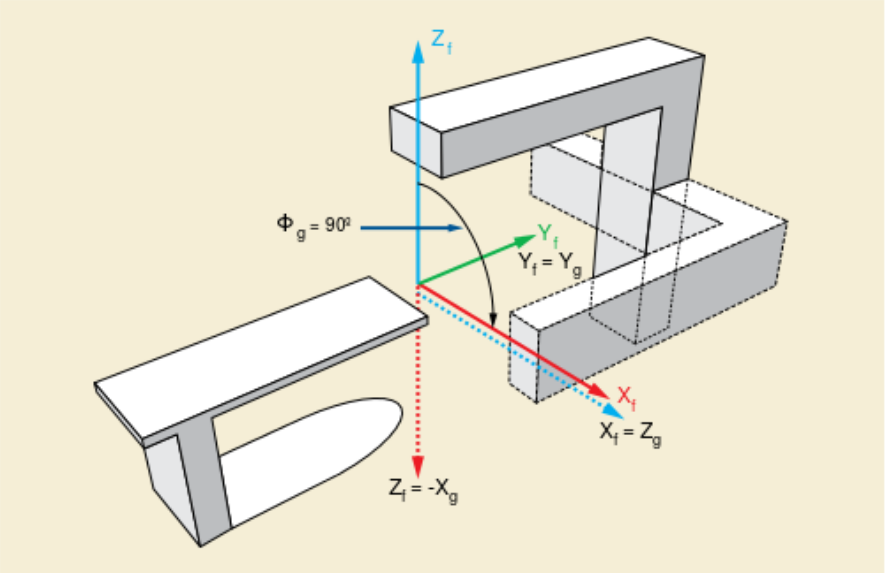

Figure 3.7: The coordinate systems in the treatment room: the fixed system and the gantry system. Subscript f means fixed, and subscript g means gantry, for the axes in the figure. These two correspond when the gantry angle is zero. If the gantry angle, for example, were to be 90°, the positive z-direction in the gantry system would point in the same direction as the positive x-direction in the fixed system [84].

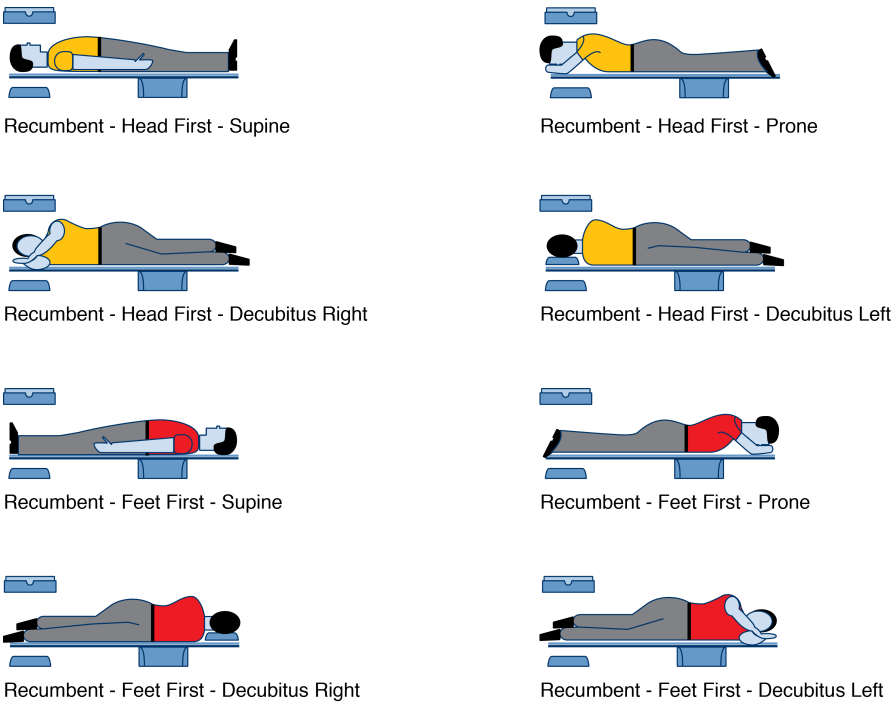

Figure 3.8: The different patient orientations in radiation therapy. The most common one is the head first - supine orientation [84].

Chapter 4

Methods and Tools

The main purpose of this project was to develop a tool to enable FLUKA Monte Carlo recalculations of dose distributions initially calculated by commercial treatment planning systems (TPS). A further aim was to enable comparison between the FLUKA and the TPS dose distributions. The tool had to be able to handle data translation between the TPS and FLUKA which required transferring of the treatment plan and imaging information, in addition to plotting and displaying dose distributions. The TPS data, which are stored in the DICOM file format, was read, extracted and translated using Python [87] (v2.7) programming language in combination with the Pydicom [88] (v0.9.7) library. To plot and compare two-dimensional dose distributions, in addition to one-dimensional dose curves and dose volume histograms, Python was used in conjunction with the NumPy [89] (v1.8.2) and Matplotlib [90] (v1.3.1) libraries. The processes to obtain the input data for FLUKA, and to perform comparisons are illustrated in Figure 4.1. DICOM files are exported from the TPS. These files are further run through scripts that obtain treatment information needed by FLUKA to perform dose recalculations. FLUKA scores e.g. the dose which can be plotted as a two-dimensional distribution transposed over the CT images. The DICOM files are directly utilized to display the TPS dose distribution. Further, a visual comparison between the dose distributions can be made. A comparison between the two dose distributions can also be made by subtracting the TPS dose from the FLUKA dose. In addition to the two-dimensional dose, one-dimensional depth dose curves and transversal doses can be plotted, both from FLUKA and the TPS. The FLUKA dose can also be converted to a DICOM RT Dose file which can be further used to create dose volume histograms or be imported into different DICOM handling software.

4.1 Defining the FLUKA Coordinate System

When importing DICOM images into FLUKA, the patient will be oriented in FLUKA according to the DICOM coordinate system only for the HFS orientation. As a result, the coordinate system will not rotate according to the orientation of the patient, which means that the positive y-axis in FLUKA will always point towards the treatment table/floor. In FLUKA, the patient can be rotated and translated to another coordinate system definition, if desirable. In this project, it was chosen not to rotate the patient in the FLUKA coordinate system, and it was further decided to use the isocenter definition of the gantry system (isocenter at the origin). In conclusion, the coordinate system in FLUKA will consist of

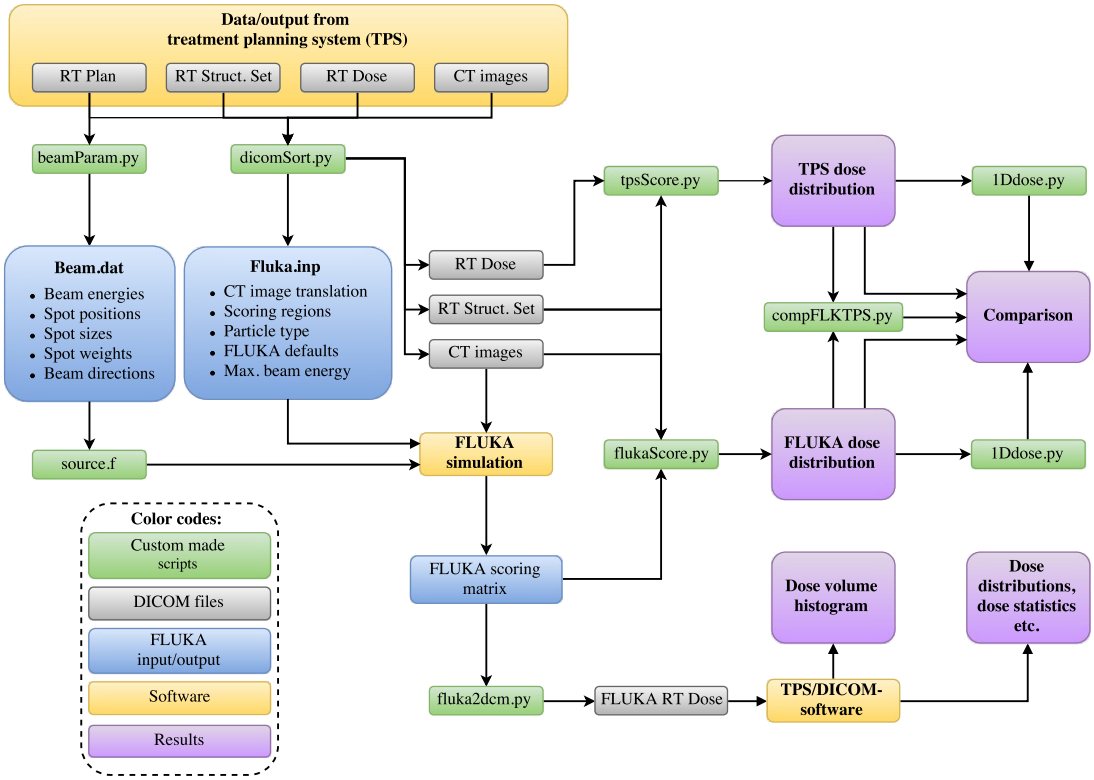

Figure 4.1: The workflow for dose verification with FLUKA. The custom made scripts (green boxes) enable dose recalculation in FLUKA and comparison to the original dose distribution. Treatment plans (DICOM format) from the TPS are run through the scripts which obtain relevant parameters and information required by FLUKA.

the axis definition of the DICOM coordinate system for the HFS position and the isocenter definition of the gantry coordinate system (see Figure 4.2). This coordinate system was also chosen for the dose-displaying scripts in this project.

Since the patient was set not to rotate in the FLUKA system, coordinate transformations had to be executed for the beam source itself according to the rotation of the gantry. These transformations are further explained below and are only valid for the HFS orientation. For the head first - prone (HFP) orientation some modifications had to be made, not explained in this method. Other orientations are not yet supported.

4.2 DICOM File Handling and FLUKA Input File

After a TPS has been used to calculate and evaluate a treatment plan, the DICOM files containing the treatment information, alongside the patient images, structures and dose profiles, can be exported from the treatment planning system. However, the naming convention used is in many cases not ideal for manual DICOM file handling, as it can be problematic identifying the type of DICOM file. If DICOM

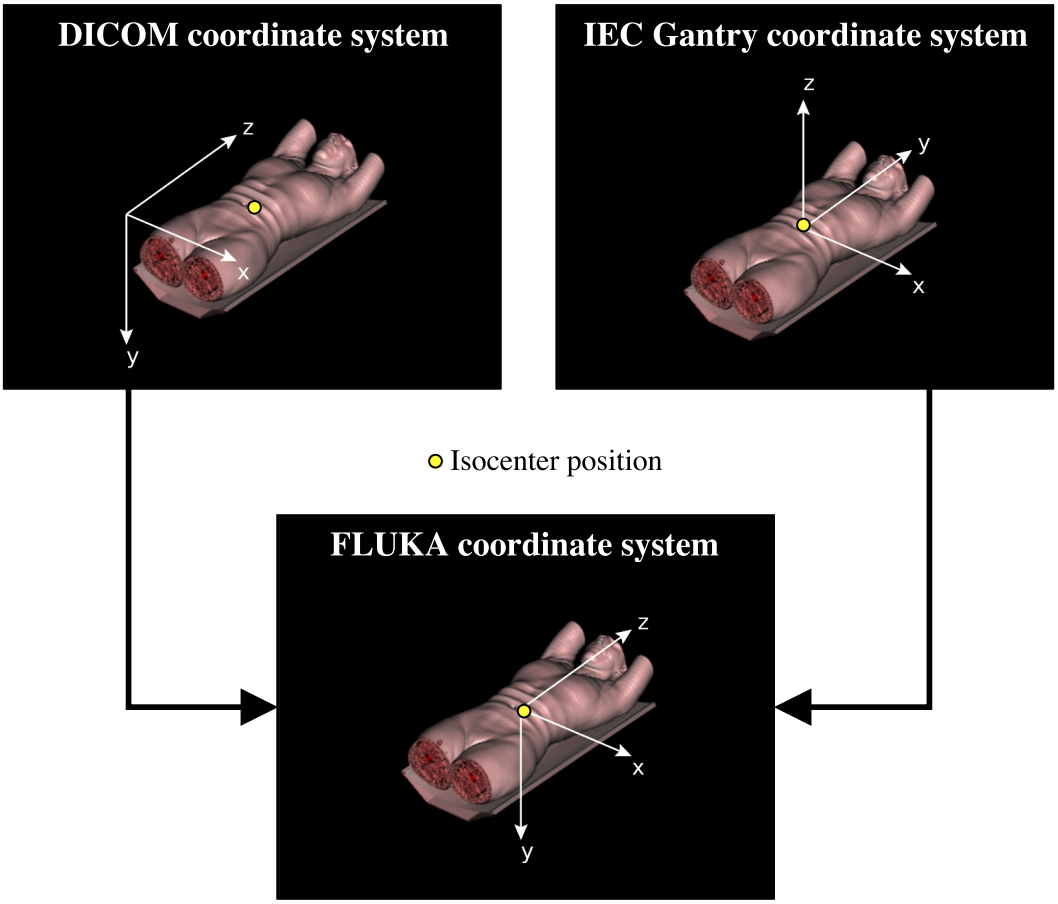

Figure 4.2: The DICOM coordinate system is merged with the IEC Gantry coordinate system to define the FLUKA system. The axes directions are taken from the former, and the isocenter position from the latter, denoted by the yellow dot. All orientations are HFS, gantry system is for 0° angle and the isocenter position and patient position in the DICOM coordinate system are only examples.

files are exported from a TPS, they are often further imported into another software that takes care of the file handling. The tool developed in this project, on the other hand, requires some manual handling of the DICOMs, mainly due to the lack of a graphical user interface. Therefore, a script that evaluates all the exported DICOM files was necessary. This script, called `dicomSort.py`, imports all the DICOM files, identifies what type each respective file is (image, plan, dose, structures), gives the files appropriate names, and stores them in a subfolder.

4.2.1 Automated creation of the FLUKA input file

To make the FLUKA recalculation procedure slightly more automated, the script `dicomSort.py`, in addition to sorting and renaming the DICOM files, is able to

automatically create the input file used by FLUKA based on relevant parameters contained in the DICOMs. These parameters, including the FLUKA default settings used, are explained below.

FLUKA defaults

FLUKA provides a set of default physics settings, making it simpler to choose the best settings for specific applications. The pre-defined settings have all been optimized for a particular type of application. The script defines what FLUKA defaults to be used for the recalculations. It provides the input file with a HADROTHErapy DEFAULTS card. The HADROTHErapy settings are optimized for hadron therapy physics, and are further outlined below:

- ElectroMagnetic FLUKA (EMF) on (transport of electrons, positrons and photons).
- Inelastic form factor corrections to Compton scattering and Compton profiles activated.
- Low-energy neutron transport on - thermal energies included (high energy neutron threshold at 20 MeV).
- Fully analogue absorption for low-energy neutrons.
- Particle transport threshold set at 100 keV, except for neutrons (1×10^{-5} eV).
- Multiple scattering threshold at minimum allowed energy, for both primary and secondary charged particles.
- Delta ray production on - 100 keV threshold.
- Restricted ionization fluctuations on, for both hadrons/muons and electromagnetic particles.
- Ratio between hadron/muon upper- and lower interval limits of dp/dx momentum loss set at 1.03. Amount of the kinetic energy to be lost in a step set at 2 %.

Maximum beam energy and particle type

Although the beam parameters for the treatment are separately imported using a FLUKA user routine (see section 4.3), an energy larger than the maximum energy of the beam is recommended to be issued to the FLUKA input file using the available BEAM card. This is because FLUKA uses the provided energy to set up tables for stopping powers, cross sections, etc. for the simulation [83]. If the value is not provided, crashes may occur.

The energy provided to the FLUKA BEAM card is set to 20 MeV higher than the maximum energy of the therapeutic beam. In addition, the radiation type (protons or ions) is read from the DICOM RT Plan and added to the FLUKA input file.

CT image translation and isocenter correspondence

As previously outlined, the FLUKA coordinate system defined in this project is a combination of the DICOM- and the IEC Gantry coordinate system (see Figure 4.2). The axes of the FLUKA system will automatically correspond to the DICOM axes (for the HFS orientation) when importing the CT images. The coordinates of the spot positions of the pencil beams used for treatment are defined using the IEC Gantry coordinate system. It was for this reason having the origin defined at the isocenter in FLUKA was desirable. In order to have corresponding isocenters, the voxelized CT images must be translated to the correct position in the FLUKA coordinate system.

The CT images can be imported directly using Flair, where they can be further positioned using the so-called VOXEL card. However, the positioning coordinates must be read and handled from the DICOM files. The necessary information for the CT image translation is given in Table 4.1.

Table 4.1: The table describes the parameters necessary to perform correct CT image translation in FLUKA in order to have isocenter correspondence between FLUKA and the gantry coordinate system.

Tag name [Variable name]	**Tag description**
`Image Position (Patient)` [*ImagePos*]	The x-, y-, and z-coordinates of the upper left hand corner (center of the first voxel transmitted) of the image, in mm. Located in the DICOM CT Image files.
`Isocenter Position` [*IsoPos*]	Isocenter coordinates (x, y, z), in mm. Specifies the location of the treatment machine's isocenter in the DICOM coordinate system. Located in the DICOM RT Plan file.
`Pixel Spacing` [*PixSpace*]	Physical distance in the patient between the center of each pixel, specified by a numeric pair, in mm. Located in the DICOM CT Image files.
`Slice Thickness` [*SliceThick*]	Nominal slice thickness, in mm. Located in the DICOM CT Image files.

When the required parameters have been obtained, the CT voxel images can be translated using the equations (4.1) below. Each equation refers to the position of the origin of the FLUKA "voxel cage", i.e. a region made of a single RPP (rectangular parallelepiped) encapsulating all the voxels in the CT images. It is highly important to translate the voxel cage correctly with millimeter precision, in order to have a perfect isocenter correspondence between the two coordinate systems.

$$
\begin{aligned}
x &= \frac{ImagePos[0] - IsoPos[0] - PixSpace[0]/2}{10} \,, \\
y &= \frac{ImagePos[1] - IsoPos[1] - PixSpace[1]/2}{10} \,, \\
z &= \frac{ImagePos[2] - IsoPos[2] - SliceThick/2}{10} \,.
\end{aligned} \tag{4.1}
$$

The *ImagePos* and *IsoPos* are 3-tuples containing x-, y- and z-coordinates. The z-coordinate (*ImagePos*[*2*]), also denoted slice location, must be acquired from the first slice, i.e. the slice with the lowest z-coordinate, in order to remap the patient correctly in the z-direction. The pixel spacing and slice thickness must be divided by 2 and subtracted from the coordinates because, when expressing their positions using coordinates, FLUKA refers to the corner of the voxels [91] whereas the DICOM standard refers to the center of the voxels [84]. Each equation is divided by 10 to obtain the answers in cm, the standard distance unit used by FLUKA.

4.2.2 TPS scoring region and grid

In order to properly compare the dose calculated by FLUKA and the TPS, a USRBIN card (defining scoring quantities and regions) in FLUKA should be created to score the dose over the exact same region and using the same number of scoring bins as the TPS, i.e. equivalent scoring grids. Table 4.2 provides the parameters in the DICOM RT Dose files needed to obtain the scoring grid. The `Isocenter Position` from Table 4.1 is also required.

After acquiring the information in Table 4.2, the scoring region in FLUKA can be defined using equations (4.2).

$$
\begin{aligned}
X_{min} &= \frac{DoseImagePos[0] - IsoPos[0] - DosePixSpace[0]/2}{10} \,, \\
Y_{min} &= \frac{DoseImagePos[1] - IsoPos[1] - DosePixSpace[1]/2}{10} \,, \\
Z_{min} &= \frac{DoseImagePos[2] - IsoPos[2] - DoseSliceThick/2}{10} \,, \\
X_{max} &= X_{min} + \frac{DoseColumns \times DosePixSpace[0]}{10} \,, \\
Y_{max} &= Y_{min} + \frac{DoseRows \times DosePixSpace[1]}{10} \,, \\
Z_{max} &= Z_{min} + \frac{DoseFrames \times DoseSliceThick}{10} \,.
\end{aligned} \tag{4.2}
$$

The *DoseImagePos* are 3-tuples containing x-, y- and z-coordinates. Again the pixel spacing and slice thickness must be subtracted and divided in half for the same reason as above.

Table 4.2: The table describes the parameters needed to score dose (or other quantities) in FLUKA over the same grid as the TPS. All parameters are located in the RT Dose files.

Tag name [Variable name]	**Tag description**
`Image Position (Patient)` (Dose) [*DoseImagePos*]	The x-, y-, and z-coordinates of the upper left hand corner (center of the first voxel transmitted) of the dose grid, in mm.
`Pixel Spacing` (Dose) [*DosePixSpace*]	Physical distance in the patient between the center of each pixel in the dose grid, specified by a numeric pair, in mm.
`Slice Thickness` (Dose) [*DoseSliceThick*]	Nominal slice thickness of the dose slices, in mm.
`Columns` (Dose) [*DoseColunms*]	Number of columns in the dose grid, i.e. the number of scoring bins in the x-direction.
`Rows` (Dose) [*DoseRows*]	Number of rows in the dose grid, i.e. the number of scoring bins in the y-direction.
`Number of Frames` (Dose) [*DoseFrames*]	Number of frames in a multi-frame image, i.e. the number of scoring bins in the z-direction.

4.3 Translating the Treatment Plan Information

The next step was to create a procedure for importing the beam parameters of the treatment plan into FLUKA using the `SOURCE` user routine. The framework of this file was provided by N. Bassler [92] and was further modified by the author of this thesis. The `SOURCE` routine is written in Fortran 77. It is used to sample primary particle properties from distributions that are too complicated to be described using the regular FLUKA input file [83]. Pencil beam scanning (PBS) is the state of the art treatment method for proton therapy [93], and therefore the tool developed in this project is only able to handle and process treatment plans for this specific technique. The PBS DICOM RT Plan file contains information about each spot used in the treatment, as the spot positions, weights, and sizes. The gantry angles and other treatment specific parameters are also located in the plan file. By using Python and Pydicom, a script called `beamParam.py` was developed. Its main objective is to create a simple text file containing the beam parameters depicted in Table 4.3. These variables are necessary to replicate the TPS calculated treatment plan in FLUKA.

The `Scan Spot Meterset Weights` can be directly written to the text file without any modification, whereas for the `Nominal Beam Energies`, the values must be converted from MeV to GeV, the standard energy unit for FLUKA.

Table 4.3: The parameters needed to import the TPS calculated treatment plan into FLUKA. All parameters are obtained from the DICOM RT Plan, if not stated otherwise.

Tag name [**Variable name**]	**Tag description**
`Nominal Beam Energy`	The nominal beam energy at the respective spot position. Unit is MeV.
`Scan Spot Position Map` [*ScanSpotPos*]	The x- and y-coordinates of the scan spots. They are defined as projected onto the isocentric plane in the IEC Gantry coordinate system. Unit is mm.
`Scan Spot Meterset Weights`	A dataset of meterset weights corresponding to scan spot positions. The order of weights matches the positions in `Scan Spot Position Map`.
`Scanning Spot Size` [*ScanSpotSize*]	The scanning spot size as calculated using the full-width half maximum (FWHM), specified by a numeric pair. The size is measured in air at the isocenter in the IEC Gantry coordinate system. Unit is mm.
`Gantry Angle` [gA]	Gantry angle of radiation source, i.e., orientation of IEC Gantry coordinate system with respect to the fixed reference coordinate system. Unit is degrees.
`Patient Position`	Specifies the orientation of the patient on the treatment table, i.e. if the patient was oriented in a head-first supine position or otherwise. Located in the DICOM CT Image files, and the RT Plan file.

4.3.1 Transformation of the beam direction

By default, a particle beam along with its spatial characteristics, is referred to as a beam going in the positive z-direction in the FLUKA coordinate system [83]. As mentioned, the DICOM coordinate standard axes directions were chosen to be used directly in FLUKA, meaning that a beam going in the z-direction will, in most cases, not be correct. A patient located on a treatment table receiving radiation therapy will be irradiated by a beam in the xy-plane according to the DICOM coordinate system, at least for treatments applied using a gantry. To simulate a rotating gantry in FLUKA, the position of the radiation source must be transformed according to the angle of the gantry as explained in the next subsection. It is therefore also necessary to transform the beam direction in FLUKA

depending on where the source is located in relation to the patient. This can be done using the FLUKA BEAMPOS card or directly in the FLUKA `SOURCE` routine. The two parameters in the `SOURCE` routine that must be changed are the so-called TXFLK and TYFLK, where the former is the direction cosine of the beam with respect to the x-axis in the FLUKA coordinate system, and the latter is the direction cosine of the beam with respect to the y-axis in the same coordinate system. By utilizing simple trigonometry, the direction cosines can be calculated using the equations (4.3) below:

$$\begin{aligned} TXFLK &= \cos(\mathit{flkAng}) \ , \\ TYFLK &= \cos(gA) \ , \end{aligned} \tag{4.3}$$

where the gantry angle (gA) can span from $0° - 360°$. *fklAng* is a variable angle defined in the script in order to make the transformations perform correctly. It is defined as:

$$\mathit{flkAng} = \begin{cases} gA + 90°, & \text{if} \quad 270° < gA \leq 360° \text{ or } 0° \leq gA \leq 90° \\ 270° - gA, & \text{if} \quad 90° < gA \leq 270° \end{cases} . \tag{4.4}$$

Figure 4.3 shows an example of a beam direction transformation. It displays the transformation of a beam source located at a gantry angle of zero degrees in the FLUKA coordinate system. Without transforming the direction, the beam will travel along the positive z-axis. By utilizing the formulas 4.3 the beam will be defined as having a cosine equal to zero relative to the x-axis and a cosine of 1 relative to the y-axis, i.e. the beam direction becomes perpendicular to the x-axis and parallel to the y-axis. This coincides with a gantry angle of zero degrees in the FLUKA coordinate system (see also Figure 4.2). Another example is a gantry angle of 180 degrees, TXFLK is still 0, TYFLK is then equal to -1, and the beam direction will become anti-parallel to the y-axis.

4.3.2 Transformation of the spot positions and spot sizes

All spot positions and sizes in DICOM files are defined in millimeters and must be converted to centimeters. In addition, further trigonometric transformations must be performed because the axes of the FLUKA- and the gantry coordinate system do not correspond. Moreover, as the gantry coordinate system rotates with the gantry angle, the coordinates defined in this system will always be the same, independent of the gantry angle. The FLUKA coordinate system is however fixed; therefore, the coordinates of the spot positions and the direction of the size extension of the spot sizes must be transformed according to the gantry angle.

Scan spot positions

Transforming the y-coordinates of the scan spot positions is straightforward, as the only difference in this relation is that the y-coordinates in the gantry system will be equal to z-coordinates in the FLUKA system. This is true for every gantry

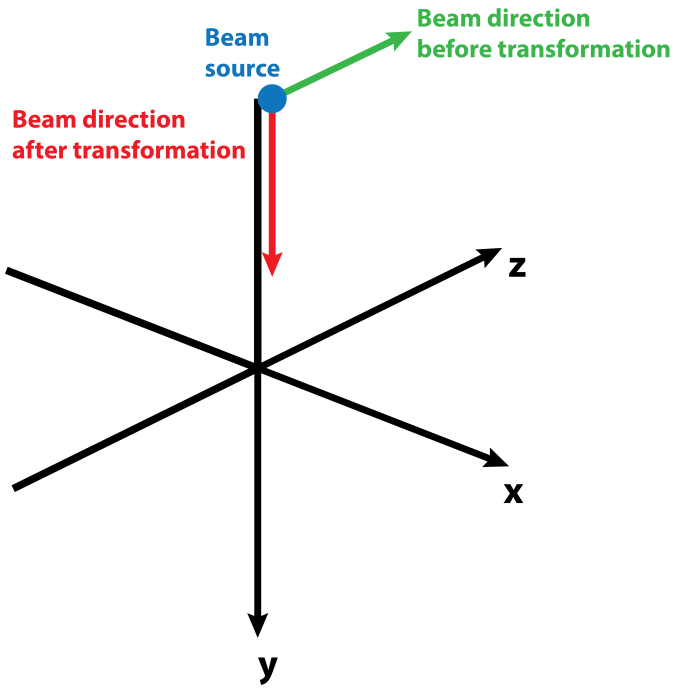

Figure 4.3: Transforming the initial FLUKA beam from going in the z-direction to travel along the positive y-axis.

angle, as the FLUKA z-axis will always be oriented in the same direction as the gantry y-direction.

The x-position in the gantry coordinate system must be distributed in the xy-plane in the FLUKA system depending on the gantry angle, i.e. depending on where the radiation source is located in relation to the patient. Therefore, one spot coordinate in the xy-plane in the FLUKA system is created from the single x-position in the gantry system. In addition, the distance from the source to the isocenter must be added to the spot position in the xy-plane. The following trigonometric equations define the spot positions in the FLUKA coordinate system:

$$\begin{aligned} SpotPosX &= \frac{ScanSpotPos[0]}{10} \times \cos(gA) + r \times \sin(gA) \ , \\ SpotPosY &= \frac{ScanSpotPos[0]}{10} \times \sin(gA) - r \times \cos(gA) \ , \\ SpotPosZ &= \frac{ScanSpotPos[1]}{10} \ . \end{aligned} \tag{4.5}$$

The $SpotPosX$, $SpotPosY$, and $SpotPosZ$ are the spot coordinates in the FLUKA coordinate system, the $ScanSpotPos[0]$ and $ScanSpotPos[1]$ are the x- and y-coordinates, respectively, as defined in the gantry coordinate system, and r is the distance from the radiation source to the isocenter, which is added to $SpotPosX$ and $SpotPosY$ depending on the gantry angle.

Scanning spot sizes

The transformation of the spot sizes (FWHM) is quite similar. The spot size in the y-direction in the gantry coordinate system can, by the same reasoning as above, be directly transformed to the z-direction of the FLUKA system. The spot size in the x-direction must be distributed in the FLUKA xy-plane, again by the same argument as above. The following transformations can be performed:

$$\begin{aligned} FWHM_x &= \left| \frac{ScanSpotSize[0]}{10} \times \cos(gA) \right| , \\ FWHM_y &= \left| \frac{ScanSpotSize[0]}{10} \times \sin(gA) \right| , \\ FWHM_z &= \frac{ScanSpotSize[1]}{10} . \end{aligned} \tag{4.6}$$

The $FWHM_{x,y,z}$ are the spot sizes in the FLUKA coordinate system, the $ScanSpotSize[0]$ and $ScanSpotSize[1]$ are the spot sizes in the x- and y-directions, respectively, as defined in the gantry coordinate system.

To simulate an extended spot size in FLUKA, for each sampling of a particle, the initial spot position for the particle is read. Added to this spot position is the FWHM divided by a factor $2\sqrt{2\ln 2}$ to obtain the standard deviation. This standard deviation is further multiplied by a FLUKA defined Gaussian distribution. As a consequence, when a particle is sampled, its position will be Gaussian distributed around the spot position, thereby mimicking an extended spot size. See equation (4.7) for a mathematical explanation:

$$XFLK(NPFLKA) = SpotPosX + \frac{FWHM_x}{2\sqrt{2\ln 2}} \times RGAUSS . \tag{4.7}$$

The $XFLK(NPFLKA)$ is the FLUKA simulated spot position for each sampling of a certain particle $NPFLKA$ and $RGAUSS$ is a random Gaussian distribution. The same formula is applied for the y- and z-positions as well.

4.4 Displaying the Dose Distribution

In order to properly compare the calculated dose distributions from the TPS and FLUKA, displaying the distributions using the same method and software was necessary. Three python scripts called `tpsScore.py` displaying the TPS dose distribution, `flukaScore.py` displaying the FLUKA recalculation of the dose distribution, and `compFLKTPS.py` displaying the difference of the dose calculated by the TPS and FLUKA, were developed. The purpose of these scripts was to plot the dose distribution as a 2D color wash transposed over the CT images, in addition to plotting the delineated volumes of interest on the images. Scripts for plotting lateral- and longitudinal dose curves were also created. The Matplotlib library was selected for the task of displaying the doses. The dose distribution is displayed using three different main plotting functions, one for the CT image,

one for the dose distribution, and one for the delineated structures. As all three scripts follow the same principles explained below, there will not be a separate section for each script. However, a subsection prevails in the end, outlining the main differences.

4.4.1 CT images

The CT HU information is located in the already mentioned two-dimensional pixel_array. These CT units are plotted using a pre-defined grayscale color scheme from Matplotlib. The CT grid makes up the basis for the dose display plot, meaning that the plot of the dose and the structures must follow the same grid and extension as the CT image. The following equations define the minimum and maximum values for the axes:

$$\begin{aligned} CtX_{min} &= \frac{ImagePos[0] - PixSpace[0]/2}{10} \,, \\ CtY_{min} &= \frac{ImagePos[1] - PixSpace[1]/2}{10} \,, \\ CtX_{max} &= CtX_{min} + \frac{CtColumns \times PixSpace[0]}{10} \,, \\ CtY_{max} &= CtY_{min} + \frac{CtRows \times PixSpace[1]}{10} \,. \end{aligned} \tag{4.8}$$

CtColumns and *CtRows* are defined as the number of columns and rows in the x- and y-direction of the CT image, respectively. This information can be found in the DICOM CT Image. Subtraction of half the pixel value is necessary because the *ImagePos* refers to the position in the middle of the pixel, and thus when defining the minimum values for the axes, the minimum value must be defined at the pixel corner. Division by 10 is done in order to obtain answers in centimeters.

4.4.2 Dose distribution

In order to reduce the amount of binning information for the treatment simulation in a TPS, the dose distribution is typically scored on a grid with larger dimensions than the CT image. It is therefore necessary to interpolate the dose grid equal to the size of the CT grid and remap the dose distribution to the correct position. All parameters needed to perform the interpolation are contained in Table 4.2. By defining maximum- and minimum values in the x- and y-direction for the dose grid, it will be forced to follow these definitions. The following formulas is used:

$$
\begin{aligned}
DoseX_{min} &= \frac{DoseImagePos[0] - DosePixSpace[0]/2}{10} \,, \\
DoseY_{min} &= \frac{DoseImagePos[1] - DosePixSpace[1]/2}{10} \,, \\
DoseX_{max} &= DoseX_{min} + \frac{DoseColumns \times DosePixSpace[0]}{10} \,, \\
DoseY_{max} &= DoseY_{min} + \frac{DoseRows \times DosePixSpace[1]}{10} \,.
\end{aligned}
\tag{4.9}
$$

The parameters used in the equations are exactly the same as for equations (4.8), except that they refer to the dose image and not the CT image. Division by 10 is done in order to obtain answers in centimeters.

The dose distribution must additionally be interpolated in the z-direction. The script, therefore, evaluates the fractional distances from the two slices in the dose distribution that are closest to the CT slice that is being plotted. From these two slices of dose, a single dose distribution can be created by multiplying each of these slices with its respective fractional distance.

As treatment planning systems remove doses located outside the patient, it is desirable to do the same for the FLUKA calculated dose, making visual comparisons simpler. Therefore, the script obtains the coordinates of the external region of interest (the patient outline). It further evaluates if the calculated dose is located outside or inside the patient. If parts of the dose are outside the patient, the dose at these locations will be set to zero.

Normalizing the dose distributions

In order to compare dose distributions between FLUKA and the TPS, the distributions must be normalized. Not all TPSs used in this project provided the number of particles used for treatment. This raised a problem to perform proper normalizations. FLUKA calculates the dose per primary particle, and if the number of particles used in the TPS dose calculation is available, the number can be multiplied by the FLUKA dose to obtain the total calculated dose compared to the TPS. If the number of particles was not provided, it was chosen to perform geometrical normalization [31]. The dose in both the TPS and FLUKA is then normalized to the average dose of the 1000 closest voxels surrounding the center position (the isocenter) of the target volume. The normalization is based on the assumption that in this region the differences between the FLUKA dose and the TPS dose are minor. This yielded acceptable results for the purpose of this project, but normalizing using the number of treatment particles should be done in order to perform proper comparisons.

4.4.3 Delineated structures

It is highly desirable to be able to display delineated regions of interest (ROI) in the patient due to the fact that visual evaluation of the dose received by the target volume(s) and OARs thereby becomes clearer. Parameters needed for plotting

structures are given in Table 4.4, which are all located in the DICOM RT Structure file.

Table 4.4: Coordinate- and color information of delineated structures (ROI), needed for plotting.

Tag name	Tag description
`Contour Sequence`	Sequence of the contours defining ROIs. The array consists of ROI coordinates in the following format $[x_1, y_1, z_1, x_2, y_2, z_2, \ldots, x_n, y_n, z_n]$.
`ROI Display Color`	RGB triplet color representation for ROIs, specified using the range $0-255$.

The user performing the plotting is provided with a list of the available structures, and can choose which ones to be shown on the CT image. The script loops over all the coordinates, plots each point and further draws a line between the plotted points. This line is drawn using the same color as defined for the respective ROI.

4.4.4 Plotting the FLUKA dose distribution and the dose difference

Plotting the dose distribution calculated by FLUKA, uses practically the same method as used for plotting the TPS dose distribution. The main difference is that FLUKA scores the dose utilizing a Fortran matrix, which is formatted differently compared to the three-dimensional NumPy array used by the DICOM files. The conversion is, however, relatively straightforward.

Plotting the dose distribution is performed by importing both the dose distributions from the TPS and FLUKA into the script. By subtracting the TPS dose distribution from the FLUKA dose distribution, the residual dose can be transposed on the CT images, yielding positive values where FLUKA has calculated higher doses, and negative values for higher doses calculated by the TPS. For the geometrical normalization, the unit for the dose difference [%], is expressed as a percentage of the average dose to the PTV, i.e. the normalization dose. For normalization by using the number of treatment particles, the unit for the dose difference is the respective dose unit used (Gy or Gy(RBE)).

4.5 FLUKA Dose to DICOM File and Dose Volume Histograms

By converting the dose from the FLUKA Fortran matrix to the same format as the DICOM dose pixel_array, it is possible to further create a separate DICOM RT Dose file containing the FLUKA recalculated dose. This DICOM file is very versatile as the file can be imported into numerous types of software that are able to read and handle DICOM files. For example, by importing the FLUKA

recalculation into the same TPS as the dose was initially calculated by, the TPS's powerful tools for dose evaluation, creation of dose volume histograms and dose comparisons, can be exploited.

The Pydicom library has the ability to change the data elements associated with each DICOM tag. This means that by writing a few lines of code, the pixel_array containing the originally TPS calculated dose distribution can be exchanged with the FLUKA recalculated dose distribution and saved as a new DICOM file. To make the FLUKA DICOM RT Dose file consistent with the regular TPS dose DICOM files, the doses outside the patient are removed. By creating DICOM files of the FLUKA dose, voxel-by-voxel comparisons to the original dose distribution can also be performed, and fine grid dose differentials can be obtained.

In this project, the RayStation treatment planning system was used for creating dose volume histograms (DVH). The RT Dose files from FLUKA and the TPS, along with the RT Structure file were imported into RayStation which performed the DVH calculations. The TPS created a .dvh file (regular ASCII file) containing volume- and dose values. This .dvh file was exported and further imported into a developed script that read the file and plotted the DVHs.

4.6 Creation of Water Phantom DICOMs

In order to test the developed tool on simple radiation plans, DICOM CT images for three separate water phantoms were designed. The phantoms were created using Dicomutilis [94], a set of utilities for working with DICOM files. They were defined as having pixel sizes of 1 mm and a slice thickness of 2 mm, resulting in 150 CT slices containing images of 300×300 pixels for each phantom.

A $30 \times 30 \times 30\,\mathrm{cm}^3$ homogeneous water phantom was defined (all voxels having HU = 0). Further, a $5 \times 5 \times 5\,\mathrm{cm}^3$ box-shaped PTV, also consisting of water, was defined in the middle of the phantom. Rectangular OARs ($2 \times 5 \times 5\,\mathrm{cm}^3$) made of water were placed at distances 0.5, 1 and 2 cm to the right of the PTV, with the idea of a beam coming from the left i.e. going in the positive x-direction. An additional OAR, of the same size, was added along the beam, just outside the location of where the beam was intended to irradiate. The idea of the OARs was to evaluate doses located outside the target volume and in low-dose regions.

The same phantom setup was chosen for the two remaining water phantoms, only in these cases, were inhomogeneities added. For both phantoms a $2.5 \times 2.5 \times 2.5\,\mathrm{cm}^3$ box having a HU unit of 1000 and -1000 to represent bone and air, respectively, were placed between the PTV and the water phantom edge, covering half the entrance area of the beam. See Figure 4.4 for water phantom illustrations, along with the delineated structures.

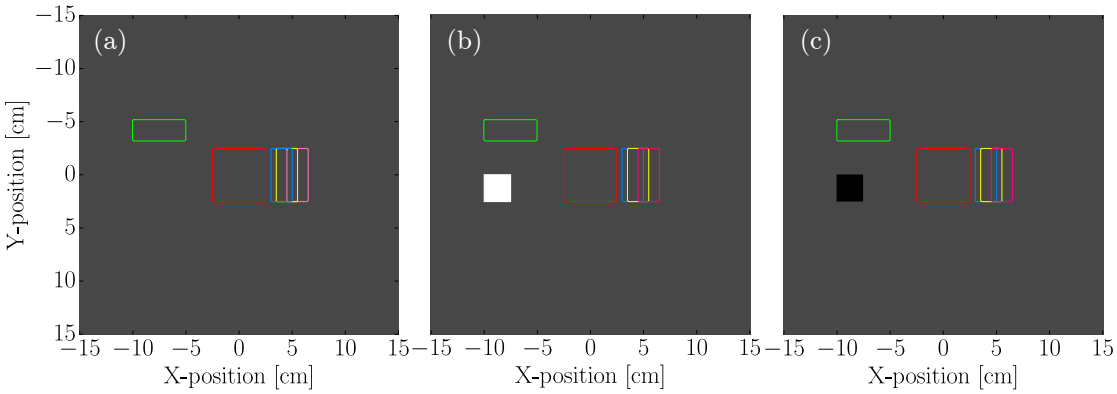

Figure 4.4: The defined water phantoms and delineated structures. (a) shows the homogeneous water phantom, (b) shows the phantom with the bone volume, while (c) is the phantom containing an air cavity. The red box in the middle indicate the PTV, whereas the rectangles are the OARs in blue, yellow, pink and green.

4.7 Handling of Treatment Plans

4.7.1 Water phantom irradiations

All three water phantoms were imported into RayStation (v4.6), by RaySearch Laboratories, for treatment planning. The same treatment plan was applied for all the phantoms. A homogeneous physical dose of 70.00 Gy delivered in 35 fractions was prescribed to the PTV. The radiation dose was delivered using a single 270° beam, i.e. a beam going in the positive x-direction in the phantom coordinate system. Objectives and restrictions given for the optimization process can be seen in Table 4.5. *External* comprise the whole water phantom volume, excluding other delineated structures.

Table 4.5: Plan objectives for the water phantom irradiation plans.

Region of interest	**Objective**	**Weight**
PTV	Min DVH: 70.00 Gy to 100 % volume	1.0
PTV	Max dose: 71.75 Gy	2.0
External	Max DVH: 35.00 Gy to 5 % volume	1.0
External	Max dose: 56.00 Gy	3.0
OAR_0.5cm	Max DVH: 7.00 Gy to 30 %	0.5
OAR_0.5cm	Max DVH: 21.00 Gy to 10 %	0.5

It should be noted that the created water phantom plans are not necessarily clinically optimized, but the treatment plans did, however, yield acceptable results to be used for the purpose of recalculating the plans in FLUKA.

The physical dose was scored over the whole water phantom where the scoring grid was defined to have pixel sizes of $2 \times 2\,\mathrm{mm}^2$ as well as a slice thickness of 2 mm.

4.7.2 Cranio-spinal irradiation

Cranio-spinal irradiation (CSI) is one of the most technically challenging treatment planning and delivery procedures due to the complex-shaped and large target volume [25]. CSI is a radiation treatment for cancer in the central nervous system, where the whole spine and brain are irradiated. $20 - 30\,\%$ of all cancer diseases in pediatric patients are due to central nervous system malignancies where a large fraction of this is medulloblastoma. Because the target volumes are close to a number of critical organs, side effects may occur following treatment, and it has been found that there is significant increase in risk of developing secondary cancer after medulloblastoma treatment [95]. For this reason, an IMPT CSI plan was chosen for Monte Carlo recalculations.

The proton plan was provided by C. Stokkevåg [25]. The plan was calculated in SIEMENS Syngo RT Planning TPS at the National Centre of Oncological Hadrontherapy (CNAO). A large advantage of using Syngo as opposed to RayStation in this project, was that the number of particles used for each treatment field was available, thereby making the normalization of the dose in FLUKA straightforward. The patient, an 11-year-old boy, was administered a physical dose of 21.27 Gy (biological effective dose of 23.40 Gy(RBE)) in 13 fractions to the PTVs. Three fields were applied in a straight angle to the spine, and an additional two opposing cranial treatment fields were delivered to the patient's brain at angles of 15° relative to the treatment table. The patient was located on the treatment table in a head first - prone position, and the treatment table was rotated in order to treat the patient from the desirable angles. Objectives given for the optimization process can be seen in Table 4.6. The number of particles administered for each beam is given in Table 4.7. Cran1 and Cran2 are the cranial fields while Spin1, Spin2 and Spin3 are the treatment fields applied to the spine.

Range shifters and range modulators were also used in the treatment plan (CNAO beam line specifics) having water equivalent thicknesses of 31.44 mm and 2.00 mm, respectively. As this was the only information available concerning the CNAO beam line, the range shifters had to be modeled in FLUKA as slabs of water.

Table 4.6: Plan objectives for the CSI plan.

Region of interest	**Objective**	**Weight**
Brain (PTV)	Prescription dose: 23.40 Gy(RBE)	1.0
Spine (PTV)	Prescription dose: 23.40 Gy(RBE)	1.0
Esophagus (OAR)	Max dose: 10.00 Gy(RBE)	1.0
Thyroid (OAR)	Max dose: 5.00 Gy(RBE)	1.0
Eyes (OAR)	Max dose: 5.00 Gy(RBE)	1.0
Trachea (OAR)	Max dose: 5.00 Gy(RBE)	1.0

Table 4.7: Number of primary protons for the CSI plan.

Treatment field	Number of particles
Cran1	1.295×10^{11}
Cran2	1.292×10^{11}
Spin1	5.756×10^{10}
Spin2	6.188×10^{10}
Spin3	7.499×10^{10}

4.8 FLUKA Simulation Setup

All simulations in this thesis was conducted with FLUKA (v.2011.2c.4). The conversion from Hounsfield units to density and material composition already implemented in FLUKA was used. The conversion in the HU range between -1024 to 1600 is based on the work of Schneider *et al.* [81] as a result of an analysis of 71 human tissues. The conversion curve has been further extended by Parodi *et al.* [82] for the HU range between 1600 and 3070. The final result is 27 groups of different materials; 1 group for air, 1 group for lung tissue, 7 groups for soft tissue, 15 groups for skeletal tissues and 3 groups of high-Z materials. Within each group, the material composition is preserved, while the material density scales with the HUs. The calibration curve from HU to material density used in the simulations is shown in Figure 4.5.

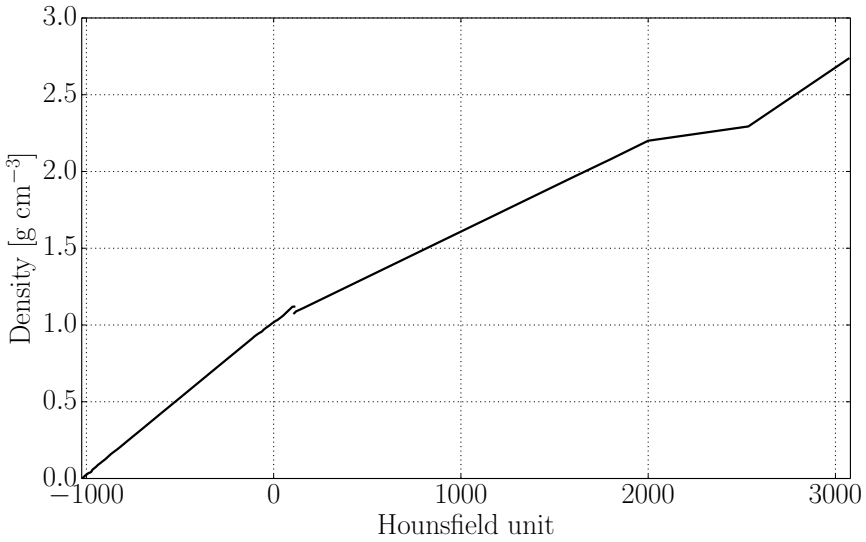

Figure 4.5: The calibration curve for HU to material density used in the simulations.

For the phantoms, the stopping power in water in FLUKA was scaled to obtain correspondence with RayStation. In order to achieve unbiased comparisons between the two systems, stopping powers should be matched [38]. A FLUKA CORRFACT card was added which has the ability to scale the stopping power density for selected materials. A scaling factor of 1.005 was set for the water phantoms. The value was based on test simulations and further comparisons between

the depth dose curves for FLUKA and RayStation. For the CSI plan, no attempt was made to calibrate FLUKA and the TPSs as this was beyond the scope of this project. To achieve good accuracy, the stopping powers would have had to be matched for all materials defined in the simulation [35]. This would have become problematic, especially considering that the TPS the plan was calculated in was not available for the author. However, it was not necessary to match the stopping powers in order to test the developed scripts.

Most of the relevant FLUKA input cards were added automatically by the scripts as previously explained. The energy spread had to, however, be defined manually, as this is a treatment machine specific parameter [96] that is not located in any DICOM file. As this value was not available for any of the treatment plans, the FWHM of the energy spread was set to 0.8 % of the respective beam energy for all FLUKA simulations. The choice of this value was based on trial and error FLUKA simulations on a homogeneous water phantom initially calculated in RayStation. An energy spread of 0.8 % yielded an adequately similar SOBP for the two systems. The value was also somewhat in agreement with Hsi *et al.* [97], who have reported an energy spread for cyclotrons (after passive range modulation) between 0.8 % and 7 %, depending on the beam energy and modulating material. This does, however, not necessarily mean that the value was correct, especially not for the Syngo simulations.

The water phantom treatment plans were all simulated using 10 million particles per CPU thread, using 4 threads per beam over 5 cycles. This yielded mean statistical errors below 1 % for the PTV, and below 10 % in low-dose regions. For the CSI plan, each separate field was simulated using 10 million particles per CPU thread, using 2 threads per beam over 1 cycle. The mean statistical errors were below 2 % for the PTVs and below 10 % in regions with lower dose. However, for regions with very little dose, the errors increased rapidly.

Scoring

Treatment planning systems calculate the water-equivalent dose, or dose-to-water, D_w. This is because traditional treatment planning systems model the human body as water with varying mass density, electron density or stopping power [98]. Arguments for reporting dose-to-water are that a human mostly consists of water (about 60 % [99]), all clinical experience is based on dose-to-water, and commissioning, quality assurance and absolute dose measurements are done in water. On the other hand, Monte Carlo tools originally calculate the dose to material, D_m, as they take into account material properties such as ionization potentials and material compositions.

Therefore, it was desirable to calculate the dose-to-water in FLUKA for comparison purposes. This can be achieved by using the FLUKA user routine `FLUSCW.f`, a routine used for weighting e.g. particle fluences. Dose-to-water can be calculated by scoring the fluence of the charged particles in a given medium. By multiplying the fluence by the LET in water for the charged particles, the dose-to-water can

be obtained. See equation (4.10).

$$D_w = \Phi_m \times \frac{LET_w}{\rho_w} \ , \tag{4.10}$$

where D_w is the dose-to-water, Φ_m is the fluence of the charged particles in the given medium, ρ_w is the density of water and LET_w is the linear energy transfer in water.

In FLUKA, the fluence of all charged particles was scored over the same region as the TPS, using a USRBIN card. The fluence was further multiplied by the LET_w using the `FLUSCW.f` user routine, thereby obtaining the dose-to-water.

Comparing dose-to-water and dose-to-medium

Dose-to-water and dose-to-medium report different magnitudes of doses as the energy loss of particles depends on the elemental composition of the medium [35]. To study the difference between the two, a second scoring card was added to the FLUKA simulation for the CSI plan that scored dose-to-medium. It was scored using a regular dose USRBIN card in FLUKA, over the same region as the dose-to-water was scored. The D_w results were converted to a FLUKA DICOM RT Dose file and run through the script `compFLKTPS.py` along with the FLUKA scoring matrix of the D_m.

To further evaluate the difference between the two scoring methods, a $30 \times 30 \times 30\,\mathrm{cm}^3$ phantom consisting purely of voxels with a HU unit of 1000 to emulate high-density bone, was created using Dicomutilis. A SOBP covering a $5 \times 5 \times 5\,\mathrm{cm}^3$ PTV in the middle of the phantom was defined. The plan was simulated in FLUKA, scoring both dose-to-water and dose-to-medium.

Chapter 5

Results

5.1 Dose Verification and Recalculations

The main result of this work is the developed Python based tool. The results presented in this chapter demonstrates its ability to recalculate doses from simple treatment plans as well as complex clinical multi-field plans. The TPS radiation plans from the previous chapter (water phantom irradiations and CSI) were run through the Python scripts and FLUKA Monte Carlo recalculations were conducted. The main focus of the results in this chapter will be to demonstrate the functionality of the developed tool. The results will not focus on differences between the TPS and FLUKA calculated doses i.e. perform benchmarking of the TPS, as this is beyond the scope of this project. However, aspects that are important to consider when performing validation of TPS calculated doses, will be emphasized.

In this section, two-dimensional dose distributions, dose profiles in the longitudinal and lateral directions, in addition to dose volume histograms, are shown. All results marked D_{TPS} are doses directly reported from the respective treatment planning system, while all results tagged D_{MC} are FLUKA Monte Carlo recalculations of the doses. Results showing $D_{MC} - D_{TPS}$ are plots where the TPS calculated dose has been subtracted from the FLUKA calculated dose, in order to better depict any differences. All plots are created using scripts developed in this project, if not stated otherwise.

5.1.1 Water phantom irradiations

For the three water phantoms, all displays of the two-dimensional dose distributions and dose differences in Figure 5.1, shows the slice located in the middle of the phantoms ($z = -0.1\,\text{cm}$). The same slice is also shown for the longitudinal depth dose curves. Further, the lateral dose curves at $x = -0.1\,\text{cm}$ are plotted.

For the two-dimensional dose distributions, including the dose difference plots, the distributions are normalized to the average dose in the middle of the PTV (red box) on the assumption that the doses reported by FLUKA and RayStation are highly similar in this region. The lowest doses displayed, for all 2D-plots, are set to 0.1 % of the PTV dose. The red parts of the dose difference plots are areas where FLUKA calculates a higher dose, while the blue parts depict higher doses from RayStation. All lateral- and longitudinal dose curves are normalized to the maximum dose calculated by RayStation at the respective x- or z-position.

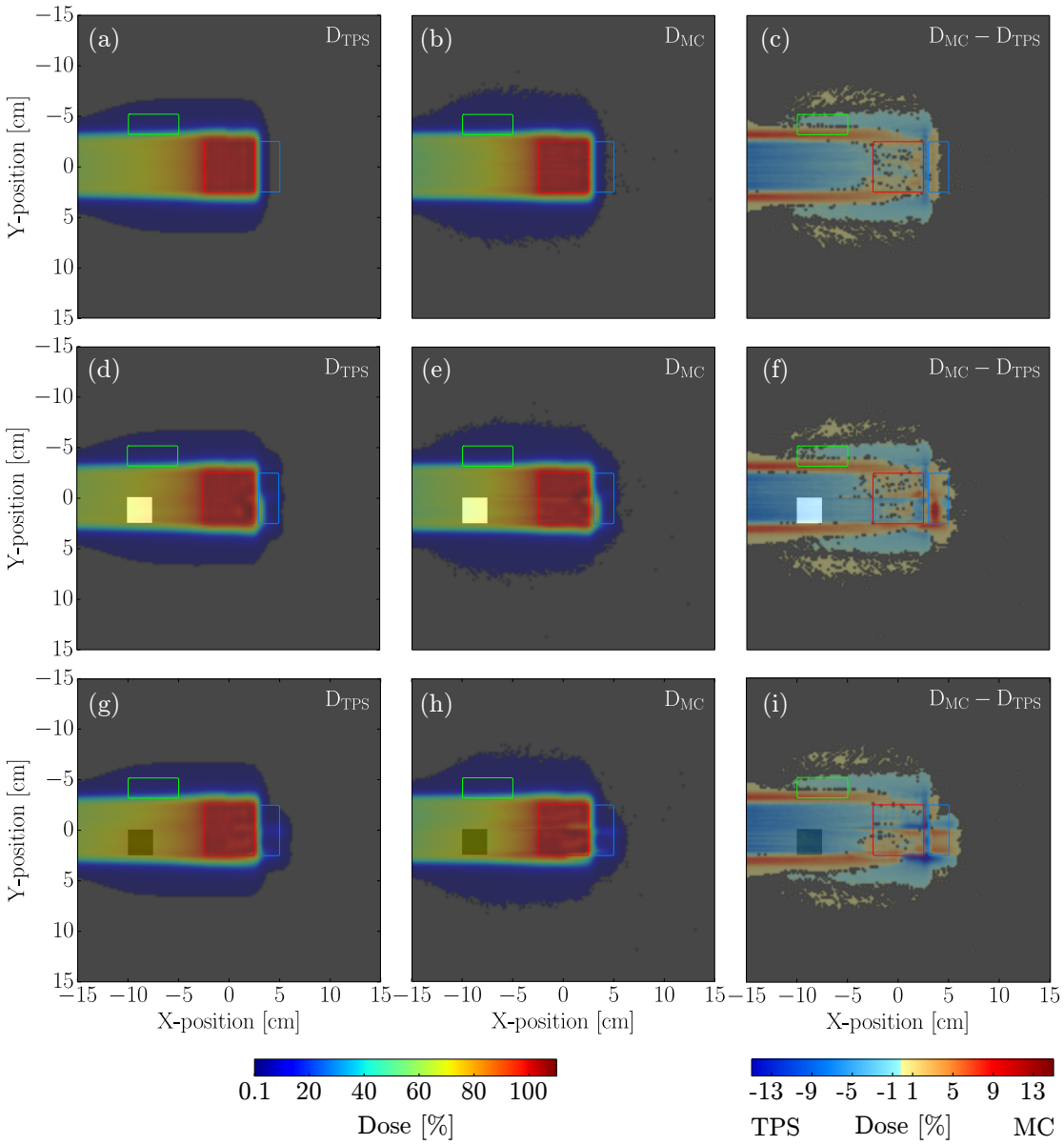

Figure 5.1: Two-dimensional dose distributions on water phantoms. First row is the homogeneous water phantom, second row is the phantom with a bone region, while the third row shows the phantom with an air cavity. The red box is the PTV, the green box is a defined OAR while the blue rectangle is an OAR located 0.5 cm behind the PTV. For (c), (f) and (i), dose differences between -0.1 and 0.1 % are set transparent, depicted as gray dots.

Homogeneous phantom

Figure 5.1a and 5.1b display the two-dimensional dose distributions in the homogeneous water phantom, as calculated by RayStation and FLUKA. From the figures, it is apparent that FLUKA calculates a marginally higher dose in the low-dose regions at the outer parts of the dose distribution. The differences between the

two dose distributions are better depicted in Figure 5.1c. There are some small inconsistencies between the dose calculated by FLUKA and RayStation behind the PTV. Immediately following the PTV, RayStation reports a higher dose, while FLUKA reports a higher dose just inside the blue OAR. This may be due to an incorrect matching of the stopping powers (see section 4.8), and the geometrical normalization (section 4.4) could also cause some discrepancies. RayStation also calculates a higher dose in the middle of the entrance region of the beam, while FLUKA calculates a higher dose at the outer regions.

In Figure 5.2, the longitudinal- and lateral dose curves are shown. Also from the longitudinal curves, it can be seen that RayStation calculates an overall higher dose in the entrance region. The curve at the SOBP region is also smoother for FLUKA, which may be due to an incorrect energy spread in FLUKA. The longitudinal curves further depict a better correspondence between the beam ranges compared to the two-dimensional plot. In Figure 5.2b, showing the lateral dose in the middle of the PTV, FLUKA calculates a marginally higher dose, most pronounced in the outer regions.

Finally, Figure 5.3 displays the dose volume histograms for all the ROIs outlined in the water phantom. The OARs closest to the PTV receives a higher dose according to FLUKA, while the OAR at the side of the beam also receives a higher dose in the Monte Carlo simulation. For the PTV, the dose reported by FLUKA is somewhat less homogeneous and a bit higher for a greater part of the volume. The pink OAR located 2 cm behind the PTV is not visible in the plot, since no significant amount of dose is received.

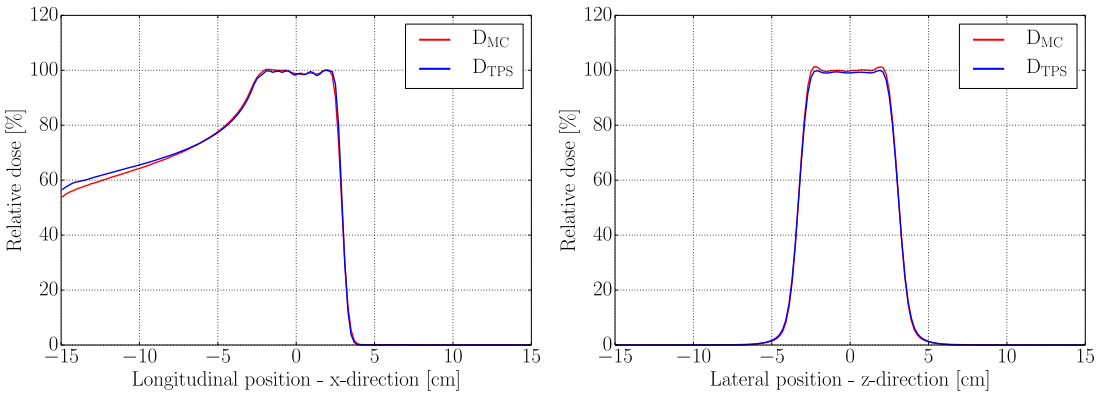

(a) Longitudinal depth dose curves from FLUKA and RayStation.

(b) Lateral dose curves from FLUKA and RayStation.

Figure 5.2: Dose profiles in the longitudinal- and lateral direction from FLUKA and RayStation in the homogeneous water phantom.

Phantom containing a bone volume

When a bone region is introduced to the water phantom, it can be seen from Figure 5.1d and 5.1e that the dose to the PTV becomes less homogeneous for both FLUKA and RayStation. As before, FLUKA calculates a higher dose in the outer regions of the beam. Further, looking at the dose difference in Figure 5.1f,

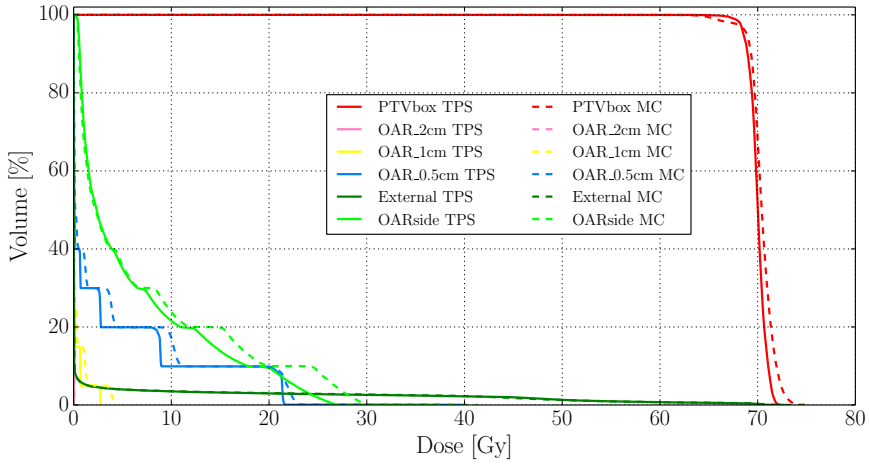

Figure 5.3: Dose volume histograms for ROIs in the homogeneous water phantom.

FLUKA calculates a noticeably higher dose inside the blue OAR, in areas where the beam has penetrated the bone volume. In the upper region of the same OAR, FLUKA still calculates a higher dose than RayStation, but of a lower magnitude compared to the rest of the OAR. Inside the PTV, FLUKA typically calculates a lower dose for areas behind the bone volume, while a higher dose is reported at the part of the PTV where the beam has not penetrated the bone volume.

For the longitudinal dose curves in Figure 5.4a, similar doses, except for the entrance region, is apparent. The lateral dose curves (Figure 5.4b) show a larger dose at the outer regions of the radiation field.

The dose volume histograms for ROIs in the phantom are plotted in Figure 5.5. It is evident that a higher dose is received by the PTV according to FLUKA. The overall doses to the OARs located behind the PTV have also increased, in agreement with what the two-dimensional dose distributions show.

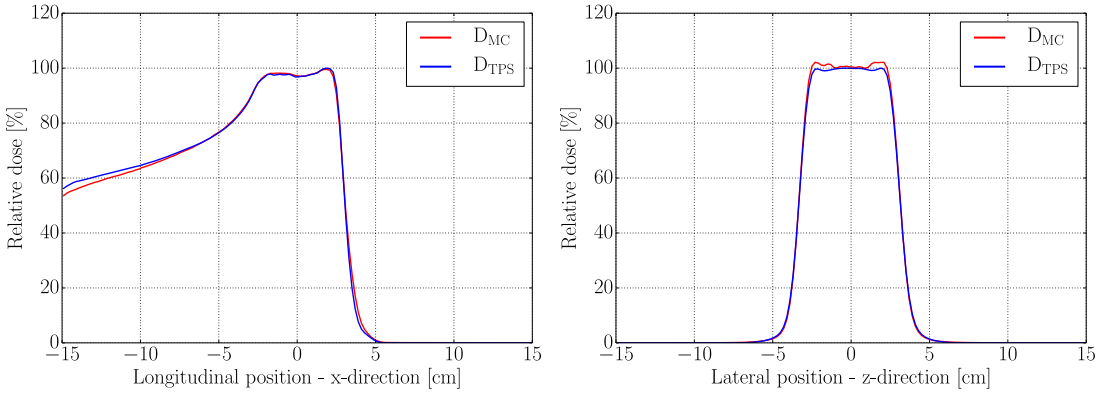

(a) Longitudinal depth dose curves from FLUKA and RayStation.

(b) Lateral dose curves from FLUKA and RayStation.

Figure 5.4: Dose profiles in the longitudinal- and lateral direction from FLUKA and RayStation in the water phantom containing a bone volume.

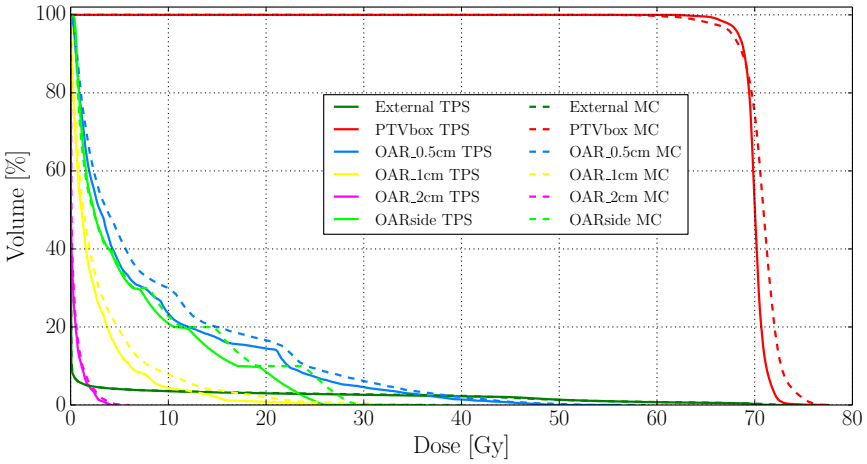

Figure 5.5: Dose volume histograms for ROIs in the water phantom containing a bone volume.

Phantom with an air cavity

In Figure 5.1g-5.1h, the two-dimensional dose distributions, in addition to the relative dose differences between FLUKA and RayStation, are shown. In this setup, the phantom contains an air cavity (HU = -1000) at the same placement as the bone region in the previous case. Even though the beam now has penetrated deeper into the phantom, a lower dose than for the phantom with the bone volume, is reported to the blue OAR. However, FLUKA and RayStation are in relatively good agreement for the doses inside the OAR. This can be observed from Figure 5.1h, due to the absence of any dark blue or dark red spots. No noticeable dose difference to the green OAR compared to the previous cases is reported. In the PTV, FLUKA calculates a higher dose for most locations where the beam has penetrated the air cavity, whereas RayStation reports a higher dose for areas not located behind the air cavity.

Looking at the longitudinal dose profile in Figure 5.6, a lower dose to the distal half of the PTV is calculated by FLUKA. As before, a higher TPS calculated dose is reported at the beam entrance region. The lateral dose curves show a somewhat less homogeneous dose reported by FLUKA, but are however else mostly in agreement with RayStation.

The dose volume histograms in Figure 5.7 show that FLUKA calculates a noticeably less homogeneous dose to the PTV. There is also a discrepancy between the doses received by the OARs according to FLUKA and RayStation.

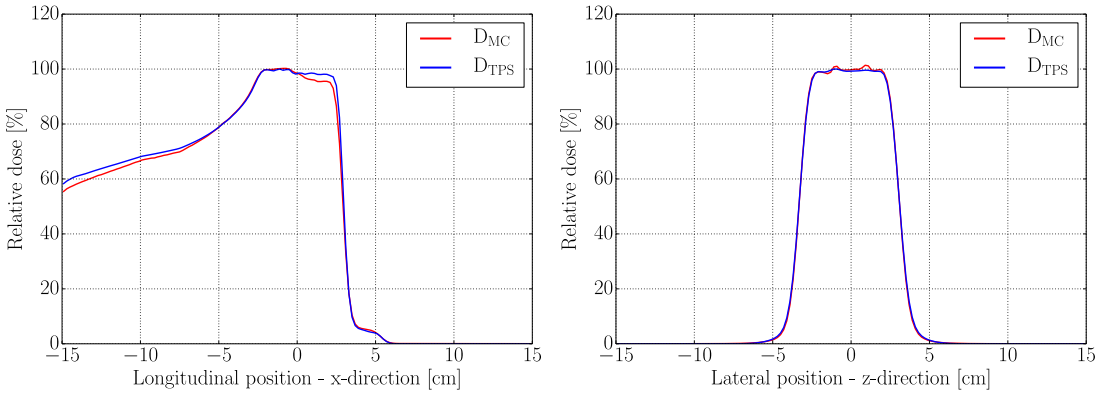

(a) Longitudinal depth dose from FLUKA and RayStation.

(b) Lateral dose curves from FLUKA and RayStation.

Figure 5.6: Dose profiles in the longitudinal- and lateral direction from FLUKA and RayStation in the water phantom containing an air cavity.

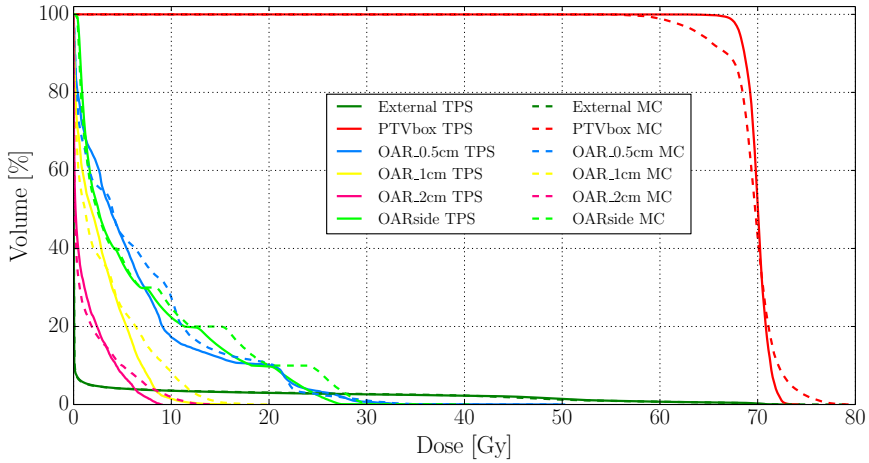

Figure 5.7: Dose volume histograms for ROIs in the water phantom containing an air cavity.

5.1.2 Cranio-spinal irradiation

All doses in the following subsection are biological effective doses, Gy(RBE), i.e. the physical dose, in Gy, multiplied by an RBE of 1.1. The dose distributions (and dose differences) below 0.1 Gy(RBE) are set transparent. For the dose difference plots, the red colored regions depict higher doses calculated by FLUKA, while the blue colored regions mean higher doses reported by the TPS. The one-dimensional dose curves are normalized to the maximum dose calculated by Syngo at the respective y- or z-position.

Shown in Figure 5.8 are dose distributions, and dose differences, from three selected slices of the spine, calculated by Syngo and further recalculated by FLUKA. One slice is plotted from each of the three spinal fields (Spin1, Spin2 and Spin3). FLUKA is able to recalculate the dose distributions, but it is however apparent that the FLUKA dose has a noticeable pullback compared to the TPS dose. This may be due to the lack of beam line implementation in FLUKA, as the pullback is similar for all slices. It becomes even more evident in the dose difference plots, especially for Figure 5.8c. Likewise as for the water phantoms, an overall higher dose is reported by FLUKA at the outer regions. Note that the CT images have been flipped along the x-axis. This was done to obtain correspondence with the RayStation coordinate system (see section 5.3).

Figure 5.9 shows the dose distributions, and dose differences, for the two combined cranial fields, at two separate locations in the head. Comparing Figure 5.9a and 5.9b, the indicated pullback is noticeable, especially in the regions to the upper right and left of the delineated eyes. Apart from this, the dose distributions are quite similar.

In Figure 5.10, the depth dose curves for the spinal fields are plotted. The same slice locations as for the previous figures are shown. The shifted penetration depths of the dose curves are obvious in these figures. The doses are normalized to the maximum dose calculated by Syngo in the respective slice. Except for the shift in the curves, they are in quite good agreement. Figure 5.11 further shows the dose from the cranial fields plotted along the y-direction. FLUKA reports an overall lower dose for both slice locations.

The lateral dose curves from the three spinal fields are shown in Figure 5.12. The curves located at $y = 6.77\,\text{cm}$ are displayed for all three fields. The shapes of the curves are relatively similar, but there are some differences, most prominent in Figure 5.12a. Here, Syngo calculates a dose on the order of 10 % higher than FLUKA at a lateral position of $-18.2\,\text{cm}$.

Figure 5.13 shows dose volume histograms of regions of interest that were prescribed dose goals or restrictions according to the DICOM RT Plan file, in addition to the external ROI, called *SkinOK*. An overall lower dose is calculated by FLUKA for all the delineated volumes. But this is mainly due to the pullback in the FLUKA dose distributions, at least for the OARs, which are located after the Bragg peaks of the beams. Since the beam simulated in Syngo penetrates deeper into the patient, it is expected that the higher doses will be reported to the OARs according to Syngo.

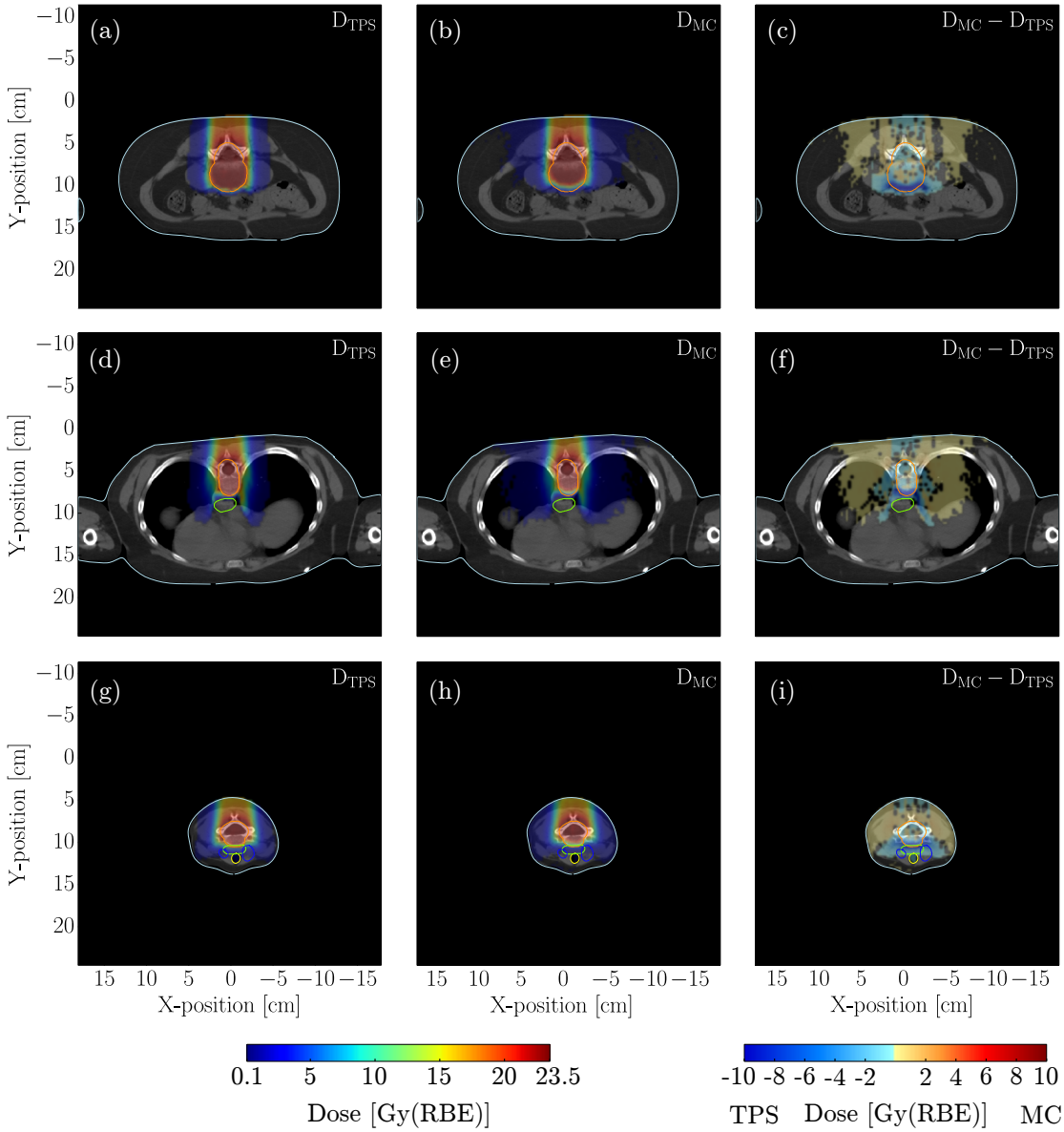

Figure 5.8: Two-dimensional dose distributions of the spinal fields for the CSI plan. Outlined are the spinal PTV (orange), esophagus (green), trachea (yellow) and thyroid (blue). Dose differences between -0.1 and 0.1 Gy(RBE) are set transparent, depicted as black dots.

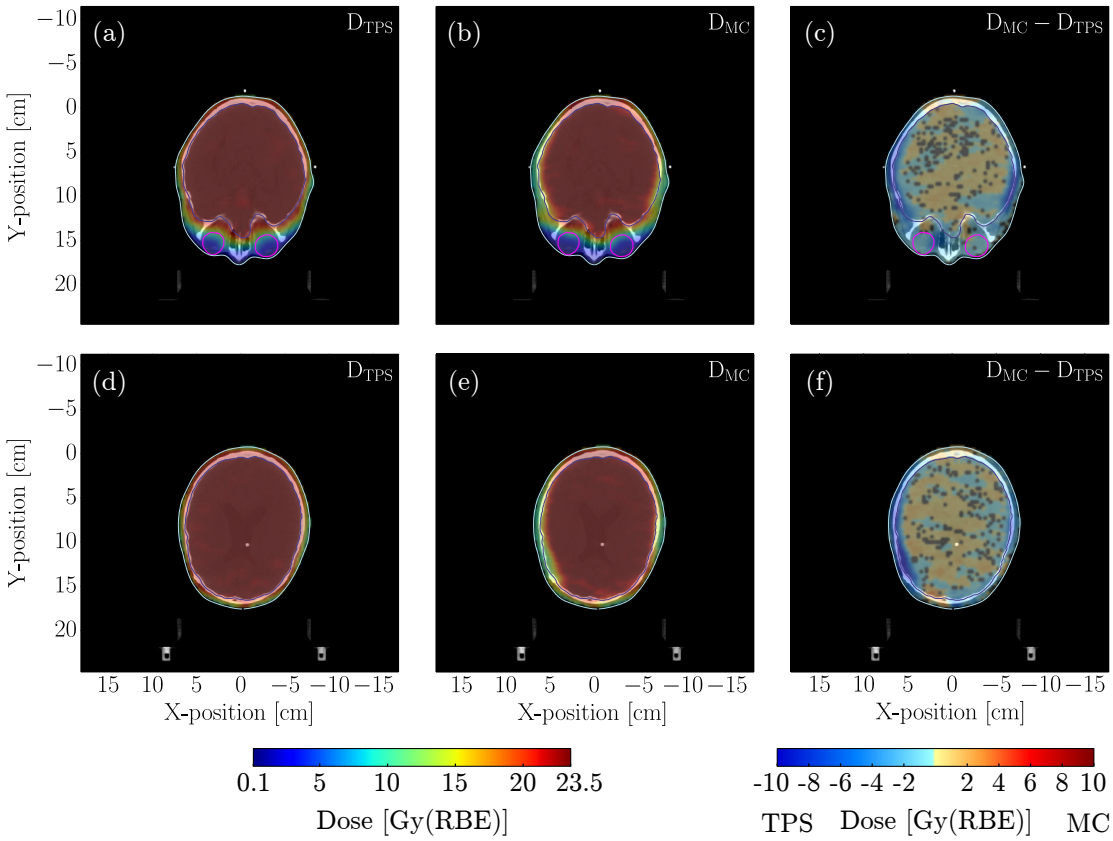

Figure 5.9: Two-dimensional dose distributions of the cranial fields for the CSI plan. Outlined are the brain PTV (purple) and eyes (pink). Dose differences between -0.1 and 0.1 Gy(RBE) are set transparent, depicted as black dots.

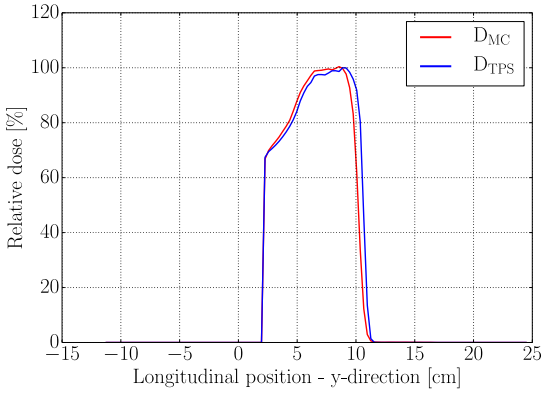

(a) Longitudinal depth dose curves from FLUKA and Syngo at $z = -14.4\,\text{cm}$.

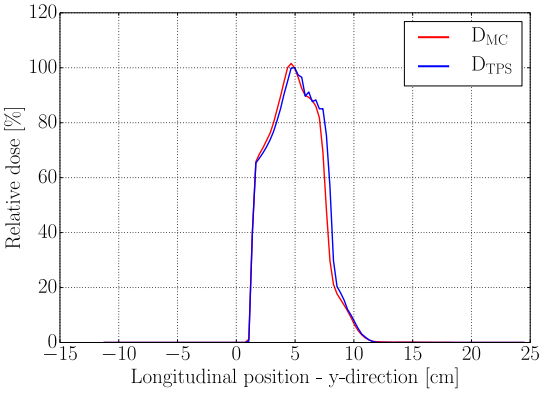

(b) Longitudinal depth dose curves from FLUKA and Syngo at $z = 6.6\,\text{cm}$.

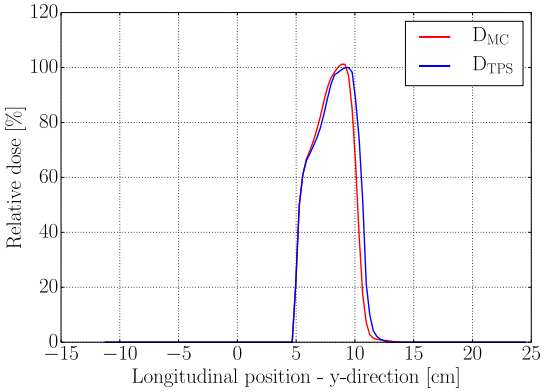

(c) Longitudinal depth dose curves from FLUKA and Syngo at $z = 21.6\,\text{cm}$.

Figure 5.10: Longitudinal depth dose curves of the spinal fields for the CSI plan.

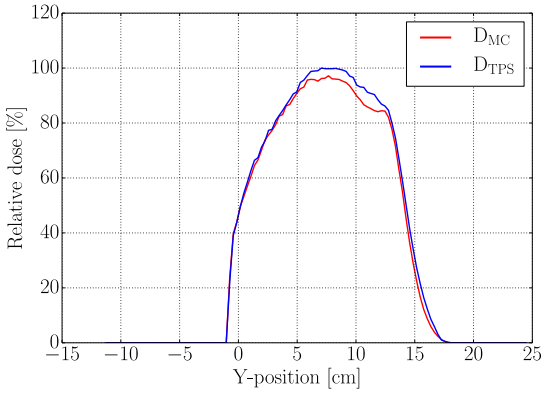

(a) Dose curves from FLUKA and Syngo at $z = 33.6\,\text{cm}$.

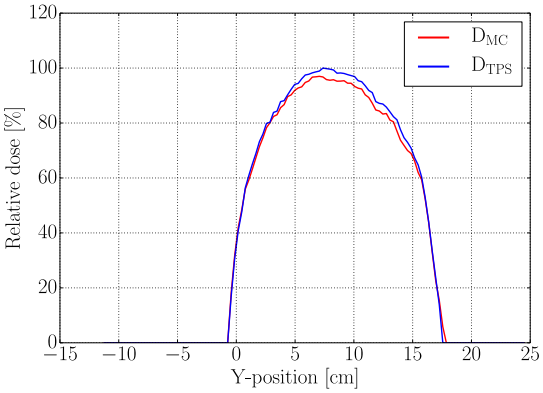

(b) Dose curves from FLUKA and Syngo at $z = 36.6\,\text{cm}$.

Figure 5.11: Dose along the y-axis of the cranial fields for the CSI plan.

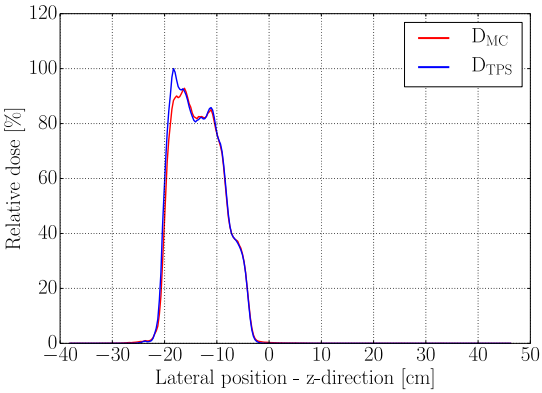

(a) Lateral dose curves from FLUKA and Syngo of the lowest spinal field (Spin3).

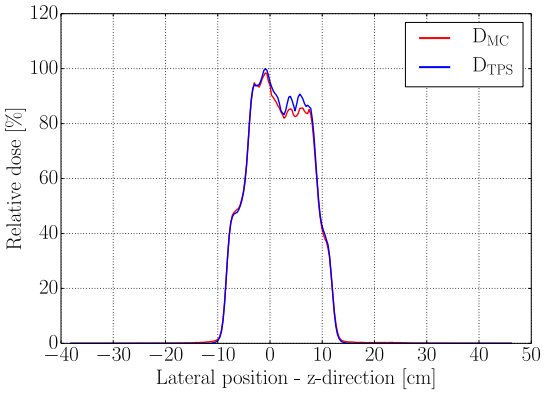

(b) Lateral dose curves from FLUKA and Syngo of the middle spinal field (Spin2).

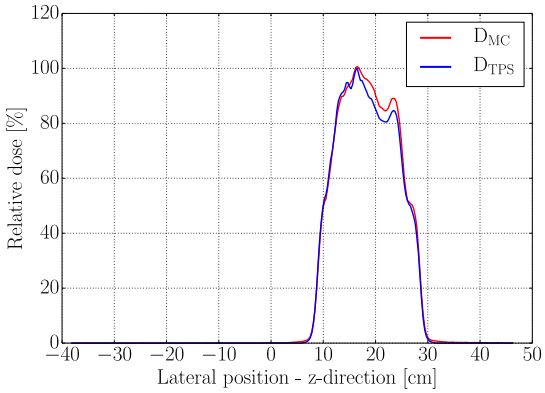

(c) Lateral dose curves from FLUKA and Syngo of the highest spinal field (Spin1).

Figure 5.12: Lateral dose curves of the spinal fields for the CSI plan. Curves at $y = 6.77\,\text{cm}$ are displayed.

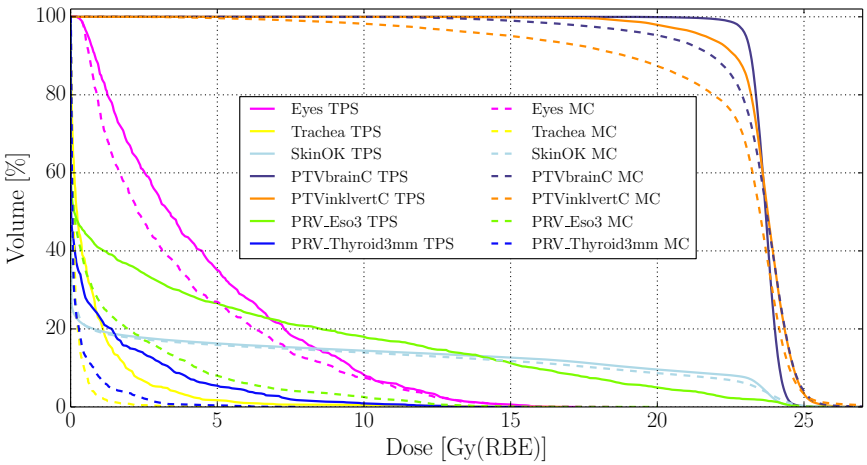

Figure 5.13: Dose volume histograms for ROIs with prescribed dose goals or restrictions for the CSI plan.

5.2 Difference Analysis of Dose-to-Water and Dose-to-Medium

This section presents differences between the scoring of dose-to-water (D_w) and dose-to-medium (D_m). In Figure 5.14a the difference between the two dose-reporting methods on a phantom consisting purely of bone, can been seen. Dose differences below 4 % are set transparent. The dose-to-water is clearly higher for all parts of the dose distribution. The same difference is also evident for the depth dose curves in Figure 5.14b. The D_w is greater than the D_m by approximately 5 % along the whole curve.

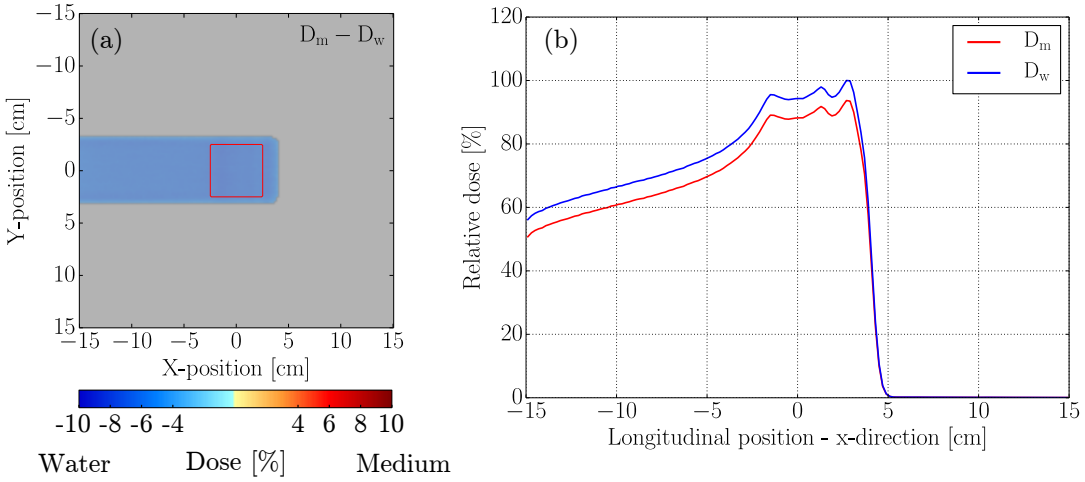

Figure 5.14: Two-dimensional dose difference plot and depth dose curves of dose-to-water and dose-to-medium scored in a bone phantom.

Figure 5.15 shows the difference between the two-dimensional FLUKA dose distributions calculated as D_m and D_w for selected slices in the CSI plan. Dose differences lower than 0.1 Gy(RBE) are set transparent. It looks like the D_w is slightly higher for regions denser than water (HU > 0), while D_m is somewhat greater for low density regions. This can, for example, be seen for some areas in the lungs in Figure 5.15a (delineated in dark blue).

Further, looking at the depth dose curves in Figure 5.16, the dose-to-water is a bit higher for most positions along the curve. Specifically, an increase in the dose-to-water can be seen in Figure 5.16b, starting at a depth around 7.5 cm. Looking at the same position in Figure 5.15b, one can see that the dose-to-water is higher in this region, and this is also at an area where the spine is located. According to H. Paganetti [98], D_w typically reports larger doses to dense material compared to D_m.

Lastly, the dose volume histograms for the two cases are displayed in Figure 5.17. The dose-to-water is slightly greater for the ROIs, at least in the high-dose regions (PTVs).

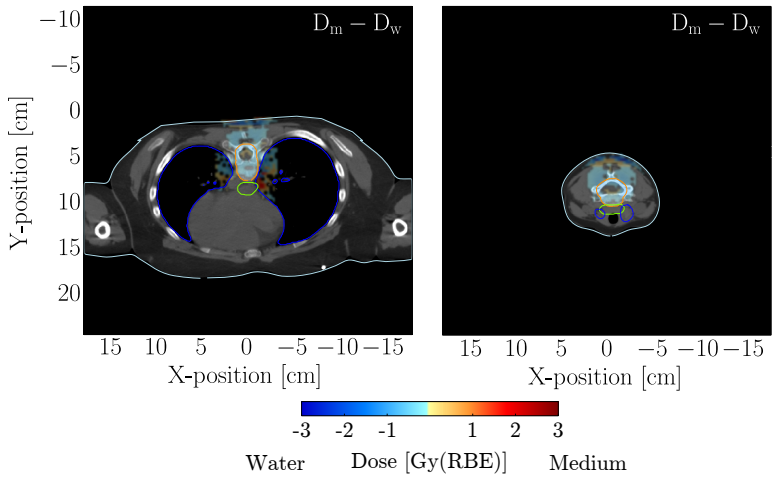

Figure 5.15: Dose differences between dose-to-medium and dose-to-water for the CSI plan, as calculated by FLUKA. Dose differences between -0.1 and 0.1 Gy(RBE) are not shown.

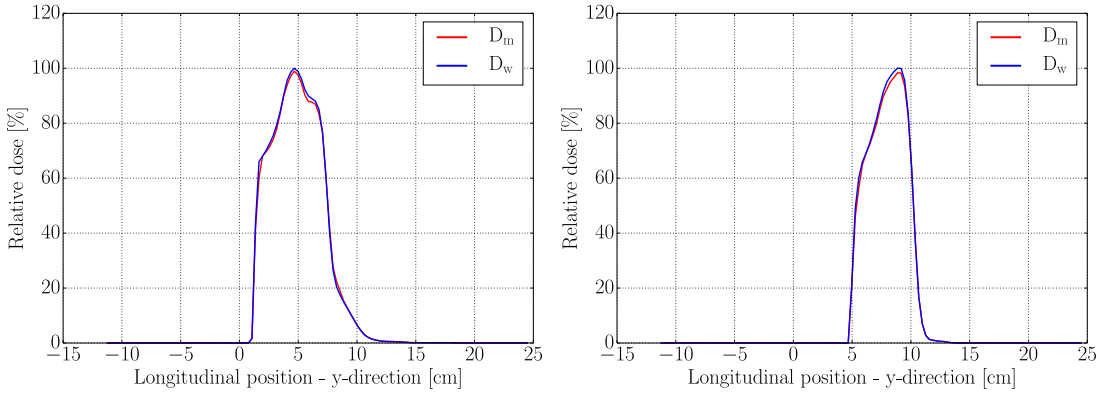

(a) Dose-to-medium vs. dose-to-water at $z = 8.4\,\text{cm}$.

(b) Dose-to-medium vs. dose-to-water at $z = 21.6\,\text{cm}$.

Figure 5.16: Longitudinal depth dose curves of dose-to-medium and dose-to-water for the CSI plan, as calculated by FLUKA.

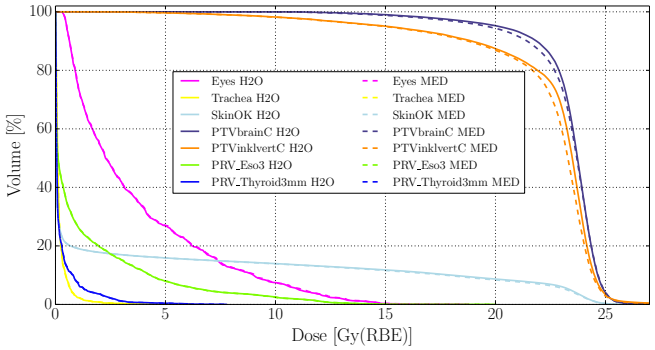

Figure 5.17: Dose volume histograms for ROIs for dose-to-medium (MED) and dose-to-water (H2O) for the CSI plan. Solid lines depict dose-to-water, while dashed lines depict dose-to-medium.

5.3 FLUKA DICOM Export

The FLUKA calculated doses can, by using the developed tool, be converted into DICOM RT Dose files. This section demonstrates that the DICOM export procedure performs well and shows some of the possibilities that opens up when importing the FLUKA dose into the RayStation TPS. All the following figures are obtained directly from RayStation. In the dose difference plots, warm colors depict higher doses from the TPS while colder colors depict higher doses from FLUKA.

In Figure 5.18 the same comparison as shown in figures 5.1a-5.1c is displayed, however, in this case, the comparison has been conducted in RayStation. The same slice location is shown ($z = -0.1\,\text{cm}$), but the dose cutoff for the differences is now set at 1.0 % of 70 Gy, which is the prescribed dose. Dose evaluation in RayStation is possible in several planes i.e. the transverse, sagittal or coronal plane.

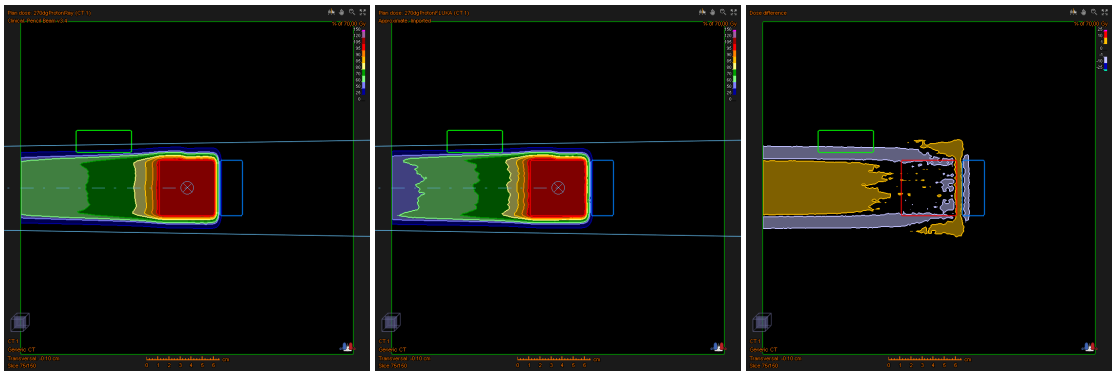

Figure 5.18: Dose distribution comparison for the homogeneous water phantom, conducted in RayStation. Differences below 1.0 % of 70 Gy are set transparent.

It is also possible to import doses calculated by other treatment planning systems into RayStation. The Syngo- and FLUKA doses for the CSI plan were imported into RayStation along with the CT images and structures. In Figure 5.19 the dose distributions calculated by Syngo and FLUKA can be seen. The same slice as in figures 5.8d-5.8f is displayed. The dose difference is cut off at 1.0 % of the prescribed dose (23.4 Gy(RBE)). Figure 5.20 outlines the dose statistics for a few selected volumes in the patient, while Figure 5.21 shows the FLUKA calculated dose distribution in the transverse, coronal and sagittal plane as displayed by RayStation.

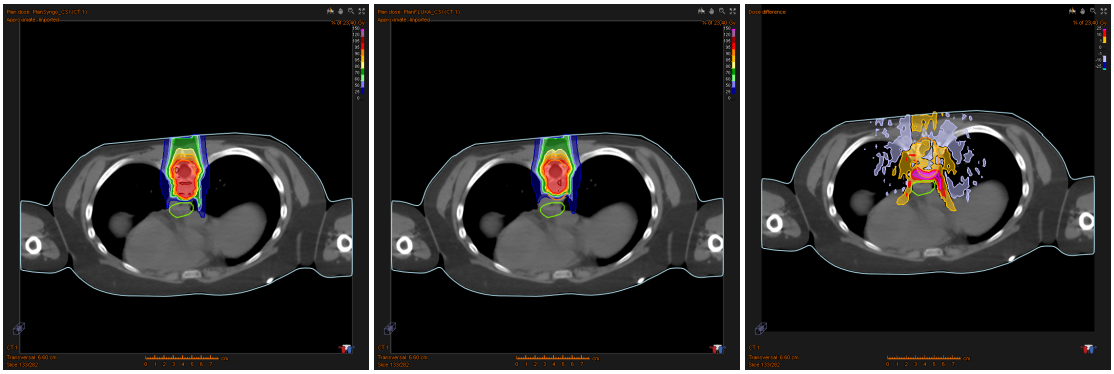

Figure 5.19: Dose distribution comparison for the CSI plan, conducted in RayStation. Differences below 1.0 % of 23.4 Gy(RBE) are set transparent.

Dose	ROI	ROI vol. [cm³]	Dose [Gy] D99	D98	D95	Average	D50	D2	D1
Plan dose: PlanSyngo_CSI (CT 1)	Eyes	18.69	0.37	0.44	0.60	4.37	3.35	12.91	14.08
Plan dose: PlanFLUKA_CSI (CT 1)	Eyes	18.69	0.39	0.43	0.51	3.63	2.28	12.99	14.12
Plan dose: PlanSyngo_CSI (CT 1)	PRV_Eso3	51.61	0.00	0.00	0.00	4.11	0.12	23.07	24.21
Plan dose: PlanFLUKA_CSI (CT 1)	PRV_Eso3	51.61	0.00	0.00	0.00	1.29	0.12	10.64	12.07
Plan dose: PlanSyngo_CSI (CT 1)	PRV_Thyroid3mm	14.79	0.00	0.00	0.00	0.94	0.02	7.47	9.87
Plan dose: PlanFLUKA_CSI (CT 1)	PRV_Thyroid3mm	14.79	0.01	0.01	0.01	0.28	0.06	2.59	3.18
Plan dose: PlanSyngo_CSI (CT 1)	PTVbrainC	1562.39	22.37	22.73	23.03	23.67	23.69	24.45	24.57
Plan dose: PlanFLUKA_CSI (CT 1)	PTVbrainC	1562.39	15.04	17.01	20.16	23.34	23.73	25.23	25.48
Plan dose: PlanSyngo_CSI (CT 1)	PTVinklvertC	570.63	18.82	19.95	21.65	23.61	23.76	25.16	25.40
Plan dose: PlanFLUKA_CSI (CT 1)	PTVinklvertC	570.63	7.65	10.49	15.08	22.45	23.49	25.25	25.83
Plan dose: PlanSyngo_CSI (CT 1)	SkinOK	27388.71	0.00	0.00	0.00	3.24	0.01	23.99	24.21
Plan dose: PlanFLUKA_CSI (CT 1)	SkinOK	27388.71	0.00	0.00	0.00	3.11	0.02	24.18	24.52
Plan dose: PlanSyngo_CSI (CT 1)	Trachea	9.92	0.00	0.00	0.00	0.73	0.22	4.46	6.02
Plan dose: PlanFLUKA_CSI (CT 1)	Trachea	9.92	0.00	0.01	0.02	0.20	0.10	1.14	1.68

Figure 5.20: Dose statistics from Syngo and FLUKA for ROIs in the CSI plan. The large discrepancies are mostly due to the reported FLUKA beam pullback.

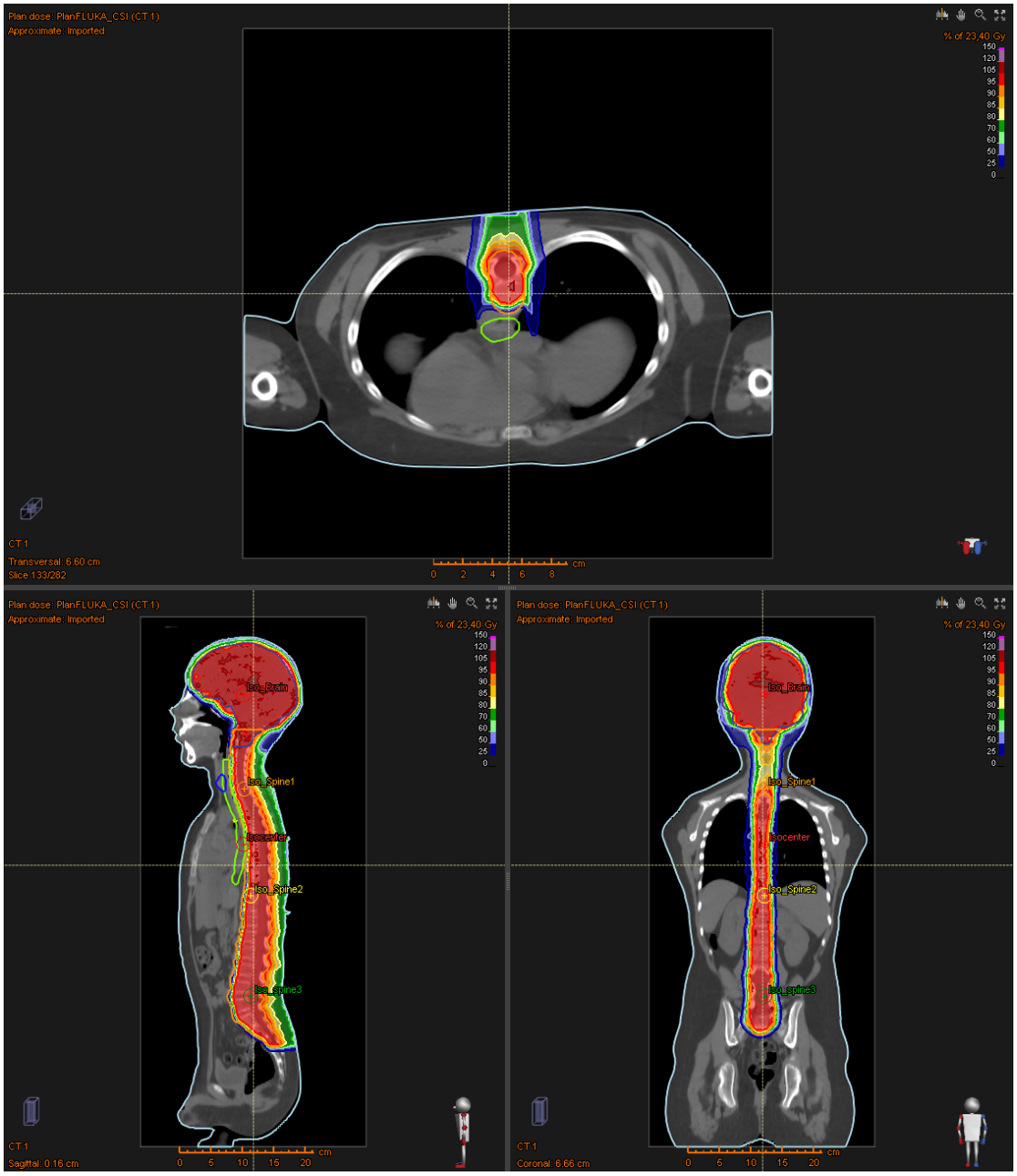

Figure 5.21: Evaluation of the FLUKA recalculated dose distribution for the CSI plan, conducted in RayStation.

Chapter 6

Discussion and Further Work

6.1 Dosimetric Verifications

The results in section 5.1 show that the tool developed in this project is successful in importing treatment plans, calculated by clinically used commercial treatment planning systems, into the FLUKA Monte Carlo tool for dose recalculation. This includes extracting the relevant information for each pencil beam in the treatment, and further transforming this information into a format readable for FLUKA. Interpolation of dose distributions and plotting of e.g. delineated structures performs as expected. As a consequence, the tool enables display of two-dimensional dose distributions in the transverse plane along with two-dimensional dose distribution differences, in addition to lateral- and longitudinal one-dimensional dose curves. Finally, dose volume histograms for both the TPS and FLUKA can be created, and DICOM export enables Monte Carlo dose visualization in a commercial TPS.

For the homogeneous water phantom, the differences in the dose distributions from RayStation and FLUKA were minor. A relatively similar homogeneous dose was delivered to the PTV for both systems. For all the phantom irradiation plans, including the CSI plan, higher doses were reported by FLUKA at the outer regions of the beam. This is consistent with the findings of Howell *et al.* [100] who showed that TPSs may underestimate out-of-field doses, increasing in magnitude for longer distances. Another similarity for the phantoms was that a lower dose was scored by FLUKA in the middle area of the beam. The reason for this was not further explored; however, the geometrical normalization method for the water phantoms may have resulted in this discrepancy. It was based on the assumption that the average dose located at the center of the PTV was similar for the two simulations. If this is not the case, the normalization may introduce high levels of uncertainties. However, without knowing the number of particles used in the treatment, nor the conversion factor between the monitor unit output and the number of particles (this conversion factor can be obtained by measurements in ionization chambers [71]), the geometrical normalization approach was decided to be adequately accurate for the purpose of this project. For comparisons with clinical accuracy, the FLUKA dose must be normalized properly.

When inhomogeneities were introduced into the phantoms, the differences between the analytical calculations and the Monte Carlo simulations increased. The dose to the PTV became less homogeneous for both the phantoms containing a bone- and air volume. The differences were largest for regions where the beam had penetrated the inhomogeneities. As noted previously in this thesis, it is in

regions containing inhomogeneities where Monte Carlo simulations are superior compared to commercial treatment planning systems [15, 32–37].

Most apparent for the homogeneous water phantom, was the disagreement between the calculated beam ranges for the two systems. The main reason for this may be due to an incorrect matching of the stopping powers. The geometrical normalization may also have contributed to the different ranges. And lastly, a lack of beam line implementation in FLUKA may, in addition, have contributed to the differences. The RayStation simulations were conducted using an IBA-based nozzle design. No range shifter was selected to be used in the simulations, but there may, for example, have been a vacuum window or other components in the nozzle design, resulting in a decreased range of the simulated RayStation beam.

When looking at the dose difference plots and the depth dose curves for the clinical cranio-spinal irradiation plan, there was an apparent difference between the simulated ranges in FLUKA and the TPS. The range of the FLUKA simulated beam was around 0.5 cm shorter than for Syngo. As no calibration between the two systems was conducted, this may have introduced a change in beam range. Ideally, a calibration curve between the Hounsfield units and relative stopping powers should be implemented into FLUKA [35, 68]. While nuclear processes scales with the density, electromagnetic processes must be furthermore adjusted to reproduce the same dependence between the relative stopping powers and HUs, used by the treatment planning system [82]. A method of matching stopping powers between the TPS and a Monte Carlo tool can be found in [38].

In addition, both a range shifter and a range modulator were utilized for the CSI plan. As previously mentioned, no information about the beam line and nozzle used for the TPS simulation was available, except for the water equivalent thicknesses of the modulator and range shifter. As a result, the range shifting components had to be modeled in FLUKA as slabs of water, introducing additional uncertainty. This may have been avoided with proper implementation of the range modulator and range shifter. Other parts of the beam line geometry should also be modeled in the Monte Carlo simulations in order to obtain correspondence with the treatment planning system and treatment room [101, 102]. The decreased range of the FLUKA beam introduced significantly lower doses to OARs and insufficient dose coverage to the target volumes. Another reason, contributing to the reported pullback from FLUKA, may have been the Hounsfield units outside the patient. To minimize computation time, commercial treatment planning systems normally assign a HU of -1024 (vacuum) for all regions outside the patient. This was not done in this project. The voxel cage that encapsulates all the voxels of the patient in FLUKA, was surrounded by vacuum. However, most voxels between the vacuum and the patient (a length of approximately 15 cm) had a HU of about -995, or less. The difference in HUs was moderate, but may nevertheless have contributed to the observed range difference. Further work should include addressing these issues.

A substantial advantage for the CSI plan was that the number of particles used for treatment was available, and thus proper normalization could be performed by multiplying the reported FLUKA dose by the original number of particles (see section 4.4). To gain a true comparison between dose calculation methods and

find the absolute difference, the normalization should be based upon the numbers of particles given in the plan. Between 0.034 and 0.016 % of the initial number of primary beam particles were simulated. This yielded mean statistical errors below 2 % in the PTVs and below 10 % for regions with lower doses (outside the treatment fields). The errors did however increase rapidly for very low-dose regions. As a statistical uncertainty of about 2 % in the PTV is required in a clinical setting [35, 103], it was concluded that the number of particles simulated in this project was sufficient. The fraction of particles simulated was also in agreement the findings of Verburg *et al.* [38], who have stated that a number of histories, that is 4-5 orders of magnitude below the number of particles used in the treatment plan, will suffice to obtain accurate results. They further emphasize that the number of histories should be increased if doses to regions far outside the treatment field are of interest.

Results from the CSI plan also showed some minor differences between the dose-to-water and dose-to-medium. Even though the differences were relatively small, the same dose scoring methods should always be performed in order to minimize uncertainties between the two systems. Siebers *et al.* [104] has for photon radiation reported a difference of 1 % in soft tissue and over 10 % in dense bone. Similar effects has been shown for protons by Jiang *et al.* [105]. This is in compliance with the presented results for the simulated bone phantom irradiation, where the reported difference between the two scoring methods was on the order of 5 % for all parts of the phantom.

6.2 Further Potential for the Developed Tool

By importing clinically calculated treatment plans into a Monte Carlo simulation tool, a number of possibilities open up for the evaluation of treatment quality and analyzing different aspects of particle therapy. Treatment planning systems are typically very restricted in which quantities they are able to score (in most cases only dose). By using Monte Carlo tools for recalculation of treatment plans, not only will a more accurate dose distribution be obtained [33], but for example scoring of excess dose due to nuclear fragments [15], range verifications [82] and linear energy transfer scoring [106] can be performed. This section will give a short outline of some of the applications that the developed tool makes achievable, either right away, or in the near future.

Linear energy transfer scoring

Even though a generic RBE value of 1.1 is used for proton therapy, it is well known that this is only an approximation, as the RBE depends on dose, endpoint, LET and other factors [107]. It has also been established that the RBE increases at the distal end of the Bragg peak [108]. This is due to the increased LET for low energy particles (Figure 2.6), and the RBE dependence on LET (Figure 2.7). The variations in LET and RBE are even more pronounced for carbon ions [109]. A homogeneous dose distribution does not guarantee a homogeneous LET distribution and may result in a varying biological effect to the tissue [107]. By

mapping the LET variations in the human anatomy, the RBE dependence can be more precisely determined, and the physical dose can be weighted accordingly.

The FLUKA Monte Carlo tool has the ability to score LET [110]. Thus, by importing clinical treatment plans into FLUKA, the LET distributions in regions of interest can be determined. The dose can further be biologically weighted according to the more accurately determined RBE. And with some minor modifications, the tool can also be used to evaluate the varying RBE for carbon ions.

Custom response models

In addition to calculating RBE and biological doses based on LET, it should be relatively straightforward to couple FLUKA with models for normal tissue complication probabilities (NTCP) and other endpoints such as e.g. secondary cancer risk models.

The risk of developing secondary cancer is of concern in radiation therapy. By converting doses received by different organs and regions in the body, to risks of developing secondary cancers using dose-risk models, the risk distributions can be displayed superimposed on the patient CT images, similar as for the dose distributions. This was done by Zhang *et al.* [111] in 2015, by developing their own risk models. They did the procedure by converting doses calculated by a TPS into secondary cancer risk. They did however state that Monte Carlo simulations should be utilized for assessing the risk in low- and medium-dose regions because of their higher accuracy. Most secondary cancers occur in low-dose areas [112, 113].

The developed tool makes the implementation of custom response models possible, both for TPS calculated doses and Monte Carlo doses. By some minor modifications, the tool can evaluate the magnitude of doses inside delineated regions/organs. These doses can (on a pixel-by-pixel basis) be further weighted, converted, removed, and so forth, depending on what is desirable.

Scoring neutron doses

Neutrons can be a large contributer to the dose in the low-dose regions for particle therapy [114, 115]. This is because neutrons do not carry any charge, and may therefore deposit their dose far from the target volume [48]. To get a better understanding of low-dose regions and associated neutron doses, it is necessary to score the neutron associated doses inside the patient.

As mentioned, FLUKA is able to score numerous quantities not feasible for a commercial treatment planning system. Therefore, by using the tool, clinical treatment plans can be imported into FLUKA, where neutron doses can be scored and further evaluated.

6.3 Suggestions for Further Work

Patient orientations that differ from head first - supine and head first - prone, are not supported by any of the scripts. The reason for this was mainly because

the scripts were first developed to be only able to handle gantry angles, and therefore, due to time constraints, support for other orientations was not added. However, a generalization of coordinate system transformations should be possible to implement. The tool is furthermore not able to automatically handle rotations of the treatment couch. However, for the CSI plan used in this project, the couch was rotated. By manually changing the simulated gantry angle to correspond to the specific couch angle, it was possible to recalculate the plans. Therefore, automatic support for treatment table rotations could be added to the tool.

Automated removal of the treatment couch, and assigning vacuum to all regions outside the patient, could be implemented to achieve better correspondence with the treatment planning systems. This can be done by obtaining the positions of all the pixels outside the delineated external contour of the patient, and setting the Hounsfield units of these pixels equal to -1024.

Some minor modifications may be needed for dose recalculations of treatment plans using other particles than protons, as this was not addressed in this project. And further, to perform Monte Carlo recalculations with clinically acceptable precision, the beam line, treatment head and other treatment room specifics should be implemented into the Monte Carlo tool. In addition, proper calibration of stopping powers and HU between the two systems should be carried out.

Chapter 7

Conclusion

In this project, a Monte Carlo based treatment planning verification tool for particle therapy has been developed. The novel tool in this work reads relevant treatment plan information from the DICOM format, and translates the data for recalculations of dose within the FLUKA Monte Carlo code. Furthermore, scripts for versatile comparisons of dose distributions from TPS and FLUKA were created. A method for exporting the FLUKA recalculated doses to DICOM format was also developed, which further enables import of Monte Carlo calculated plans in commercial treatment planning systems.

In addition to recalculation of dose, the tool serves as a research framework for studies including neutron doses and scoring of other secondary particles, LET mapping, particle beam range verifications, clinically relevant endpoints such as NTCP and secondary cancer visualization risk, and so forth.

The results in this thesis demonstrate the developed tool's capability of recalculation of doses using Monte Carlo simulations. Furthermore, the results show that detailed information of the beam line and beam configuration, and calibration with respect to a specific TPS or treatment machine, is essential in order to achieve clinical precision in the recalculation process. Further work should focus on the implementation of specific beam lines, treatment nozzle and other facility dependent parameters.

Bibliography

[1] R. W. Ruddon. *Cancer Biology*. 4th ed. Oxford University Press, 2007.

[2] N. S. Hosmane et al. *Boron And Gadolinium Neutron Capture Therapy For Cancer Treatment*. 1st ed. World Scientific Publishing Company, 2012.

[3] J. Thariat et al. "Past, present, and future of radiotherapy for the benefit of patients". In: *Nature Reviews Clinical Oncology* 10.1 (2012), pp. 52–60.

[4] I. K. Larsen, ed. *Cancer in Norway 2013 - Cancer incidence, mortality, survival and prevalence in Norway* (2015). Oslo: Cancer Registry of Norway.

[5] Helse Vest, Helse Sør-Øst, Helse Midt-Norge, Helse Nord, Helsedirektoratet. *Planlegging av norsk senter for partikkelterapi*. 2013.

[6] A. Van der Kogel and M. Joiner. *Basic Clinical Radiobiology*. 4th. A Hodder Arnold Publication, 2009.

[7] H. Paganetti, ed. *Proton Therapy Physics (Series in Medical Physics and Biomedical Engineering)*. 1st ed. CRC Press, 2011.

[8] U. Amaldi and G. Kraft. "Radiotherapy with beams of carbon ions". In: *Reports on Progress in Physics* 68.8 (2005), pp. 1861–1882.

[9] M. Jermann. "Particle Therapy Statistics in 2014". In: *International Journal of Particle Therapy* 2.1 (2015), pp. 50–54.

[10] O. H. Odland. "Status of Particle Therapy in Norway". In: *ENLIGHT Highlights* (2014), p. 17.

[11] M. Lederman. "The early history of radiotherapy: 1895–1939". In: *International Journal of Radiation Oncology * Biology * Physics* 7.5 (1981), pp. 639–648.

[12] R. R. Wilson. "Radiological use of fast protons". In: *Radiology* 47.5 (1946), pp. 487–491.

[13] U. Linz, ed. *Ion Beam Therapy: Fundamentals, Technology, Clinical Applications (Biological and Medical Physics, Biomedical Engineering)*. 2012th ed. Springer, 2011.

[14] L. Hong et al. "A pencil beam algorithm for proton dose calculations". In: *Physics in Medicine and Biology* 41.8 (1996), pp. 1305–1330.

[15] J. Bauer et al. "Integration and evaluation of automated Monte Carlo simulations in the clinical practice of scanned proton and carbon ion beam therapy". In: *Physics in Medicine and Biology* 59.16 (2014), pp. 4635–4659.

[16] S. Yajnik. *Proton Beam Therapy: How Protons are Revolutionizing Cancer Treatment*. 2013th ed. Springer, 2014.

[17] K. S. Ytre-Hauge. "Measurements and Monte Carlo Simulations of Neutron Doses from Radiation Therapy with Photons, Protons and Carbon Ions". PhD thesis. University of Bergen, 2013.

[18] S. Dhanesar et al. "SU-E-T-403: Intensity Modulated Proton Therapy Plans with Multiple Fields for Prostate Cancer". In: *Medical Physics* 40.6 (2013), pp. 297–297.

[19] E. B. Podgorsak. *Radiation Oncology Physics: A Handbook for Teachers And Students*. Intl Atomic Energy Agency, 2005.

[20] A. J. Lomax et al. "A treatment planning inter-comparison of proton and intensity modulated photon radiotherapy". In: *Radiotherapy and Oncology: Journal of the European Society for Therapeutic Radiology and Oncology* 51.3 (1999), pp. 257–271.

[21] H. Paganetti. "Range uncertainties in proton therapy and the role of Monte Carlo simulations". In: *Physics in Medicine and Biology* 57.11 (2012), R99–R117.

[22] C. H. Stokkevåg et al. "Risk of radiation-induced secondary rectal and bladder cancer following radiotherapy of prostate cancer". In: *Acta Oncologica* 54.9 (2015), pp. 1317–1325.

[23] J. D. Boice et al. "Second cancers following radiation treatment for cervical cancer. An international collaboration among cancer registries". In: *Journal of the National Cancer Institute* 74.5 (1985), pp. 955–975.

[24] D. J. Brenner et al. "Second malignancies in prostate carcinoma patients after radiotherapy compared with surgery". In: *Cancer* 88.2 (2000), pp. 398–406.

[25] C. H. Stokkevåg et al. "Estimated risk of radiation-induced cancer following paediatric cranio-spinal irradiation with electron, photon and proton therapy". In: *Acta Oncologica* 53.8 (2014), pp. 1048–1057.

[26] D. L. Preston et al. "Solid cancer incidence in atomic bomb survivors: 1958-1998". In: *Radiation Research* 168.1 (2007), pp. 1–64.

[27] A. Peeters et al. "How costly is particle therapy? Cost analysis of external beam radiotherapy with carbon-ions, protons and photons". In: *Radiotherapy and Oncology* 95.1 (2010), pp. 45–53.

[28] M. Schwarz. "Treatment planning in proton therapy". In: *The European Physical Journal Plus* 126.7 (2011), pp. 1–10.

[29] M. Urie et al. "Degradation of the Bragg peak due to inhomogeneities". In: *Physics in Medicine and Biology* 31.1 (1986), pp. 1–15.

[30] P. Andreo. "On the clinical spatial resolution achievable with protons and heavier charged particle radiotherapy beams". In: *Physics in Medicine and Biology* 54.11 (2009), N205–N215.

[31] Z. Li. "ICRU Report 78—Prescribing, Recording, and Reporting Proton-Beam Therapy". In: *International Journal of Radiation Oncology * Biology * Physics* 73.5 (2009), p. 1602.

[32] H. Jiang and H. Paganetti. "Adaptation of GEANT4 to Monte Carlo dose calculations based on CT data". In: *Medical Physics* 31.10 (2004), pp. 2811–2818.

[33] A. Tourovsky et al. "Monte Carlo dose calculations for spot scanned proton therapy". In: *Physics in Medicine and Biology* 50.5 (2005), pp. 971–981.

[34] B. Juste et al. "Radiotherapy treatment planning based on Monte Carlo techniques". In: *Nuclear Instruments and Methods in Physics Research Section A: Accelerators, Spectrometers, Detectors and Associated Equipment*. Frontiers in radiation physics and applications:Proceedings of the 11th International Symposium on Radiation Physics 619.1–3 (2010), pp. 252–257.

[35] H. Paganetti et al. "Clinical implementation of full Monte Carlo dose calculation in proton beam therapy". In: *Physics in Medicine and Biology* 53.17 (2008), p. 4825.

[36] A. Mesbahi, D. I. Thwaites, and A. J. Reilly. "Experimental and Monte Carlo evaluation of Eclipse treatment planning system for lung dose calculations". In: *Reports of Practical Oncology & Radiotherapy* 11.3 (2006), pp. 123–133.

[37] S. Çatlı and G. Tanır. "Experimental and Monte Carlo evaluation of Eclipse treatment planning system for effects on dose distribution of the hip prostheses". In: *Medical Dosimetry* 38.3 (2013), pp. 332–336.

[38] J. M. Verburg et al. "Automated Monte Carlo Simulation of Proton Therapy Treatment Plans". In: *Technology in Cancer Research & Treatment* (2015).

[39] A. Mairani et al. "A Monte Carlo-based treatment planning tool for proton therapy". In: *Physics in Medicine and Biology* 58.8 (2013), p. 2471.

[40] A. Ferrari et al. *FLUKA: a multi-particle transport code*. Tech. rep. SLAC-R-773. Stanford Linear Accelerator Center (SLAC), 2005.

[41] T. T. Böhlen et al. "The FLUKA Code: Developments and Challenges for High Energy and Medical Applications". In: *Nuclear Data Sheets* 120 (2014), pp. 211–214.

[42] R. Kaderka. "Out-of-field dose measurements in radiotherapy". PhD thesis. Technische Universität Darmstadt, 2011.

[43] W. R. Leo. *Techniques for Nuclear and Particle Physics Experiments*. 2nd Rev. Springer, 1994.

[44] K. A. Olive and Particle Data Group. "Review of Particle Physics". In: *Chinese Physics C* 38.9 (2014), p. 090001.

[45] J. F. Ziegler. "Stopping of energetic light ions in elemental matter". In: *Journal of Applied Physics* 85.3 (1999), pp. 1249–1272.

[46] E. Sengbusch et al. "Maximum proton kinetic energy and patient-generated neutron fluence considerations in proton beam arc delivery radiation therapy". In: *Medical Physics* 36.2 (2009), pp. 364–372.

[47] NIST US Department of Commerce. *NIST Stopping-Power and Range Tables: Electrons, Protons, Helium Ions*. URL: `http://www.nist.gov/pml/data/star/` (visited on 03/28/2016).

[48] B. Gottschalk. "Physics of Proton Interactions in Matter". In: *Proton Therapy Physics*. Series in Medical Physics and Biomedical Engineering. CRC Press, 2011, pp. 19–60.

[49] C. Grupen and B. Shwartz. *Particle Detectors (Cambridge Monographs on Particle Physics, Nuclear Physics and Cosmology)*. 2nd ed. Cambridge University Press, 2008.

[50] S. Greilich et al. "Amorphous track models: A numerical comparison study". In: *Radiation Measurements* 45.10 (2010), pp. 1406–1409.

[51] H. Cember and T. Johnson. *Introduction to Health Physics: Fourth Edition*. 4th ed. McGraw-Hill Education / Medical, 2008.

[52] D. J. Thomas. "ICRU Report 85—Fundamental Quantities and Units for Ionizing Radiation". In: *Radiation Protection Dosimetry* 150.4 (2012), pp. 550–552. ISSN: 0144-8420, 1742-3406.

[53] ICRP. *ICRP Publication 26: Recommendations of the ICRP*. 1st ed. SAGE Publications Ltd, 1977.

[54] P. Mayles, A. Nahum, and J. C. Rosenwald, eds. *Handbook of Radiotherapy Physics: Theory and Practice*. 1st ed. CRC Press, 2007.

[55] ICRP. *ICRP Publication 103: Recommendations of the ICRP*. 1st ed. SAGE Publications Ltd, 2013.

[56] E. J. Hall and A. J. Giaccia. *Radiobiology for the Radiologist*. Seventh. Lippincott Williams & Wilkins, 2011.

[57] G. B. Saha. *Physics and Radiobiology of Nuclear Medicine*. 3rd. Springer, 2006.

[58] H. L. Borges, R. Linden, and J. Y. Wang. "DNA damage-induced cell death". In: *Cell research* 18.1 (2008), pp. 17–26.

[59] M. R. Kelley, ed. *DNA Repair in Cancer Therapy: Molecular Targets and Clinical Applications*. 1st ed. Academic Press, 2011.

[60] M. Beyzadeoglu, G. Ozyigit, and C. Ebruli. *Basic Radiation Oncology*. 2010th ed. Springer, 2010.

[61] H. Paganetti. "Relating Proton Treatments to Photon Treatments via the Relative Biological Effectiveness—Should We Revise Current Clinical Practice?" In: *International Journal of Radiation Oncology * Biology * Physics* 91.5 (2015), pp. 892–894.

[62] H. Paganetti et al. "Relative biological effectiveness (RBE) values for proton beam therapy". In: *International Journal of Radiation Oncology * Biology * Physics* 53.2 (2002), pp. 407–421.

[63] H. Paganetti. "Relative biological effectiveness (RBE) values for proton beam therapy. Variations as a function of biological endpoint, dose, and linear energy transfer". In: *Physics in Medicine and Biology* 59.22 (2014), R419–R472.

[64] N. Barrie Smith and A. Webb. *Introduction to Medical Imaging: Physics, Engineering and Clinical Applications (Cambridge Texts in Biomedical Engineering)*. 1st ed. Cambridge University Press, 2010.

[65] L. E. Romans. *Computed Tomography for Technologists: A Comprehensive Text*. 1st ed. Wollters Kluwer Health / Lippincott Williams & Wilkins, 2010.

[66] B. Schaffner and E. Pedroni. "The precision of proton range calculations in proton radiotherapy treatment planning: experimental verification of the relation between CT-HU and proton stopping power". In: *Physics in Medicine and Biology* 43.6 (1998), pp. 1579–1592.

[67] U. Schneider, E. Pedroni, and A. Lomax. "The calibration of CT Hounsfield units for radiotherapy treatment planning". In: *Physics in Medicine and Biology* 41.1 (1996), pp. 111–124.

[68] K. Parodi et al. "PET/CT imaging for treatment verification after proton therapy: a study with plastic phantoms and metallic implants". In: *Medical Physics* 34.2 (2007), pp. 419–435.

[69] D. Jones. "ICRU Report 50—Prescribing, Recording and Reporting Photon Beam Therapy". In: *Medical Physics* 21.6 (1994), pp. 833–834.

[70] F. M. Khan. *The Physics of Radiation Therapy*. Fourth. LWW, 2009.

[71] I. J. Das and H. Paganetti. *Principles and Practice of Proton Beam Therapy*. Medical Physics Pub Corp, 2015.

[72] J. J. Wilkens and U. Oelfke. "Optimization of radiobiological effects in intensity modulated proton therapy". In: *Medical Physics* 32.2 (2005), pp. 455–465.

[73] W. C. Schlegel et al., eds. *New Technologies in Radiation Oncology (Medical Radiology)*. 2006th ed. Springer, 2006.

[74] D. Schulz-Ertner, O. Jäkel, and W. Schlegel. "Radiation Therapy With Charged Particles". In: *Seminars in Radiation Oncology* 16.4 (2006), pp. 249–259.

[75] J. M. Schippers. "Beam delivery systems for particle radiation therapy: current status and recent developments". In: *Reviews of Accelerator Science and Technology* 2.01 (2009), pp. 179–200.

[76] M. Engelsman, M. Schwarz, and L. Dong. "Physics Controversies in Proton Therapy". In: *Seminars in Radiation Oncology* 23.2 (2013), pp. 88–96.

[77] C. Grupen and I. Buvat, eds. *Handbook of Particle Detection and Imaging*. 2012th ed. Springer, 2011.

[78] G. O. Sawakuchi et al. "Density heterogeneities and the influence of multiple Coulomb and nuclear scatterings on the Bragg peak distal edge of proton therapy beams". In: *Physics in Medicine and Biology* 53.17 (2008), pp. 4605–4619.

[79] N. Kanematsu et al. "A CT calibration method based on the polybinary tissue model for radiotherapy treatment planning". In: *Physics in medicine and biology* 48.8 (2003), p. 1053.

[80] V. Vlachoudis. "FLAIR: a powerful but user friendly graphical interface for FLUKA". In: *Proc. Int. Conf. on Mathematics, Computational Methods & Reactor Physics (M&C 2009), Saratoga Springs, New York*. 2009.

[81] W. Schneider, T. Bortfeld, and W. Schlegel. "Correlation between CT numbers and tissue parameters needed for Monte Carlo simulations of clinical dose distributions". In: *Physics in Medicine and Biology* 45.2 (2000), p. 459.

[82] K. Parodi et al. "Clinical CT-based calculations of dose and positron emitter distributions in proton therapy using the FLUKA Monte Carlo code". In: *Physics in Medicine and Biology* 52.12 (2007), pp. 3369–3387.

[83] A. Ferrari et al. *FLUKA: a multi-particle transport code (Manual)*. Stanford Linear Accelerator Center (SLAC). 2014.

[84] National Electrical Manufacturers Association (NEMA). *DICOM PS3.3 2014a - Information Object Definitions*. NEMA. DICOM Standards Committee, 2014.

[85] IEC TC/SC 62C. *IEC 61217 Ed. 1.1 b:2002, Radiotherapy equipment - Coordinates, movements and scales*. Multiple. Distributed through American National Standards Institute (ANSI), 2007.

[86] O. Ratib. "OSIRIX: An Open Source Platform for Advanced Multimodality Medical Imaging". In: *2006 ITI 4th International Conference on Information Communications Technology*. 2006, pp. 1–2.

[87] G. van Rossum and the Python development team. *The Python Language Reference*. Reference Manual. Version 2.7.11. Python Software Foundation, 2016.

[88] D. Mason. "SU-E-T-33: Pydicom: An Open Source DICOM Library". In: *Medical Physics* 38.6 (2011), pp. 3493–3493.

[89] S. van der Walt, S. C. Colbert, and G. Varoquaux. "The NumPy Array: A Structure for Efficient Numerical Computation". In: *Computing in Science & Engineering* 13.2 (2011), pp. 22–30.

[90] J. D. Hunter. "Matplotlib: A 2D Graphics Environment". In: *Computing in Science & Engineering* 9.3 (2007), pp. 90–95.

[91] A. Panfili. "Development of a Monte Carlo tool to verify Treatment Planning in proton therapy at CNAO". Thesis. University of Milan, 2011.

[92] N. Bassler and I. Kantemiris. "Comparison of optimized single and multifield irradiation plans of antiproton, proton and carbon ion beams". In: *Radiotherapy and oncology : journal of the European Society for Therapeutic Radiology and Oncology* 95.1 (2010), pp. 87–93.

[93] R. Malyapa et al. "Evaluation of Robustness to Setup and Range Uncertainties for Head and Neck Patients Treated With Pencil Beam Scanning Proton Therapy". In: *International Journal of Radiation Oncology * Biology * Physics* 95.1 (2016), pp. 154–162.

[94] *Dicomutils*. URL: `https://github.com/raysearchlabs/dicomutils.git` (visited on 05/05/2016).

[95] R. J. Packer et al. "Survival and secondary tumors in children with medulloblastoma receiving radiotherapy and adjuvant chemotherapy: results of Children's Oncology Group trial A9961". In: *Neuro-Oncology* 15.1 (2013), pp. 97–103.

[96] T. Bortfeld. "An analytical approximation of the Bragg curve for therapeutic proton beams". In: *Medical Physics* 24.12 (1997), p. 2024.

[97] W. C. Hsi et al. "Energy spectrum control for modulated proton beams". In: *Medical Physics* 36.6 (June 2009), pp. 2297–2308. (Visited on 05/31/2016).

[98] H. Paganetti. "Dose to water versus dose to medium in proton beam therapy". In: *Physics in Medicine and Biology* 54.14 (2009), pp. 4399–4421.

[99] A. C. Guyton and J. E. Hall. *Textbook of Medical Physiology*. 11th ed. Saunders, 2005.

[100] R. M. Howell et al. "Accuracy of out-of-field dose calculations by a commercial treatment planning system". In: *Physics in Medicine and Biology* 55.23 (2010), pp. 6999–7008.

[101] K. Parodi et al. "Monte Carlo simulations to support start-up and treatment planning of scanned proton and carbon ion therapy at a synchrotron-based facility". In: *Physics in Medicine and Biology* 57.12 (2012), pp. 3759–3784.

[102] T. V. M. Lima et al. "Monte Carlo Calculations Supporting Patient Plan Verification in Proton Therapy". In: *Frontiers in Oncology* 6 (2016).

[103] R. Jeraj and P. Keall. "The effect of statistical uncertainty on inverse treatment planning based on Monte Carlo dose calculation". In: *Physics in Medicine and Biology* 45.12 (2000), p. 3601.

[104] J. V. Siebers et al. "Converting absorbed dose to medium to absorbed dose to water for Monte Carlo based photon beam dose calculations". In: *Physics in Medicine and Biology* 45.4 (2000), p. 983.

[105] H. Jiang, J. Seco, and H. Paganetti. "Effects of Hounsfield number conversion on CT based proton Monte Carlo dose calculations". In: *Medical physics* 34.4 (2007), pp. 1439–1449.

[106] D. A. Granville and G. O. Sawakuchi. "Comparison of linear energy transfer scoring techniques in Monte Carlo simulations of proton beams". In: *Physics in Medicine and Biology* 60.14 (2015), N283.

[107] C. Grassberger et al. "Variations in linear energy transfer within clinical proton therapy fields and the potential for biological treatment planning". In: *International Journal of Radiation Oncology * Biology * Physics* 80.5 (2011), pp. 1559–1566.

[108] J. B. Robertson et al. "Radiobiological studies of a high-energy modulated proton beam utilizing cultured mammalian cells". In: *Cancer* 35.6 (1975), pp. 1664–1677.

[109] H. Suit et al. "Proton vs carbon ion beams in the definitive radiation treatment of cancer patients". In: *Radiotherapy and Oncology* 95.1 (2010), pp. 3–22.

[110] G. Giovannini et al. "Variable RBE in proton therapy: comparison of different model predictions and their influence on clinical-like scenarios". In: *Radiation Oncology* 11 (2016), p. 68.

[111] R. Zhang, D. Mirkovic, and W. D. Newhauser. "Visualization of risk of radiogenic second cancer in the organs and tissues of the human body". In: *Radiation Oncology* 10.1 (2015).

[112] W. Dörr and T. Herrmann. "Cancer induction by radiotherapy: dose dependence and spatial relationship to irradiated volume". In: *Journal of Radiological Protection: Official Journal of the Society for Radiological Protection* 22.3A (2002), A117–121.

[113] I. Diallo et al. "Frequency distribution of second solid cancer locations in relation to the irradiated volume among 115 patients treated for childhood cancer". In: *International Journal of Radiation Oncology * Biology * Physics* 74.3 (2009), pp. 876–883.

[114] H. Jiang et al. "Simulation of organ-specific patient effective dose due to secondary neutrons in proton radiation treatment". In: *Physics in Medicine and Biology* 50.18 (2005), pp. 4337–4353.

[115] U. Schneider et al. "Secondary neutron dose during proton therapy using spot scanning". In: *International Journal of Radiation Oncology * Biology * Physics* 53.1 (2002), pp. 244–251.